ENGINEERING FLUORESCENT PROTEIN BIOSENSORS FOR INTERROGATING BIOLOGICALLY RELEVANT CHEMICAL SPECIES

by

Keelan J. Trull

A Dissertation

Submitted to the Faculty of Purdue University

In Partial Fulfillment of the Requirements for the degree of

Doctor of Philosophy

Department of Chemistry

West Lafayette, Indiana

August 2019

THE PURDUE UNIVERSITY GRADUATE SCHOOL
STATEMENT OF COMMITTEE APPROVAL

Dr. Mathew Tantama, Chair

College of Science, Department of Chemistry

Dr. Angeline Lyon

College of Science, Department of Chemistry

Dr. Chengde Mao

College of Science, Department of Chemistry

Dr. Elizabeth Parkinson

College of Science, Department of Chemistry

Approved by:

Dr. Christine Hrycyna

Head of the Graduate Program

Dedication

I dedicate this work to the people who have helped my grow as a scientist and a person during my time as a graduate student: Emily Haynes, Stevie Norcross, Megha Rajendran, Isaac Tat and Piper Miller. Without these people I would not have made it to where I am today.

ACKNOWLEDGMENTS

I would like to acknowledge the undergraduates who I mentored and who assisted me in completing the work presented in this thesis: Isaac Tat, Piper Miller, and Ashley Varney. Isaac worked on much of the cloning for the ChoX constructs as well as the cloning for the redox sensors. He also completed the work for the ATP dose responses for both the BRET-based ATP sensor and the genetically encoded ADP sensor. Piper Miller assisted with screening the libraries for the ADP sensor and the red ATP sensors. Piper also did much of the *in vitro* characterization work for the ADP sensor. Ashley Varney assisted with the end stages of the ADP sensor project specifically she was responsible for cloning the sensor into the mammalian membrane expression vector.

I would like to acknowledge the people who worked with me on the redox sensor project. Mainly, Stevie Norcross, who is my co-author on the redox sensor work. She is also responsible for the *in vitro* characterization of the sensor's redox properties, and she assisted with the initial cell experiments was well as the experimental design for the NAC experiments. Jordan Snaider took the lifetime measurements for the redox sensors. I would like to acknowledge Saranya Radhakrisan, Jake Norley, and Sara Doan who have continued the work we started on the redox sensors.

I would also like to acknowledge Sehong Min, who started the work on the BRET ATP sensor and was the one who continue to optimize the sensors and showed their utility in tissue imaging.

I would like to acknowledge Mathew Tantama and the entire Tantama Lab for their support during my graduate studies.

TABLE OF CONTENTS

LIST OF TABLES

LIST OF FIGURES

LIST OF ABBREVIATIONS

ACh	acetylcholine
ADP	adenosine diphosphate
ATP	adenosine triphosphate
BRET	bioluminescent resonance energy transfer
CFP	cyan fluorescent protein
cpXFP	circularly permuted fluorescent protein (any color)
DTT	dithiothreitol
EDTA	Ethylenediaminetetraacetic acid
EGFP	enhanced green fluorescent protein
FCCP	Carbonyl cyanide-4-phenylhydrazone
FP	fluorescent protein
FRET	Förster/fluorescent resonance energy transfer
GFP	green fluorescent protein
GSH	glutathione
HEK	human embryonic kidney cells
HEPES	4-(2-hydroxyethyl)-1-piperazineethanesulfonic acid
MOPS	3-(N-morpholino)propanesulfonic acid
N2a	mouse neuroblastoma cells
NAC	N-acetyl cysteine
mXFP	monomeric fluorescent protein (any color)
RFP	red fluorescent protein
ROS	reactive oxygen species
roGFP	reduction-oxidation sensitive green fluorescent protein
s.e.m.	standard error of the mean
stdev	standard deviation
wt	wild type
YFP	yellow fluorescent protein

ABSTRACT

Author: Trull, Keelan, J. PhD
Institution: Purdue University
Degree Received: August 2019
Title: Engineering Fluorescent Biosensors for Interrogating Biologically Relevant Chemical Species
Committee Chair: Mathew Tantama

Fluorescent proteins and the biosensors created with them have been used extensively to monitor chemical species inside and outside of the cell. They have been used to increase our knowledge of cellular function in normal and diseased states. Fluorescent biosensors are advantageous because they can be genetically encoded, do not require exogenous reagents, and can be quantitative. Fluorescent biosensors are also able to measure analytes with high spatial and temporal resolutions, enabling measurements at the scale of physiological events. In this thesis efforts have made to increase the available fluorescent biosensor tools for imaging cellular events. This work includes creation of new sensors for two molecules not yet detectable via fluorescent protein biosensor, acetylcholine and adenosine diphosphate. Efforts were also made to improve the current available biosensors for adenosine triphosphate and cellular redox, to make them more compatible with multiplex and deep tissue imaging. Here I present my work to design, characterize and utilize these fluorescent biosensors.

CHAPTER 1. INTRODUCTION

1.1 Fluorescent Protein Based Biosensors

When green fluorescent protein (GFP) was first cloned and expressed in bacteria and *C. elegans* it was a groundbreaking discovery that paved the way for a deluge of biological discoveries[1]. As a genetically encoded fluorescent indicator, it allowed scientist to easily track anything from cell subtypes to tumor growth, and even to track of protein localization within cells[2–7]. The discovery of GFP also created the field of genetically encoded fluorescent biosensors, which has since exploded. With the discovery of red fluorescent proteins (RFP) derived from corals as well as the work to shift the spectral properties of GFP there are now a large pallet of fluorescent proteins available[8,9]. Using the variety of fluorescent proteins, researchers have developed a wide array of biosensors capable of detecting a vast number of cellular species[10].

Fluorescent biosensors can be broadly separated into two categories based on the type of signal they output, intensiometric or ratiometric. Intensiometric sensors output signals that are measured by changes in intensity based on the response to changes in the analyte. These types of sensors are generally more difficult to use quantitatively because the signal can be more easily affected by expression levels and bleaching artifacts. Ratiometric sensors are measured via two distinct signals, one that is directly proportionate to changes in the analyte and another that is indirectly proportionate to those same changes. This allows the derivation of a ratio and makes these types of sensors intrinsically quantitative. Such sensors are less likely to be affected by changes in protein expression or bleaching of the sensor. Since ratiometric sensors are less likely to be affected by these artifacts, they are generally considered more useful. However, this is not to say that intensiometric sensors are not useful, they are well suited to take event-based measurements and because ratiometric sensor require multiple signal outputs they take up more spectral space than intensiometric sensors, thus limiting their use in multiplex imaging.

There are a few basic ways in which a biosensor can be created: 1) alter the structure of the fluorescent protein (FP) itself so that it becomes sensitive to an analyte 2) fuse a single FP to another protein domain that confers sensitivity to an analyte 3) fuse two or more FPs to another protein domain that is sensitive to analyte and thus changes the way the FPs interact with each other.

Biosensors that rely on alterations made directly to the fluorescent protein are generally capable of detecting cellular species that can directly react with or bind to individual amino acids in proteins in general, such as pH and reactive oxygen species (ROS). Some examples of this type of sensor are the pH sensors pHluorin[11], pHRed[12], and mCherryEA[13] that utilize the innate pH sensitivity of FPs, conferred by the hydroxyl group in the chromophore, but improve upon it by mutating key residues surrounding the chromophore. Other examples are the redox sensitive sensors, the roGFPs[14,15], which have cysteines engineered close to the chromophore which can be reduced or oxidized thus forming or breaking a disulfide bridge which then causes strain the on the β-barrel, altering fluorescence. This type of sensor is great for detecting smaller molecules that can easily alter amino acids sidechains (via disulfide bond formation or protonation/deprotonation events, etc.), but to detect larger and more varied molecules biosensors require a sensing domain.

Sensing domains are usually proteins or parts of proteins that natively bind the substrate of interest and have a conformational change upon binding that specific substrate. The conformational change in the sensing domain is relayed to the FP which then causes a measurable change in the fluorescence. Sensing domains can be from any type of organism, from periplasmic binding domains of bacterial ABC-transporters to human G-protein coupled receptors. When fused to a single FP, these sensing domains can be used to create intensiometric probes such as GACh[16], MaLions[17], GCaMPs[18],and ArcLight[19], for acetylcholine, ATP, Ca^{2+}, and cell potential respectively. Single FP fusions can also be used to make ratiometric sensor such as Perceval[20], the Queens[21], GEM-GECO[22], and REX-GECO[23] which can quantitatively measure ADP/ATP ratio, ATP, and calcium.

By fusing two FPs to a sensing domain you can create a ratiometric biosensor that utilizes Förster resonance energy transfer (FRET) as a sensing paradigm. FRET is a non-radiative energy transfer between two chromophores and the efficiency of that transfer is based on spectral overlap, relative distance, and orientation of the two chromophores. Therefore, in order to create a FRET based sensor the conformational change of the sensing domain must alter the relative distance or orientation between the two FPs. This technique has been used to create many sensors, including ATeam[24], Twitch[25], and AKAR[26] which can detect ATP, calcium, and PKA activity.

While there are a multitude of sensors available, there is also a preponderance of improvements that can be made, including enhancing dynamic range, sensitivity, and signal-to-noise of current sensors. In addition, new sensors need to be developed that are ratiometric or red-

shifted versions of those currently available, allowing quantitative and multiples imaging respectively. There are also many biologically relevant molecules that do not currently have a biosensor capable of specifically detecting them including ADP and adenosine.

In this thesis I will discuss my efforts to make improved biosensors for acetylcholine, ATP, ADP, and cellular redox.

1.2 Cholinergic sensors

Cholinergic signaling, mediated by acetylcholine, has been shown to affect movement and cognitive function in the prefrontal cortex, with observed changes in attention and cue detection[27–29]. In neurological diseases such as Parkinson's and Alzheimer's, these functions have been shown to deteriorate in parallel with loss of cholinergic neuron function in various regions of the brain[30–32]. There is also evidence to suggest that individuals with autism spectrum disorders have decreased levels of nicotinic acetylcholine receptors, which are involved in cholinergic signaling, in the cerebellum as well as the prefrontal and parietal cortices[33]. Although acetylcholine is known to be involved in these behavioral and disease states, there remains a distinct gap in knowledge about how cholinergic signals propagate, affect pathways, and become altered in these various disorders[34].

To address this problem, tools are needed to quantitatively measure fluctuating levels of acetylcholine within the timescale of neurological signaling (ms-s) and the spatial area of a cholinergic circuit (nm-cm). Current methods for the detection of acetylcholine or its byproduct choline typically involve micro-dialysis and electrochemical sensors. These techniques have allowed for the determination of the accepted 5-10 μM general physiological range of extracellular choline[35–37]. Using these techniques, normal and dysregulated cholinergic signaling has also been observed[38–41]. However, both microdialysis and microelectrode techniques limit the spatial and temporal resolution of the measurement, as well as potentially cause damage and scaring to the tissue, which can alter cellular behavior[42]. These limits in our current ability to monitor cholinergic signaling in brain regions require the development of new tools that can accurately track acetylcholine release, diffusion, and clearance with high resolution.

Fluorescent biosensors offer a method to both increase resolution, as well as quantitatively measure levels of biomarkers, monitor cell signaling, and track enzyme activity[43,44]. Currently there are biosensors that can be used to study cholinergic signaling indirectly. This can be achieved

by measuring changes in secondary messengers, such as increased intracellular Ca^{+2}, caused by activation of muscarinic acetylcholine receptors[45–47]. Recently, a fluorescent biosensor for acetylcholine was published that used the muscarinic acetylcholine receptor as a sensing domain and circular permuted GFP (cpGFP) as the fluorescent reporter[16]. However, this sensor is intensiometric, and while it was shown to be useful in monitoring acetylcholine release it could not be used to quantitate extracellular levels. Also, because the sensing domain is an integral membrane protein there is a need for a soluble biosensor for acetylcholine.

1.3 ATP

Adenosine triphosphate (ATP) is an important cellular molecule; it acts as the energy currency of the cell, is involved in post translational modification, and is an important signaling molecule.

Due to ATP's importance in cellular biology, it is no surprise that there are many available methods for measurement of ATP, including a veritable menagerie of fluorescent biosensors including Perceval, the ATeam sensors, and the Queen sensors. Perceval is a ratiometric yellow sensor capable of measuring the ATP to ADP ratio inside of cells[20,48]. The ATeam sensors are FRET-based biosensors that use the epsilon subunit from various bacterial ATP synthases to measure multiple ranges of ATP concentrations[24]. The Queen family of ATP sensors are another type of ATP sensor that utilizes the same epsilon subunits, but Queen only uses one fluorescent protein, cpEGFP, as the reporter[21]. These sensors have time and again been shown useful for measuring ATP concentrations inside and outside of the cell[20,21,24,48,49], but they have one limiting characteristic, they all occupy the cyan-yellow spectral space. This limits their use for multiplex imaging with other cyan-yellow sensors and monitoring ATP in multiple subcellular locals. It also limits their use in deeper tissue imaging experiments because their excitation and emission wavelengths are easily absorbed by and can cause damage to tissue. To solve these two problems, there is a need for sensors that are red shifted and are compatible with deep tissue imaging. Some newly minted sensors help to partially fill this need. The MaLionR sensor is a red ATP sensor that was recently developed[17]. However, because it is an intensiometric sensor, it cannot be used to quantitate ATP concentrations and can only be used to observe changes. ATP sensors have also been created using a single FP paired with a luminescent protein, and they use bioluminescence resonance energy transfer (BRET) to detect changes in ATP. Both the NanoLantern family of

sensors and the BTeam sensors use this approach[50,51]. However, there are still issues with using these sensors in tissue due to the yellow emission light from the acceptor FPs. So, there is still a need for red-shifted and deep tissue compatible ratiometric sensors for detecting ATP.

1.4 ADP

Purinergic signaling is involved in pain sensation, immune responses and neuronal-glial communication and is mediated mainly by ATP, ADP, and adenosine[52–57]. To better understand the dynamics of purinergic signaling we need to be able to follow changes in the extracellular concentrations of both ATP and ADP.

Existing sensors for measuring ATP, including the Queen and ATeam sensors, can be used to measure extracellular ATP. In fact, the ATeam sensors have been successfully targeted to the extracellular membrane and used to measure changes in ATP concentrations in the extracellular space[49]. What is now needed are sensors for the other component of purinergic signaling, ADP. A sensor for ADP has been developed using a bacterial actin-like protein, ParM, as the sensing domain and various synthetic dyes as the reporters[58,59]. However, because they require dyes to function, these sensors have only been used in plate-based assays and have yet to be incorporated into cells[58,59]. There is still an evident need for a fully genetically encoded biosensor capable of detecting ADP in the extracellular space.

1.5 Redox

The balance of reduction-oxidation (redox) reactions inside of living cells is imperative for maintaining cell health. This balance is generally maintained by a redox network made up of enzymatic and non-enzymatic buffers like glutathione[60–62]. Loss of that balance has been known to lead to certain disease states in aging, cancer, and Parkinson's disease among others[63–66]. Regulated levels reactive oxygen species (ROS) are involved in normal metabolism and signaling, but as ROS levels become elevated above what the redox network can handle, it can begin to cause cellular damage than can lead to cell death[67]. To fully understand the redox network inside of cells, we must take into account the different redox networks in different organelles and how these redox networks interact with each other[68–73].

Currently tools exist that enable us to shed light on the redox networks inside of cells. The roGFP family of fluorescent biosensors are one set of such tools[14,15]. The roGFPs are ratiometric sensors of redox potentials, so they allow for the quantitative measurement of redox networks inside of cells. These sensors can also be fused with cellular redox enzymes such as, glutaredoxin-1 (Grx1) and oxidant receptor peroxidase-1 (Orp1), to improve kinetics and make them specific for glutathione and hydrogen peroxide respectively[74].

Unfortunately, because the roGFP-based sensors all emit green fluorescence, accurately measuring redox dynamics in multiple subcellular compartments is not feasible. There some available red fluorescent redox sensors, HyPerRed[75] and rxRFP[76], but unlike the roGFPs, these sensors are not ratiometric, and they can only be used to observe relative changes and are not quantitative.

Therefore, there is a distinct need for a red shifted ratiometric biosensor capable of detecting changes to the redox environment inside of cells.

It is therefore the goal of this body of work to create new fluorescent biosensors that fill the gaps in our current toolbox. This thesis will present our work toward creating a soluble and ratiometric fluorescent sensor capable of detect acetylcholine. This work also includes our progress toward improved sensors for detecting ATP in the red wavelengths and in deep tissue. We also made significant progress in the creation of a fully genetically encoded biosensor capable of detecting ADP on the extracellular side of the plasma membrane. Finally, we successfully created a red, ratiometric sensor that can be used to measure the redox status of cellular organelles simultaneously with the roGFPs.

CHAPTER 2. ENGINEERING A FLUORESCENT BIOSENSOR FOR MEASURING CHOLINERGIC SIGNALING

2.1 Introduction

Acetylcholine is a neurotransmitter that is involved in motor control, learning, and attention. It is thought that acetylcholine can act through volume transmission as well as traditional fast synaptic transmission[42,77–80]. Acting as a neuromodulator, acetylcholine can affect the underlying mechanism of complex behaviors by modulating excitability, influencing the release of other neurotransmitters, inducing synaptic plasticity, and coordinating firing amongst neurons[78]. Acetylcholine acts through two types of receptors, nicotinic ion-channels and muscarinic G-protein coupled receptors. Cholinergic signaling is implicated in relaying sensory information in mice and *C. elegans*[81,82]. Basal forebrain projections into the prefrontal cortex have also been shown to use cholinergic signaling in attention and cue detection tasks[28,81]. Acetylcholine release in the striatum, which is heavily involved in motor control, has been shown to cause synaptic release of dopamine and γ-aminobutyric acid (GABA) in the striatum without inducing an action potential[83–85]. Substantia nigra dopaminergic neurons innervate the striatum and are involved in the regulation of the tonic firing rate of striatal cholinergic interneurons[86,87].

Many pathological states involve dysfunction of cholinergic signaling. For example, in Parkinson's disease, the death of dopaminergic neurons in the substantia nigra drastically decreases the concentration of dopamine released in the striatum. It has been observed that as dopamine levels decrease, striatal release of acetylcholine increases[88,89]. In the prefrontal cortex cholinergic signaling has been shown to affect movement as well as cognitive functions like attention and cue detection. In neurological diseases, including Parkinson's disease and Alzheimer's, these functions have been shown to deteriorate in parallel with the loss of function of cholinergic neurons in different brain regions[30–32]. There is also evidence showing that there are lower levels of nicotinic acetylcholine receptors, involved in cholinergic signaling, in the cerebellum and prefrontal cortex of individuals with autism spectrum disorders[33]. In these cases, there is some understanding about which neurons play a role in cholinergic signaling. However, at present there is a distinct gap in our knowledge about how acetylcholine release and clearance dynamics affect these behaviors and how they are altered in different diseases and disorders[34]. This

gap in knowledge has persisted because we need methods to directly observe acetylcholine levels in intact tissue.

Current methods of detecting acetylcholine include the use of microelectrodes, and microdialysis coupled to liquid chromatography or mass spectrometry[38–40]. Using these methods, normal extracellular acetylcholine levels have been measured at 5-10 μM concentrations, aberrant cholinergic signaling has been detected in Alzheimer's disease, and they have significantly advanced our understanding of how acetylcholine can act as a neuromodulator. However, current methods do have their limitations often because they rely on indirect signals or they lack spatial and temporal resolution, limiting our ability to fully study the dynamics of cholinergic signaling[35–37,39,77,90]. For example, the use of microelectrodes requires coupling them with enzymes to detect acetylcholine and choline, typically acetylcholinesterase and choline oxidase respectively. These microelectrodes can still be affected by other electroactive biomolecules *in vivo* and can also cause significant scarring[38,42].

In contrast to microelectrodes and microdialysis probes, genetically encoded fluorescent protein sensors offer a much less invasive way to image cellular processes in real-time and at cellular resolutions. Currently, sensors have been designed for use in live cells to image metabolite concentrations and signaling pathways[43,44]. The CNiFER sensors have been used to image acetylcholine release, the sensor expressed on adjacent cells detects acetylcholine when it binds to its receptor. This then causes intracellular calcium levels to increase which is monitored with the calcium indicator TN-XXL[45,47]. Since these sensors rely on detecting changing levels of secondary messengers this leads to an indirect measurement of cholinergic signaling[45,46]. Recently, a new sensor has been developed that is capable of directly measuring cholinergic signaling by measuring sensor binding. The GACh sensor is a fusion of cpGFP and the muscarinic acetylcholine receptor, a GPCR. When acetylcholine binds to the receptor portion of the sensor, it causes an increase in the intensity of green emitted light. GACh was shown to be capable of measuring cholinergic signaling in cultured neurons and pancreatic cells as well as in live fruit flies and mice[16]. However, because part of the sensor is an integral membrane protein, the GACh sensor is not soluble and cannot be used elsewhere in the cell or fully characterized *in vitro*. Also, because the reporter is intensiometric this sensor can only detect release and clearance events and cannot be easily or accurately used to quantitatively measure extracellular concentrations of acetylcholine. Thus, there

remains a clear need for a soluble and ratiometric biosensor to directly detect acetylcholine, providing a scientific premise for this project.

2.2 Design of a Genetically Encoded Acetylcholine Biosensor

We engineered a fluorescent sensor for acetylcholine by fusing a sensing domain that binds to acetylcholine to a fluorescent protein reporting domain. Our sensing domain is the choline and acetylcholine binding protein, ChoX, of the ATP-binding cassette transporter ChoVWX from *Sinorhizobium meliloti*. We chose ChoX as our sensing domain because it is known to bind both acetylcholine and choline, and the crystal structures for the semi-open unbound form and the closed bound form have been reported[91–93]. ChoX undergoes a clam-shell-like closing motion upon binding its ligand, and this global closing motion also causes small localized conformational changes in various regions of the protein (Figure 1).

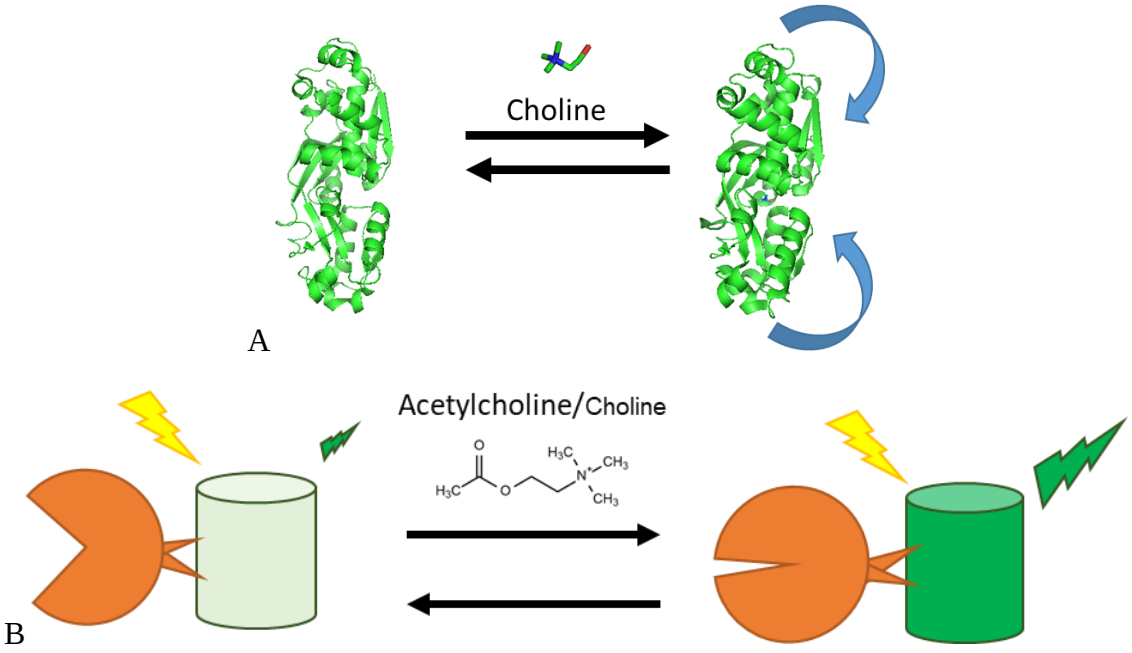

Figure 1 A. Comparison of the apo (PDB 2REJ) and bound (PDB 2REG) states of ChoX upon binding its ligand[92]. B. Cartoon of the acetylcholine biosensor design in which ChoX, the sensing domain, is coupled to a circularly permuted GFP (cpGFP), the reporting domain.

By comparing the crystal structures of the unbound semi-open form to the bound closed form of ChoX, we identified sites, surface-exposed loops in particular, which experience

conformational changes. Site selection was based on a gain or loss of β-sheets, changes in the dihedral angle between amino acids, or spatial relocation of loops (Figure 2). We also compared the structure of ChoX to a maltose-binding protein and a glutamate-binding protein used previously to create similar sensors, to identify sites other groups have used that are structurally homologous to ChoX[94,95].

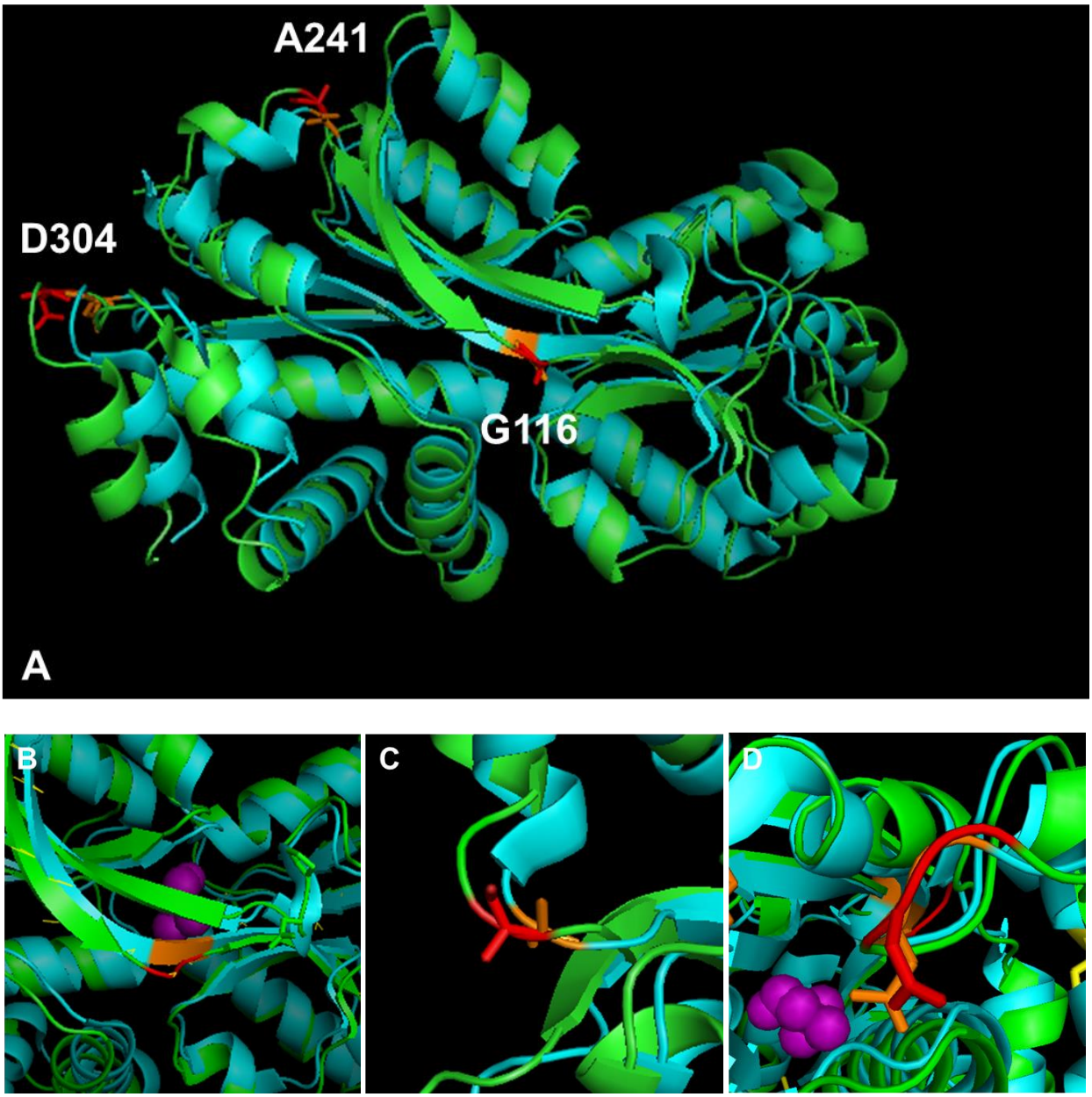

Figure 2 Selected insertions sites in ChoX. A) Alignment of the bound, closed state in cyan (2REG)[92] with the apo semi-open state in green (2REJ)[92] with selected insertion sites at G116, A241, and D304 highlighted. B) Position 116 was selected because of the conformational change upon binding to choline and its location within the hinge region C) Position 241 was selected because it is structurally similar to a site selected for creating a maltose sensor[94] D) Position 304 was selected because it is surface exposed and shows a slight shift upon binding to choline.

Using this information, we then designed fluorescent sensor candidates in which ChoX is fused to cpEGFP at the sites that were identified to undergo a ligand-dependent conformational change. cpEGFP is a version of EGFP that has been mutated to have its N- and C- termini moved

closer in proximity to the chromophore, allowing us to more easily affect the fluorescence. By fusing cpEGFP to a site in ChoX that has a conformational change, acetylcholine binding may be able to induce a change in the structure of cpEGFP that will measurably affect its fluorescence[18,43,44,94]. The N- and C-termini of cpEGFP were fused to ChoX using short peptide linkers that are also genetically encoded.

To fully optimize the acetylcholine biosensor, several candidates were created, each testing one of the multiple potential cpEGFP insertion sites in ChoX that were chosen based on the criteria stated above.

2.3 Characterization of First Round Sensor Candidates

Three versions of the ChoX-cpEGFP biosensor were initially designed and tested for response to choline as a feasibility study (Figure 2). Remarkably, one of the three sensors showed a response when the concentration of choline is increased (Figure 3 & 4). Here, we initially used choline as a ligand because ChoX has higher affinity to choline compared to acetylcholine[92,93] and to mitigate concerns about uncatalyzed acetylcholine hydrolysis during processing. The most promising candidate, with the cpEGFP inserted after glycine 116 (Figure 5), showed incremental decreases in fluorescence intensity when the concentration of choline is increased from 1 nM to 1 mM (Figure 3). This biosensor responds with an approximate K_d – 482±127nM (mean ± stdev n=3) (Figure 4), which is increased in affinity compared to the native K_d of the original choline binding protein (2.3 ± 1.0 µM)[92,93]. The other two biosensor candidates did not show a consistent fluorescence change with the addition of choline. Therefore, we focused initially on the first candidate.

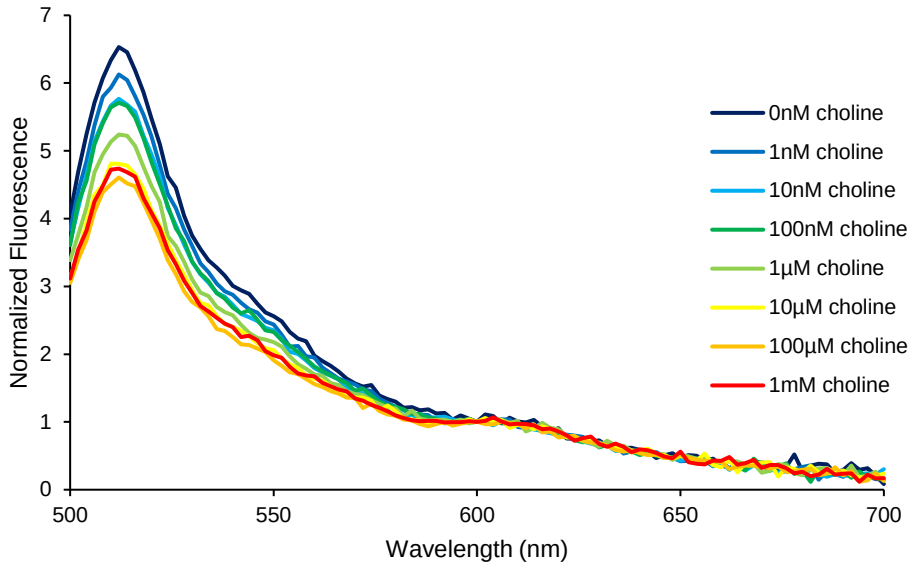

Figure 3 Fluorescent emission spectra of the most promising candidate from the initial set of acetylcholine sensors, ChoX-116cpEGFP, in the presence of increasing concentrations of choline. This construct was fused to a RFP, mCherry, to normalize the spectra.

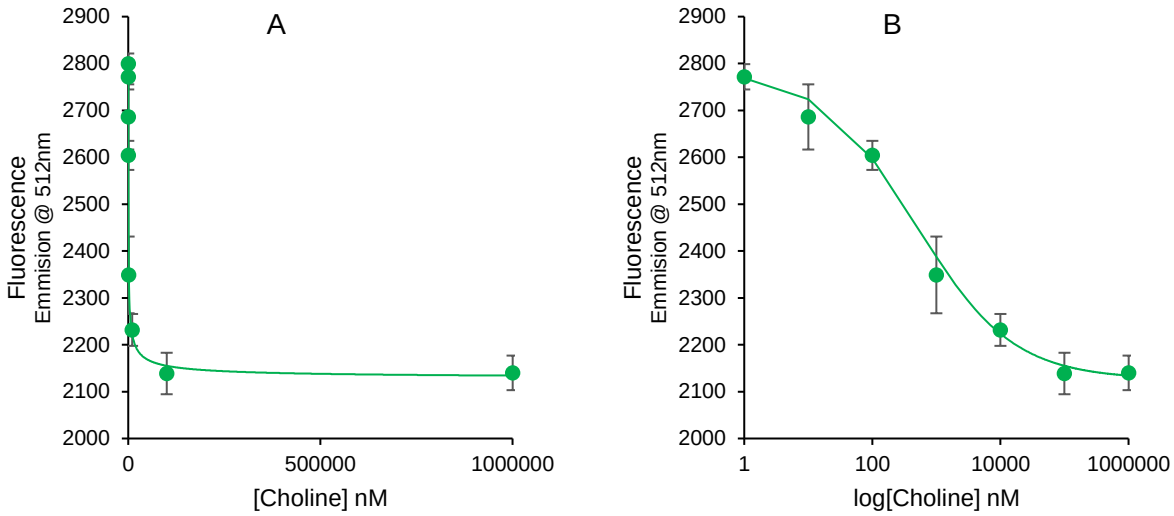

Figure 4 Choline dose response curve of ChoX-116 sensor candidate. K_d - 482±127nM (n=3 mean ± stdev)

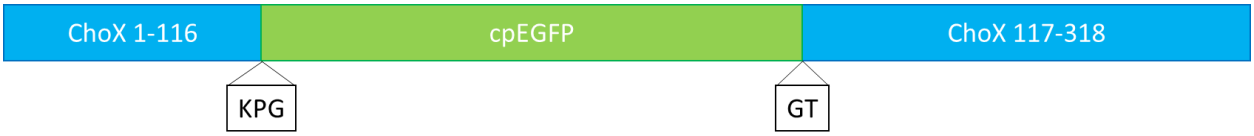

Figure 5 Diagram of the ChoX-116 construct with cpEGFP inserted into the ChoX protein after glycine 116. Diagram also show the amino acid makeup of the two linkers that connect ChoX to cpEGFP.

After discovering that the ChoX-116 sensor responded to changes in choline concentration, we tested to see if it had the ability to detect changes in the acetylcholine concentration. We observed the same decrease in fluorescence as before upon addition of increasing concentrations of acetylcholine (Figure 6). From this data we estimated the K_d for acetylcholine to be 44.1±88.4µM (mean ± stdev n=3) (Figure 7), which is within a similar range as the native ChoX protein (100±12µM)[92].

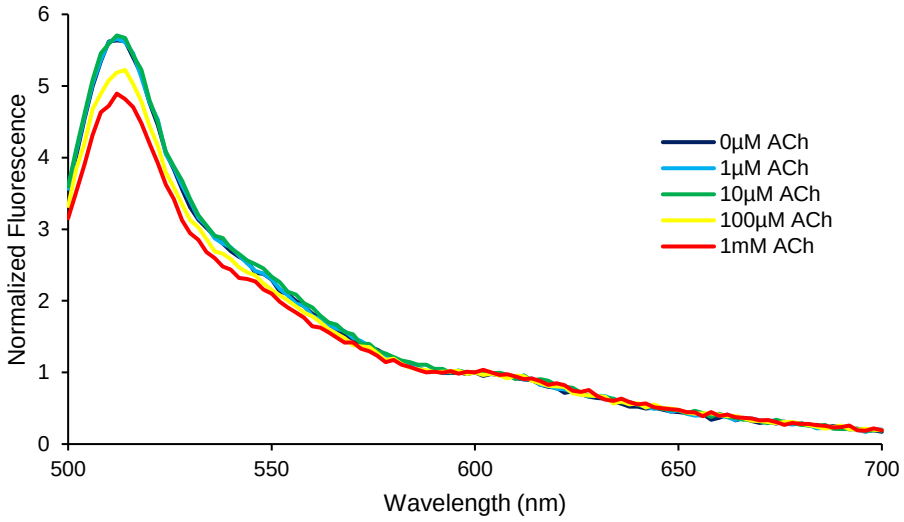

Figure 6 Fluorescent emission spectra of ChoX-116 in the presence of increasing concentrations of acetylcholine. Normalized to the emission peak of mCherry fused to the N-terminus.

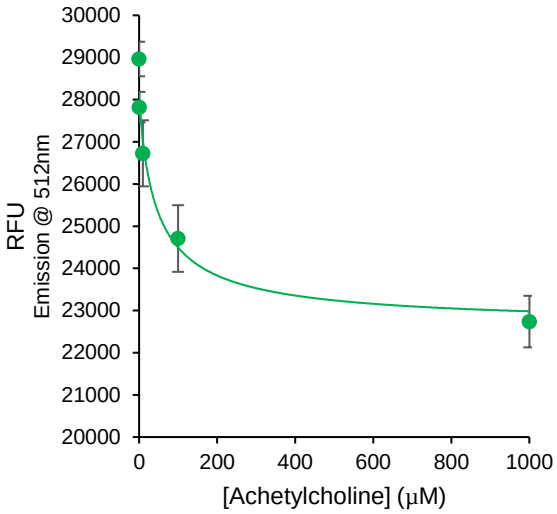

Figure 7 Acetylcholine dose response curve for sensor candidate ChoX-116. K_d – 44.1±88.4µM (n=3 mean ± stdev)

2.4 Conclusions and Future Directions

Though our best sensor candidate is not ratiometric, we were able to create a soluble fluorescent biosensor capable of detecting acetylcholine. This sensor lays the groundwork for future generations of sensors that will be able to fill the gap in our current acetylcholine sensing technology.

Optimization of this sensor could include tinkering with the FP and linkers to create a ratiometric sensor with greater dynamic range. Directed evolution is also an option that maybe useful in tuning the sensitivity to acetylcholine and choline so that the sensor is more sensitive to the former.

2.5 Methods

The ChoX gene was created as G-block from IDT and was designed to be inserted directly into the pRsetB vector directly using Gibson assembly. Sensors were constructed by Gibson Assembly using the NEB HiFi kit. Sensors were tagged with mCherry, an RFP, on the N-terminal end so that the fluorescent could be easily normalized.

Sensor candidates were expressed as His-tagged protein in BL21(DE3) *E. coli* and purified by nickel-affinity chromatography. Protein concentrations were obtained using a BCA assay.

The fluorescence choline and acetylcholine dose-response curves for purified protein solutions were measured on a BioTek Synergy H4 multi-mode microplate reader at ambient temperature. Assays were run in a MOPS + Mg^{2+} buffer (100mM MOPS, 50mM KCl, 5mM NaCl, 0.5mM $MgCl_2$, 0.1% BSA). Choline or acetylcholine was added repeatedly to a single well at increased concentrations, excitation and emissions scans were performed after every addition.

CHAPTER 3. ENABLING MULTIPLEX IMAGING OF ATP WITH RED EMITTING BIOSENSORS

3.1 Introduction

ATP is an important cellular molecule; it acts as the energy currency of the cell, is involved in post translational modification, and is an important signaling molecule.

As such, there have been a multitude of fluorescent protein-based sensors designed to monitor ATP levels. Perceval is one such sensor that is ideal for detecting energy levels inside of cells by monitoring the ATP to ADP ratio[20,48]. Perceval and its subsequent generations enable us to monitor overall cell health as measured by energy levels by ratiometrically shifting the two excitation peaks of a yellow fluorescent protein[20,48]. Another sensor that has been designed to answer questions focused on cellular ATP levels is the ATeam family of sensors[24]. ATeam uses the epsilon subunit from bacterial ATP synthases as a sensing domain and a cyan-yellow pair of fluorescent proteins that can be used to measure a FRET response[24]. Since FRET is an innately ratiometric measurement, the ATeam sensors can easily be used to quantitate the amount of ATP inside of cells. It has also been shown that epsilon subunits from different species of bacteria can be used and combined to tune the specificity of ATeam to a range that is useful for any application[24]. The Queen family of ATP sensors are another type of ATP sensor that utilizes the same epsilon subunit used in the ATeam sensors, but Queen only uses one fluorescent protein, cpEGFP, as the reporter[21]. Since cpEGFP has two excitation peaks, the Queen sensor are also ratiometric and quantitative like ATeam. As with the ATeam sensors, the epsilon subunit used in the Queen sensors can also be tuned to specifically fit the needs of different systems with different expected ATP concentrations.

While the all of these sensors have proven useful for measuring ATP, they have one limiting characteristic, they all occupy the cyan-yellow spectral space. This is limiting because: 1) many current sensors occupy the same spectral space, limiting their use to simultaneously make measurements of different analytes or in different sub-cellular compartments and 2) cyan-yellow fluorescent biosensors are not as useful for imaging deeper within tissue because the excitation and emission wavelengths are more easily absorbed by and can cause damage to the tissue. To solve these two problems, we have designed two sensors, a red fluorescent protein-based ATP

sensor to enable multiplex imaging and a bioluminescent resonance energy transfer (BRET) based ATP sensor for *in vivo* and in tissue imaging.

3.2 Red Shifting the Queen Family of ATP sensors

By utilizing the same sensing domain as the ATeam and Queen sensors, the epsilon subunit, but replacing the reporting domain with a red fluorescent protein we aimed to create a ratiometric, red fluorescent biosensor capable of detecting ATP within multiple physiologically relevant ranges (Figure 8)[21,24]. This would allow for the simultaneous detection of ATP in multiple different subcellular compartments, as well as enable the use of another cyan-yellow sensor at the same time as these red ATP sensors.

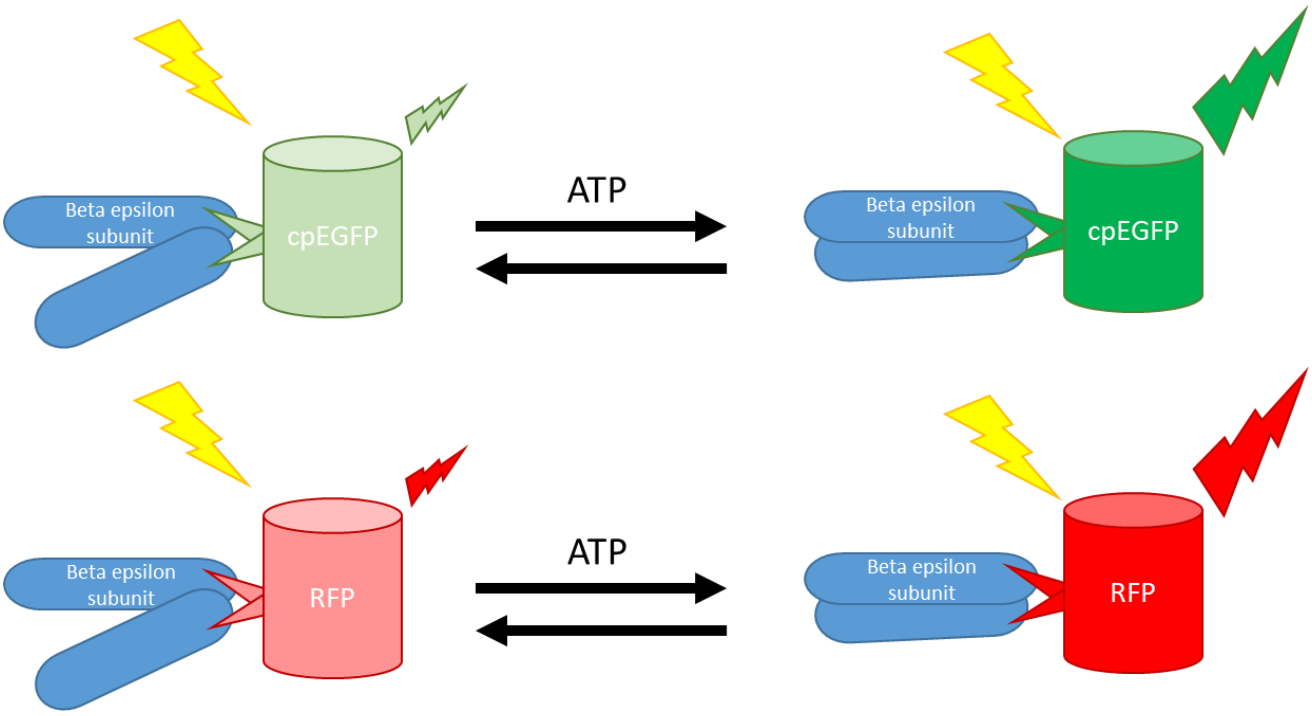

Figure 8 Diagram of the Queen ATP sensors and the proposed Red Queen ATP sensors.

In designing the Red Queen sensors, we planned to utilize cpRFPs that had previously been used in other red fluorescent biosensors and had decent dynamic ranges (Table 1). This approach was previously successfully applied for the creation of a wide spectral range of calcium sensors[22]. Due to the important role linkers play in creation of fluorescent protein-based biosensors, our first

attempts to create the Red Queens included a linker library. This library included linkers designed based on the linkers originally cloned into the Queen sensors as well as the linkers found in the red sensors which we are pulling the RFPs from.

Table 1 RFPs selected to create Red Queens R-GECO[46], REX-GECO[23], and RCaMP[96]

Parent Sensor	Fluorescent Protein	Circular Permutation	Excitation Wavelength	Emission Wavelength	Dynamic Range
R-GECO1.2	mApple	145	445, 557	600	16
REX-GECO1	mApple mutant	145	480	585	100
RCaMP1h	mRuby	142	571	594	10.5

However, after cloning the three libraries, one for each RFP, we ran into difficulties expressing our Red Queens in a format that was compatible with higher throughput screens (Figure 9). After screening more than 300 colonies over a four-month period we still had not achieved a good level of expression or any measurable response to changing ATP levels. We attempted to resolve this issue by screening a multitude of expression conditions including four types of media, three different expression time courses, three expression temperatures, two different culture volumes, and three bacterial cell lines to no avail. Circularly permuted RFPs are known to be notoriously finicky and difficult to work with. Native RFPs require good access to oxygen to properly mature and it is difficult to achieve the proper level of aeration in a 96-well format and cpRFPs compound the problem because the new termini can further impair maturation. This severely limited our ability to make progress in the production of these sensors. Even when we were able to achieve some level of expression and were able to screen the library with methods previously described[21] the sensor candidates showed no response (Figure 9A). These non-responders likely had linkers that were able to ensure maturation but were not able to transfer the conformational change from the ε-subunit to the RFP. While we were troubleshooting our expression system, a set of red, green, and blue ATP sensors were published[17]. However, these sensors are intensiometric and cannot be used quantitatively. Therefore, the Red Queens are still poised to be the first ratiometric red fluorescent biosensors of ATP as our work continues.

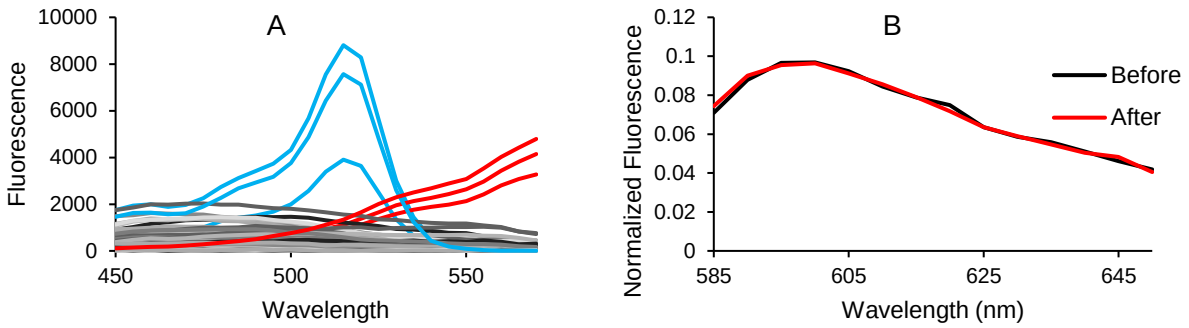

Figure 9 Spectra from library screens of Red Queen ATP sensors detailing the difficulties encountered. A) Poor expression of the Red Queen library (gray) when the positive controls (ATeam, blue & RCaMP1h, red) express well. As a note, this library screened the REX sensors, which have different spectral properties when compared to the RCaMP control, which is why the red peak is not resolved B) Even with decent expression no change in fluorescence upon challenge with KCN was observed

3.3 Creating a BRET based Biosensor for ATP

Another strategy to expand the color palette and overcome the issues green fluorescent sensors have with tissue penetration is to use some form of bioluminescence. Bioluminescent proteins do not require excitation light, so they are more ideal for deep tissue imaging, and they can also participate in resonance energy transfers with fluorescent proteins including RFPs[97]. Therefore, our aim was to create a BRET-based biosensor for detecting changes in ATP concentrations (Figure 10).

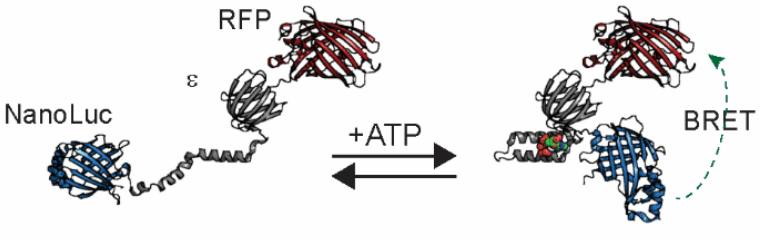

Figure 10 Sensor designs. Diagrams of a BRET-ATP sensor depict NanoLuc in blue, the *B. subtilis* ε-subunit in grey, and an RFP in red

Again, using the sensing domain from both the ATeam and Queen sensors, we planned on fusing the ε-subunit to a common bioluminescent protein, NanoLuc, as the energy transfer donor and an RFP to act as the acceptor[21,24,97,98]. NanoLuc has been shown to very efficiently transfer

energy to many color variants of fluorescent proteins including a GFP and a RFP[97]. We chose to initially try two different RFPs as the acceptor, tdTomato and one of its derivatives GRvTomato[99,100]. tdTomato was chosen because it is one of the brightest known RFPs and it has been shown to be a good BRET acceptor when paired with NanoLuc[97,99]. GRvTomato was chosen because one of the chromophores remains green and a GFP-NanoLuc pairing previously showed no residual bioluminescence making it an ideal candidate for a BRET sensor[97,100]. When paired together as an ATP sensor we were able to measure significant BRET between the NanoLuc and the respective RFP (Figure 11). From here we went onto more specifically test the response of these sensors to ATP.

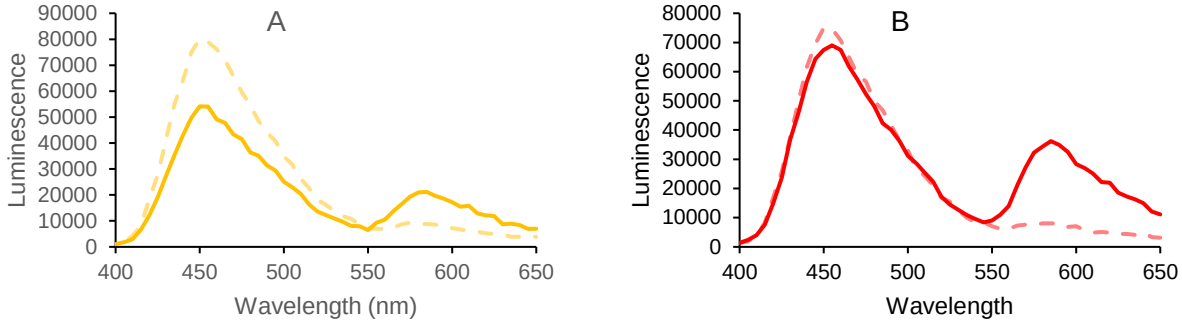

Figure 11 Spectra of NanoLuc-RFP fusions demonstrating BRET in between the NanoLuc Luciferase and the RFP A) GRvTomato and B) tdTomato. Solid lines are in the presence of 10mM ATP, dashed lines are with no ATP present.

We were able to measure an ATP dose dependent response for both the GRvTomato-NanoLuc sensor and the tdTomato-NanoLuc sensor (Figure 12). Both the GRvT-NanoLuc and the tdTomato-NanoLuc sensors had similar K_D's, 2.28±0.36mM and 2.36±0.40mM (mean ± stdev n=3) respectively, but the tdTomato-NanoLuc sensor had a greater dynamic range.

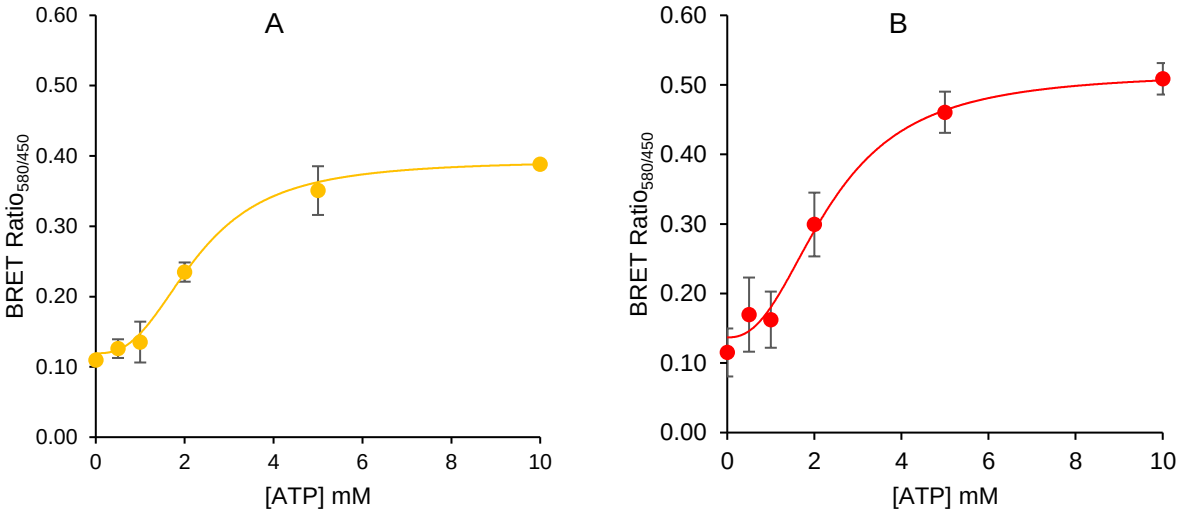

Figure 12 Dose responses of the two BRET based biosensors for ATP. A) The dose response of the Green-Red vine Tomato – epsilon subunit – NanoLuc fusion (n=3 mean ± stdev). B) The dose response of the tdTomato – epsilon subunit – NanoLuc fusion. Each point is an average, errors bars represent standard deviation, curve is derived from the fitting (n=3 mean ± stdev).

Though both sensors have decent dynamic ranges, they were further optimized by another member of the lab by testing different RFP acceptors. One of which, mScarlet[101], had an increase in the dynamic range and was then shown to be visible through mouse epidermis.

3.4 Conclusions

We have taken the first steps toward the creation of fluorescent ATP sensors that are useful in multiplex imaging and tissue imaging.

The design of the Red Queen sensors is still valid, because the MaLION sensors are qualitative[17], and with optimization of the expression system may lead to the first ratiometric red fluorescent biosensor capable of detecting ATP.

The RFP-NanoLuc sensors are the first red-shifted BRET sensors of ATP and are compatible with deeper tissue imaging experiments. The next step would be to demonstrate their usefulness by answering biological questions possibly in live mice. The epsilon subunit can also be exchanged or mutated to tune the specificity of these sensors so that they may be used in a multitude of different cellular environments.

3.5 Methods

Protein Engineering and Library Screen

Single FP Red ATP sensors

The three RFPs, cpmApple, cpREXApple, cpmRuby, were fused to the epsilon subunit from the Queen2m sensor by Gibson Assembly using the NEB HiFi master mix. These libraries were transformed into NEB BL21(DE3) GOLD *E. coli* for efficient transformation and expression. Libraries were expressed in 0.75mL of 1xYT media in deep-well 96 well plates overnight at 37^{o}C then for varying amounts of time at room temperature and 4^{o}C. Each library contained a media blank, pUC transformed bacterial control, bacteria expressing ATeam1.03 as an ATP-sensor positive control, and bacteria expressing RCaMP1h as a red sensor positive control.

Bacteria were then transferred to M9 minimal media (50mM Na2HPO4, 20mM KH2PO4, 20mM NH4Cl, 9mM NaCl, 2mM MgSO4, 0.1mM CaCl2, pH 7.5) and diluted to an OD600 of approximately 0.2. Fluorescent excitation and emission spectra were then measured: The cpmApple and cpmRuby libraries: Excitation spectra – excitation wavelengths 435-570/9nm 5nm steps emission wavelength 590/9nm. Emission spectra – excitation wavelength 565/9nm, emission wavelengths 585-650/9nm 5nm steps. The REXApple libraries: Excitation spectra – excitation wavelengths 450-565/9nm 5nm steps emission wavelength 585/9nm, Emission spectra – excitation wavelength 480/9 emission wavelengths 500-650/9nm 5nm steps. KCN was then added to a final concentration of 10mM, the cultures were incubated with the cyanide for 10 minutes before a second set of excitation and emission spectra were measured.

BRET-based ATP sensor

Sensors were constructed by Gibson Assembly using the NEB HiFi kit, sub-cloned into the pRSETB vector for expression as His-tagged protein in BL21(DE3) *E. coli* and purified by nickel-affinity chromatography. CeNL/pcDNA3 was a gift from Takeharu Nagai (Addgene plasmid # 85199), and pBad-HisB-GRvT (Addgene plasmid # 87363) was a gift from Robert Campbell.

The fluorescence and luminescence ATP dose-response curves for purified protein solutions were measured on a BioTek Synergy H4 multi-mode microplate reader at ambient temperature. Assays were performed in assay buffer (50mM MOPS-KOH 50mM KCl, 0.5mM $MgCl_2$, 0.05% Triton-X, pH-7.3) at protein concentrations of 1µM. ATP was added to each well in the entire plate, then well-by-well 100µL of coelenterazine solution was added and the luminescence spectra was measured. The coelenterazine solution had to be added immediately

before reading the spectra or else the signal would degrade before the entire plate could be measured.

CHAPTER 4. DEVELOPMENT OF A FULLY GENETICALLY ENCODED ADP BIOSENSOR

4.1 Introduction

Purinergic signaling is involved in pain sensation, immune responses and neuronal-glial communication[52–57]. Specifically, purinergic signaling is involved in the immune response of microglia after infection or injury within the central nervous system[53,102]. In most cases, activation and recruitment of the microglia can assist in reducing inflammation and clearing debris, however in some disease states such as stroke and Parkinson's disease, activation of microglia can exacerbate the damage already present in the CNS[103,104].

Adenosine triphosphate (ATP) is a major signaling molecule in purinergic pathways and once released can act on many cell surface receptors, similar to many other signaling mechanisms. However, ATP degradation products such as adenosine and adenosine diphosphate (ADP) also have the ability to initiate signaling cascades by binding to receptors[57,105,106]. To fully understand the dynamics of purinergic signaling we need to be able to follow changes in the extracellular concentrations of both ATP and ADP[107].

Using genetically encoded fluorescent biosensors to monitor ATP and ADP is advantageous because it does not require the addition of exogenous reagents and does little to perturb the normal function of the cell. Genetically encoded sensors are also useful because they can be used for *in vitro* work, cell-based systems, as well as *in vivo* model systems. There already exists a variety of sensors capable of measuring ATP, including the Queen sensors and the ATeam sensors[21,24]. The ATeam sensors have even been successfully targeted to the extracellular membrane and used to measure changes in ATP concentrations in the extracellular space[49]. All that remains is to develop a genetically encoded sensor for ADP that can be targeted to and used on the extracellular membrane.

ParM is a bacterial actin like protein that is involved plasmid separation and has a relatively high native affinity for ADP (2.4μM)[108]. While this high affinity for ADP is not ideal for making sensor that would be used inside of the cell, it is more suited for use as an extracellular sensor of ADP where the concentration of ADP can range from nM to μM[57,109,110]. While ParM also has a high native affinity for ATP (42nM)[108], certain mutations have been shown to decrease the ATP affinity so that ParM is as much as 400-fold more selective for ADP over ATP[58,59]. Previously

used in a semi-synthetic ADP sensor, this mutant ParM is an ideal candidate to use as a sensing domain for a fully genetically encoded sensor[58,59].

4.2 Designing of a Fully Genetically Encoded ADP Sensor

The general design for the sensor is similar to other strategies, where a binding domain has a major conformational change upon binding the molecule of interest is fused to a fluorescent reporter. The actin-like bacterial protein, ParM, has been shown to change conformations in a Venus flytrap motion upon binding ADP (Figure 13)[111].

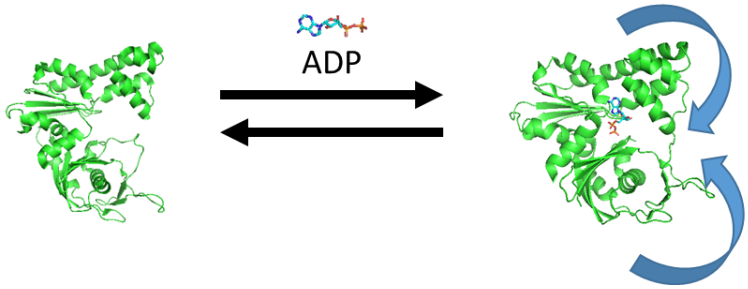

Figure 13 Crystal structure of ParM in the apo (1MWK)[111] and ADP bound (1MWM)[111] states.

We aimed to create a FRET based sensor by attaching two FRET compatible fluorescent proteins, monomeric teal fluorescent protein (mTFP1) and a yellow fluorescent protein (mVenus), at two points on ParM. Two strategies were developed to achieve this goal. One was to insert the FPs into the protein structure at points that moved closer to each other upon binding. The other approach was to attach the FPs onto the N- and C- termini. Using the insertion approach would most likely yield a sensor with a higher FRET change but may be difficult because we were inserting two relatively large amino acid sequences into the ParM structure which is likely to destabilize the protein. Using the termini is more likely to yield a properly folded protein, but because the termini are located close to each other and have very small movement upon binding, they are less likely to produce a sensor with large FRET changes. In order to maximize the chances of developing a sensor, we moved forward with both strategies, selecting six insertion sites on surface exposed loops and the two termini.

As FRET is dependent on not only the distance between the donor and acceptor but also the relative orientation of both chromophores in relation to each other. We hoped to optimize the

orientation using various circular permutations of both the donor and acceptor (Figure 14A)[112]. This library should allow us to sample multiple paired orientations to screen for a set that had low basal FRET and a large increase of FRET upon ADP binding. The second step in our library screens was designed in order to screen the linkers that connected the ParM sensing domain to the fluorescent proteins. Since the linkers are what connect the sensing domain to the reporting domain, they are responsible for relaying the conformational change from one domain to the other. Therefore, they must be optimized to best relay the binding motion, unfortunately, no consistent pattern has been observed across various fluorescent protein-based probes, so linker optimization can be more random[10]. To identify the best linkers between the sensing domain ParM and the two reporters, we engineered a second library with varying linker lengths (Figure 14B).

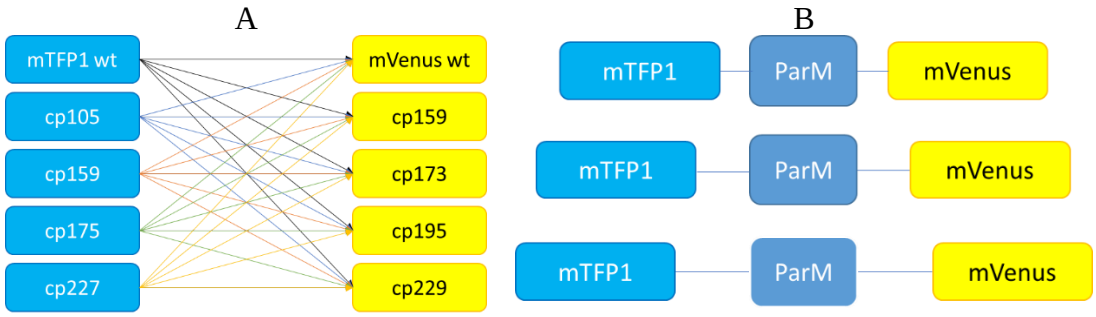

Figure 14 Design strategies for screening A) various circular permutations to optimize orientation B) various linker lengths to optimize dynamic range

4.3 Screening Sensor Candidates

To efficiently screen our sensor libraries, we utilized an assay previously employed to test a fluorescent ATP sensor, where *E. coli* expressing the sensors were exposed to cyanide. The assay was used to measure the change in FRET before and after the cyanide challenge to identify responders[21]. When used before the assay was measuring a decrease in ATP, but because we wanted to measure an increase in ADP, we needed to validate the assay for our purposes. To validate the assay, we performed a luciferase assay to measure ATP concentrations and we used pyruvate kinase and excess phosphor(enol)pyruvate (PEP) to convert ADP to ATP. By measuring the ATP concentrations with and without the pyruvate kinase and PEP we could calculate the amount of ADP present. With this set-up we were able to determine that the KCN challenge does cause a measurable increase in the amount of ADP present in *E. coli* (Table 2).

Table 2 Luciferase Assay (mean ± stdev, * data extrapolated from standard curve)

	ATP pmol	ADP pmol
Vehicle	2.84±0.43	0.13±0.20*
KCN	-0.30±0.04*	0.51±0.16

Using this assay with *E. coli* expressing the libraries of the ParM sensors, we initially screened the FP orientation library with the various circular permutated TFP and mVenus. From these initial libraries, hits were selected based on the presence of both FP emission peaks and a ratiometric change in both peaks upon cyanide challenge. We identified a total of eleven sensor candidates that met our criteria, nine hits were identified from terminal library and two from the insert library (Figure 15). The hits sampled most of the circularly permuted variations. Interestingly the 175 mTFP1 variant and the 229 mVenus variant were not included in these hits (Table 3). Another interesting point, the combination that would be later selected in the final screenings, wild type mTFP1 with the 157 variant of mVenus, was a hit in both the initial insert and terminal libraries (Table 3).

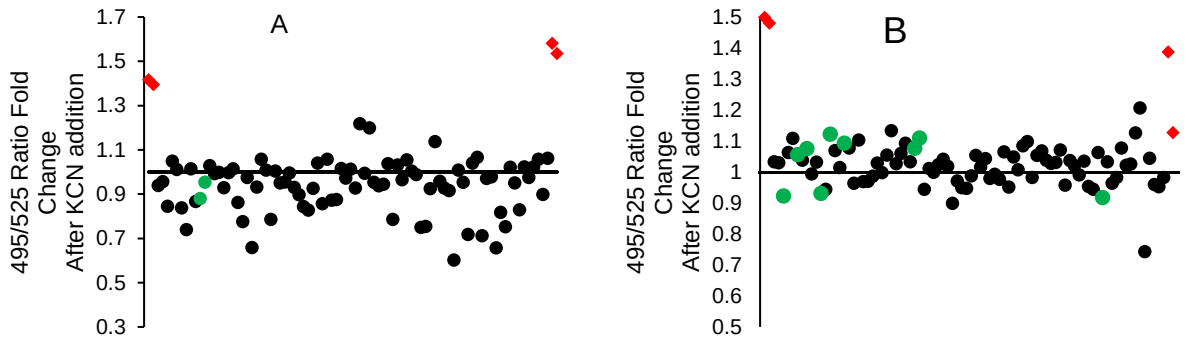

Figure 15 Results of the initial library screens black dots indicate a single sensor candidate, green dots are sensor candidates with both emission peaks present and a ratiometric change after KCN addition, red diamonds are the positive control, ATeam1.03 an ATP sensor A) Results of the library with the mTFP1 and mVenus variants inserted with in the ParM protein structure B) Results of the library with the mTFP1 and mVenus variants tagged on the N- and C- termini.

Table 3 Identity of the hits from the first round of sensor library screenings *Ter 3 was unable to be sequence verified

Hit ID	TFP variant	mVenus variant
Ins 1	wt	157
Ins 2	227	157
Ter 1	105	173
Ter 2	wt	157
Ter 3	*unk	*unk
Ter 4	wt	173
Ter 5	159	wt
Ter 6	wt	195
Ter 7	227	wt
Ter 8	227	195
Ter 9	227	173

At this point we decided to cease working with the insert constructs and focus on the terminal library. This was due to low overall expression and success of the library, along with the level of difficulty involved in cloning.

Using the pairs identified from the terminal library, we went on to our next planned library, screening the linkers in between the ParM sensing domain and the two FP reporters (Figure 14b). For the linker library we screened linkers of three different lengths, three, five, or seven amino acids, in between the mTFP and ParM (SGITSLY, SGITS, SGI) as well as the mVenus and the ParM (EVVIAAA, VIAAA, AAA). The composition of the linkers in this library came partially from necessity, based on the restriction enzymes sites used to accomplish the cloning strategy. The restriction enzymes sites used coded for a number of the amino acids selected. Those amino acids not assigned by restriction enzyme sites were chosen loosely based off of previous FRET sensors[24,112]. From this round of screening we identified three candidates with improved dynamic range in response to KCN addition (Figure 16). Upon sequence verification we discovered that all three of the hits had the same identity, $mTFP_{wt}$-SGITS-ParM-AAA-$cpmVenus_{157}$.

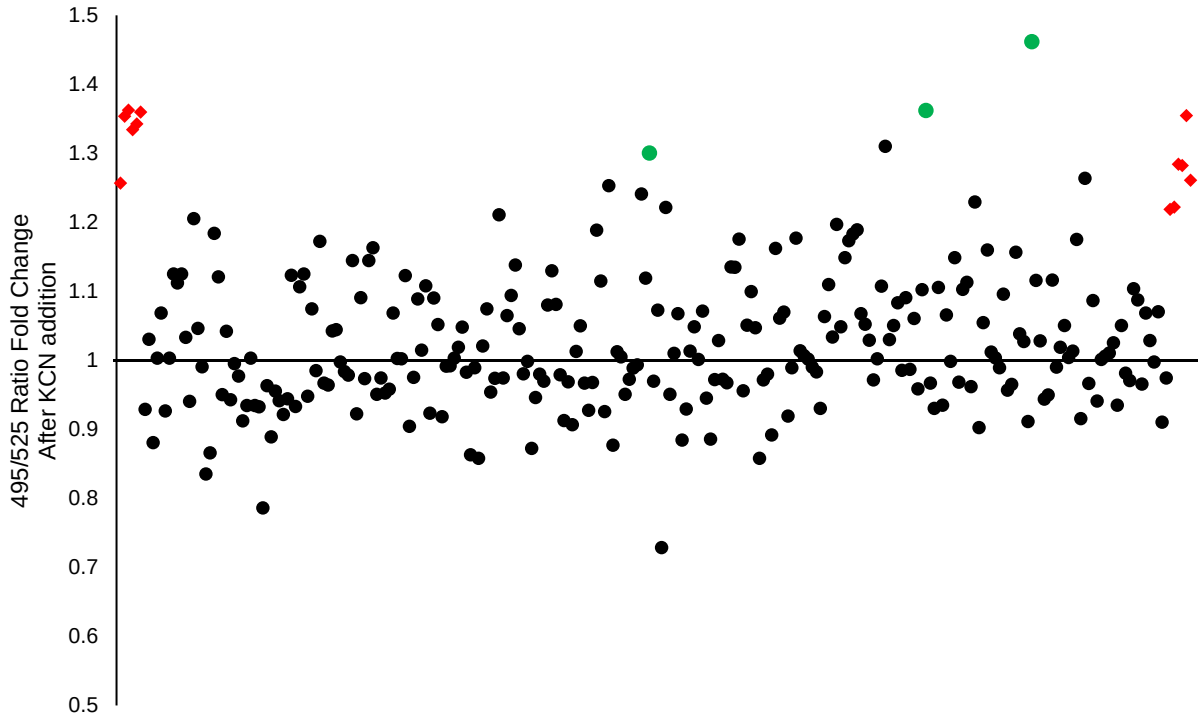

Figure 16 Results of the library screen of linker lengths: black dots indicate a single sensor candidate, green dots are sensor candidates with both emission peaks present and an improved ratiometric change after KCN addition, red diamonds are the positive control, ATeam1.03 an ATP sensor

After the linker library screen the sensor had an improved dynamic range, however we wanted to attempt to improve the FRET change even more so. Therefore, we planned another library using poly proline linkers in between the FPs and ParM. Poly proline linkers have been used before to try and optimize the FRET change of a fluorescent biosensor for calcium[25]. The poly proline linkers should be relatively ridged because of the structure of the amino acid proline. This rigidity should cause a greater change in the distance between the two FPs upon ParM binding to its substrate, ADP. The library was designed to screen poly proline linkers with zero to seven prolines in between the ParM and the two FPs. At this point we had also become concerned that the native affinity of ParM for ATP may be interfering with our library screens inside of live bacteria because of the vast amounts of ATP present. To solve this problem, we shifted to a plate-based nickel affinity chromatography purification system to purify our libraries and then tested the purified protein's response to added ADP. Using the new screening method, we screened the poly-proline library using $mTFP1_{wt}$ and $cpmVenus_{157}$ as our FRET pairs (Figure 17).

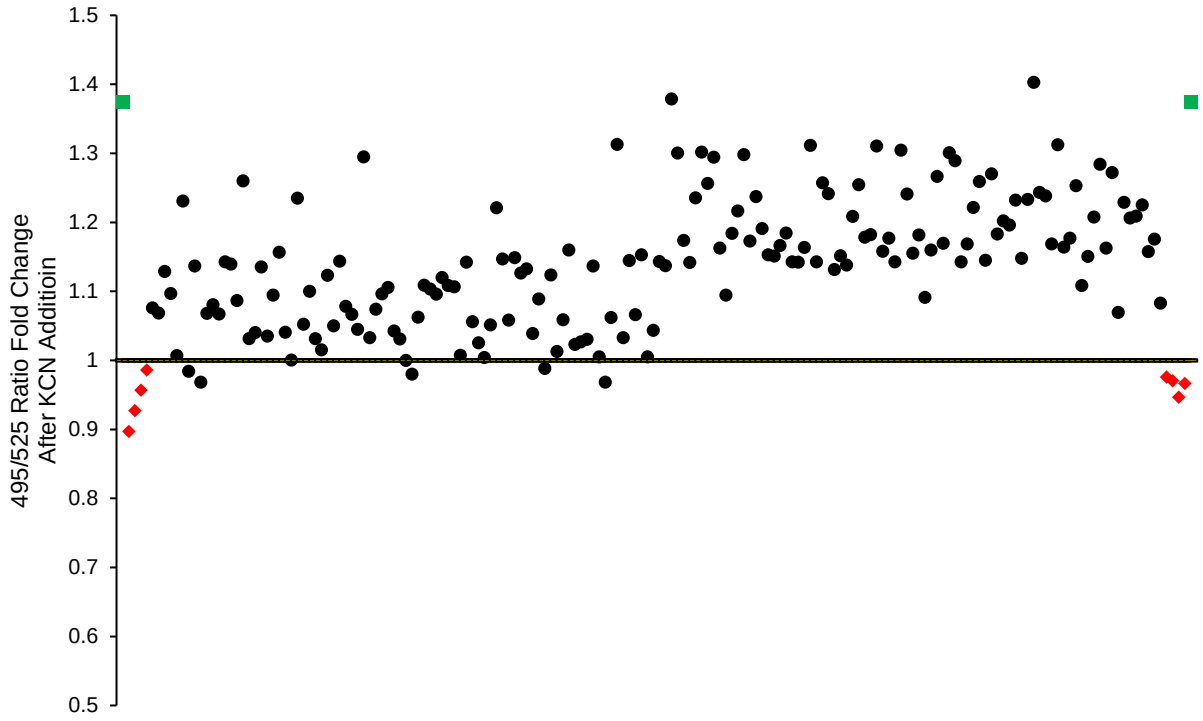

Figure 17 Results from the poly proline library. Black dots indicate a single sensor candidate, green squares are average response of the highest responders from the previous library ($mTFP_{wt}$-SGITS-ParM-AAA-$cpmVenus_{157}$), red diamonds are the positive control, ATeam1.03 an ATP sensor.

Though many of the candidates had a similar dynamic range when compared to the candidates from the previous screen, the improvement was not as great as we expected. Comparing these responses to the response we saw in the previous library, only two candidates matched or exceeded the dynamic range (Figure 17). Therefore, we decided to continue working with the sensor we identified from the first two rounds of screenings, $mTFP_{wt}$-SGITS-ParM-AAA-$cpmVenus_{157}$.

To ensure that our sensor candidate was an actual FRET sensor that had a reversable ratiometric FRET change in response to changing ADP concentration we measured the lifetime change of the donor FP using a similar assay as the one used to identify the sensor. In this assay, our sensor was expressed in *E. coli* suspended in a low glucose media. After measuring a baseline for the donor lifetime, glucose was added. This should cause an increase in cellular ATP and a corresponding decrease in ADP which would correspond to an increase in the FRET between the two FPs and thus a decrease in the donor lifetime (Figure 18). Then cyanide was

added, which should inhibit production of ATP, so as the cell uses up the available ATP we should see an increase in the cellular concentrations of ADP, a decrease in FRET, and an increase in the donor lifetime, which is what we observe (Figure 18).

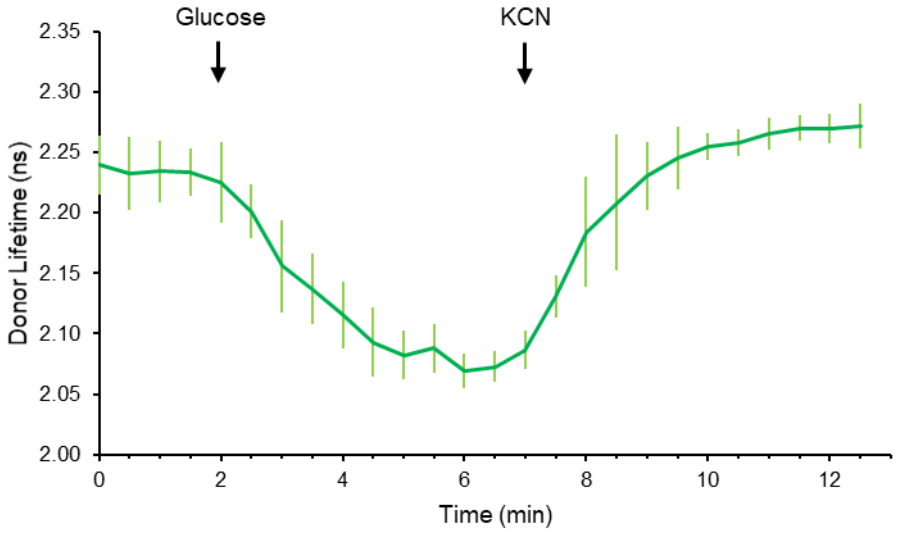

Figure 18 Lifetime measurements of *E. coli* cells expressing $mTFP_{wt}$-SGITS-ParM-AAA-$cpmVenus_{157}$ in low glucose media. At 2 min glucose was added and at 7 min cyanide was added. Average ± CI95

From here we decided to work with the $mTFP_{wt}$-SGITS-ParM-AAA-$cpmVenus_{157}$ sensor which we have named ADPrime (ADP sensor for Ratiometric IMaging of Extracellular purines) and fully characterize its sensing capabilities.

4.4 *In vitro* Characterization

To determine the sensing capability of the sensor, we performed a full dose response and determined that the affinity to ADP of ADPrime is 0.16±0.06 µM (mean ± stdev n=9) (Figure 19), which is increased from the previously reported K_d of 0.51µM[58], improving the sensitivity for the sensor for use in the extracellular space (nM-µM range)[57,109,110]. Though there is a loss in dynamic range of ADPrime[58,59], we believe that it is enough of a change to be seen in cells.

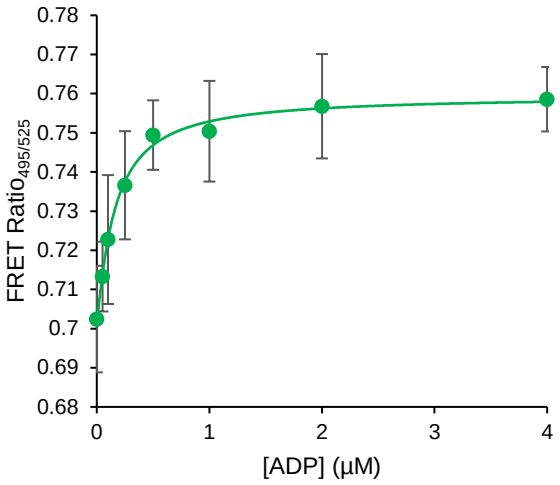

Figure 19 ADP dose response. K_d = 0.16±0.06 µM (n=9 mean ± stdev) Each point is an average, errors bars represent standard deviation, curve is derived from the fitting.

ParM is known to also have an affinity to ATP, though lower than its affinity for ADP, it could pose a potential problem when using our sensor to measure extracellular purinergic signaling. The Kd of ADPrime for ATP in protein solution is 9.88 ± 6.34 µM (mean ± stdev n=9). Though ADPrime's affinity for ATP is higher than the previously reported sensor[58,59], it is still almost 100x lower than its affinity for ADP hopefully relaying specificity for ADP over ATP.

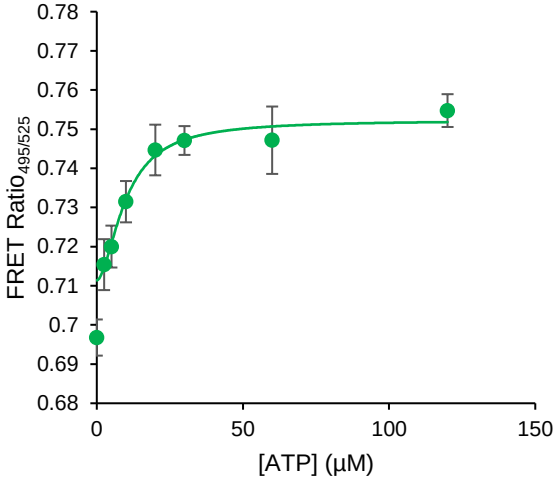

Figure 20 ATP dose response. K_d =9.88 ± 6.34 µM (n=9 mean ± stdev)

We then wanted to test ADPrime's specificity for ADP over ATP and ensure that our sensor could still detect ADP in the presence of ATP. In order to test this an ADP dose response was performed in the presence of ATP, at concentrations close to the K_d and at saturating levels. In the presence of 10µM ATP, ADPrime was still able to detect ADP with similar affinity, though the dynamic range of the sensor was diminished (Figure 21a). However, in the presence of saturating concentrations of ATP, 50µM, ADPrime lost all ability to detect changes in ADP concentration (Figure 21b). We suspect that the partial and complete loss of FRET response is due to a competitive binding event. For the purpose of a sensor that would sit on the extracellular membrane of cells, these ATP concentrations would not be prohibitive[49,107].

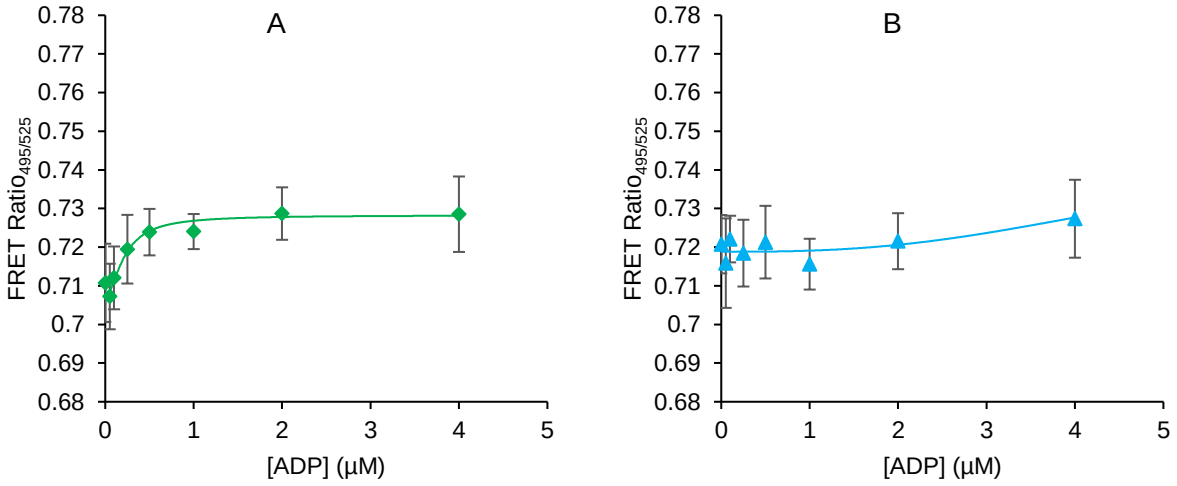

Figure 21 ATP competition assays in the presence of a) 10µM ATP (K_d – 0.22 ± 0.095µM (n=9 mean ± stdev)) and b) 50µM ATP (K_d – 5.30 ± 125.71µM (n=9 mean ± stdev))

Adenosine is the final degradation product of ATP and ADP and also can be involved in purinergic signaling; thus, it is a possible species that would be present at the extracellular space. Therefore, we wanted to ensure ADPrime had no affinity for adenosine. Upon testing, ADPrime showed no affinity for adenosine (Figure 22a). Though it was highly unlikely that adenosine would have the same competitive binding affect that ATP had, ran similar tests to ensure that we did not see the same effect as ATP. Adenosine had no effect on ADPrime's affinity for ADP or it's dynamic range (Figure 22b).

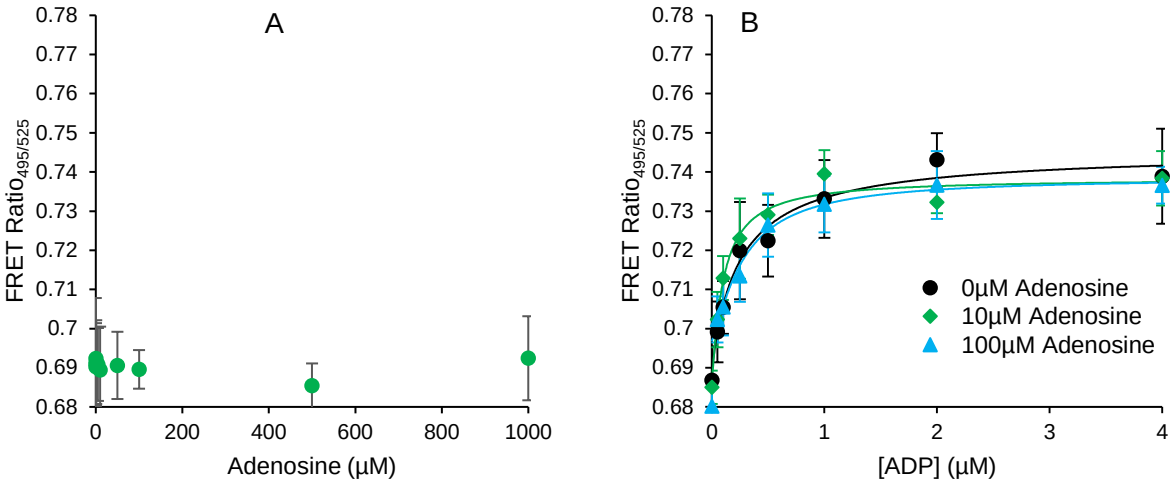

Figure 22 a) Adenosine dose response (n=9 mean ± stdev) b) adenosine competition assay (n=9 mean ± stdev)

Most fluorescent proteins are sensitive to changing pH because the chromophore must be in the deprotonated state to fluoresce. In light of this, the sensitivity to changing pH and its effect on ADP response was also tested for our sensor. As expected, ADPrime is sensitive to pH and its pKa is similar to the pKa of wild type mVenus (pKa=6.0)[113] (Figure 23). Therefore, ADPrime's pH sensitivity is most likely due to the pH sensitivity of the Venus and not due to a pH-dependent nucleotide binding effect. mTFP1 likely does not contribute to this pH sensitivity because it's reported pKa (4.3)[114] is well outside of the range tested here. We also noted that the pH curve shifts upwards upon addition of saturating levels of ADP, which is expected due to the sensor's response to ADP. To further demonstrate that the pH effect we observed is due to sensitivity in the Venus and not a pH-sensitive nucleotide binding effect we tested how pH affects ADPrime's ability to detect ADP changes in a dose dependent manner (Figure 24).

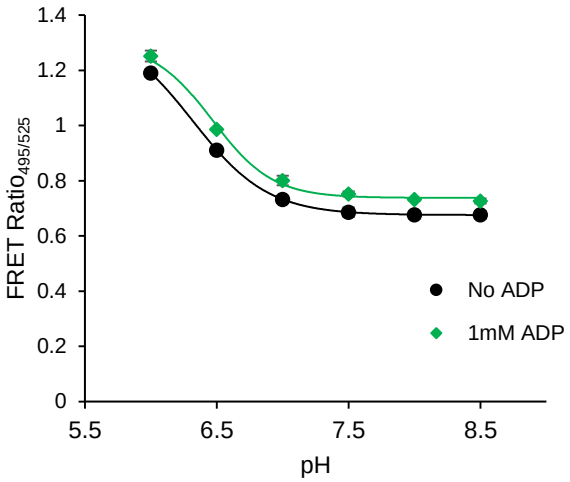

Figure 23 pH sensitivity curve in the presence (pKa – 6.3±0.002 (n=3 mean ± stdev)) and absence (pKa – 6.5±0.04 (n=3 mean ± stdev)) of saturating levels of ADP

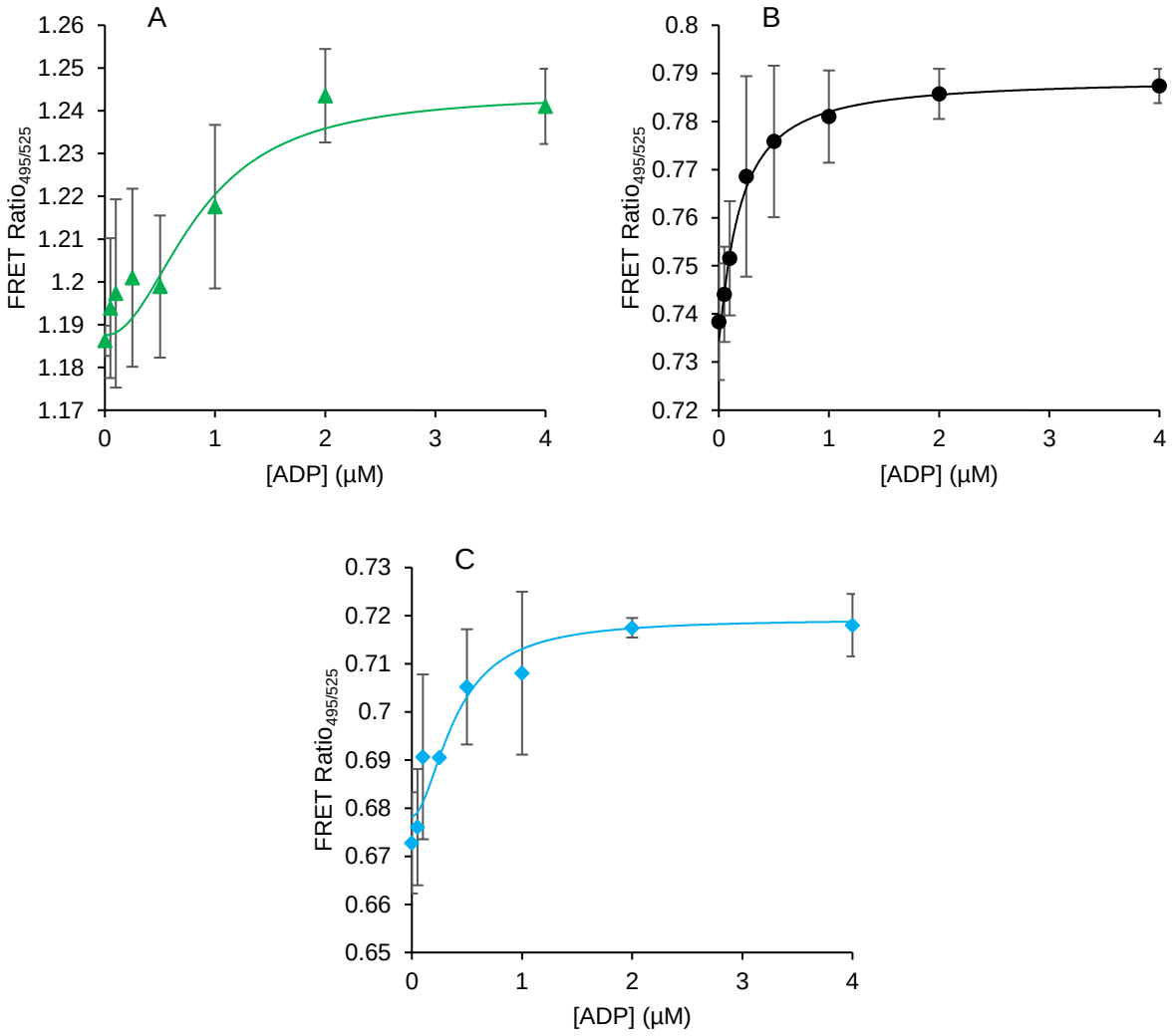

Figure 24 ADP dose responses at various pH A) performed at a pH of 6, K_d – 0.85±0.29µM (n=3 mean ± stdev) B) performed at a pH of 7, K_d – 0.18±0.07µM (n=3 mean ± stdev) C) performed at a pH of 8, K_d – 0.40±0.10µM (n=3 mean ± stdev)

At different pH's ADPrime can still detect changes in ADP concentration with only a slight shift in K_d and little to no change in dynamic range. The overall ratios changes when at a more acidic pH due to the affect pH had on the mVenus chromophore.

4.5 Live Cell Experiments Measuring Extracellular ADP

Using the membrane tag from the platelet derived growth factor receptor, ADPrime was targeted successfully to the extracellular side of the plasma membrane of adherent HEK-293 cells

(Figure 25). Both the mTFP and the mVenus are clearly visible at the membrane (Figure 25B & C), fluorescence seen inside of the cell is likely also membrane because widefield microscopy was used. The same type of ratio change was observed on the cell membrane as was seen in solution in the presence of ADP (Figure 25 D, E).

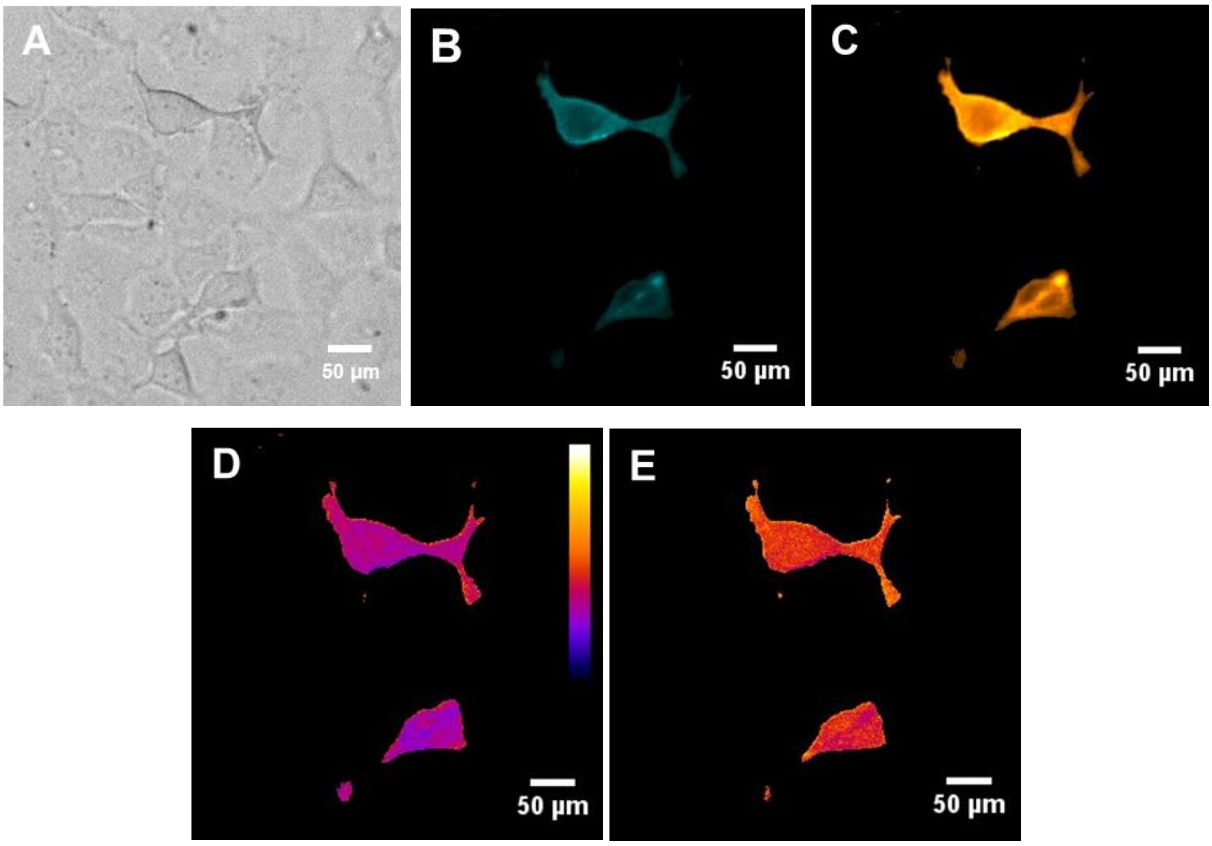

Figure 25 HEK-293a cells expressing ADPrime on the extracellular membrane A) DIC image B) Fluorescent image of the mTFP1, clearly targeted to the membrane C) Fluorescent image of the mVenus, clearly targeted to the membrane D) Ratio image (495/525) at the beginning of the imaging experiment in the presence of no ADP E) Ratio image (495/525) during the experiment in the presence of 1mM ADP

ADP was perfused across cells expressing ADPrime at 100uM and 1mM and then the ADP was washed out. The sensor was easily able to detect these changes in ADP concentration and returned to a baseline after they were washed out. It is unclear why the sensitivity of ADPrime seems to be diminished on the membrane. The change in sensitivity is a phenomenon that has been seen before, where sensors have different sensitivity when expressed on the membrane versus in

protein solution. This maybe just a difference in the bath concentration versus the at membrane concentration.

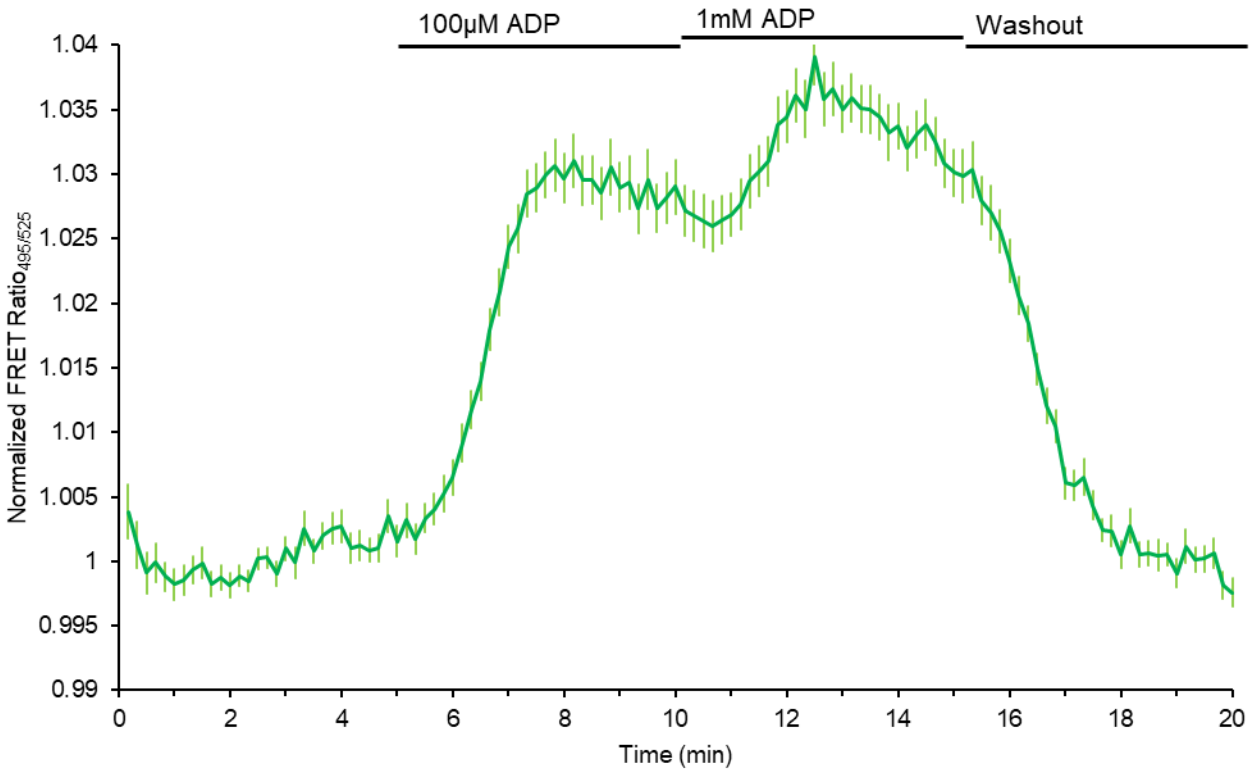

Figure 26 ADP calibration in live cells on the extracellular membrane. Baseline measurement for 5 minutes, calibrations with 100µM ADP for 5 minutes, calibration with 1mM ADP for 5 minutes, final washout for 5 minutes. (n=77 mean ± 95% confidence interval)

To further demonstrate the usefulness of ADPrime, we used a well-established model where a change in osmotic pressure induces a release of purinergic signaling molecules[109]. In order to validate the release of purines, these experiments were done with cells expressing an ATP sensor, ATeam, in the same well[49]. In these experiments a robust response to the osmotic shock was seen with both ADPrime and the ATeam sensor (Figure 27). These experiments were calibrated by the addition of ADP and ATP at the end of the experiment. This demonstrates the ability of ADPrime to detect physiological changes in purinergic signaling molecules.

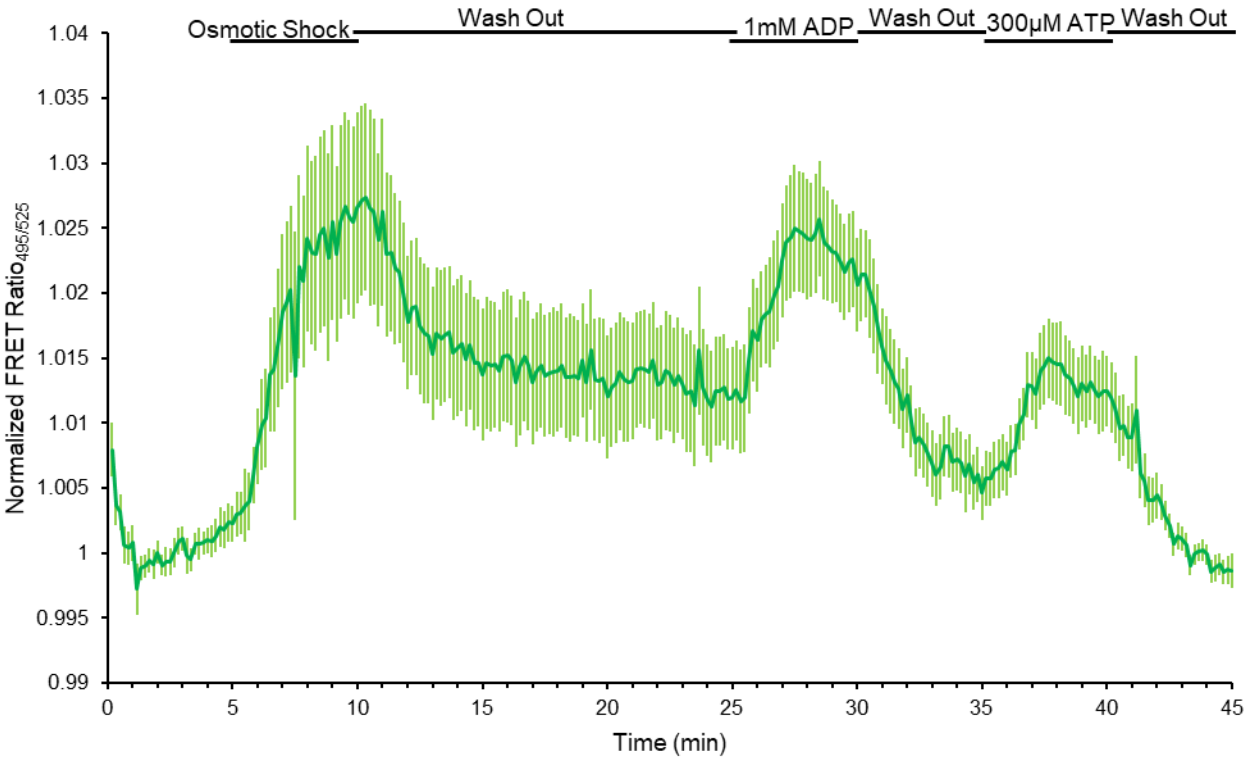

Figure 27 Osmotic shock experiments with sensor on extracellular side of the plasma membrane in HEK293a cell. Baseline measurement for 5 min, osmotic shock for 5 min, recovery for 15 mins, calibration with 1mM ADP for 5 mins, washout for 5 mins, calibration with 300µM ATP for 5 mins, final washout for 5 mins. (n=62 mean ± 95% confidence interval)

4.6 Conclusions

We have demonstrated that ADPrime is sensitive to ADP and can be used to detect ADP on the extracellular membrane of cells. Further steps will need to be taken to decrease ADPrime's affinity for ATP if it is to be used in any model systems. It would also be of use to continue attempts to optimize the sensor and increase its dynamic range beyond the small change see in this first generation. Looking more closely into the insert type sensors that we attempted to use in our first round of screenings may be one way to achieve this goal. One could also attempt to improve many of the candidates that were identified with the polyproline library. Directed evolution would be a viable approach to both decrease ATP affinity while increasing dynamic range. Another approach that may help increase the dynamic range would be exchanging the two fluorescent proteins with other FPs that have been shown to have high FRET efficiencies or greater brightness.

Overall, ADPrime was a successful attempt at generating a fully genetically encoded biosensor capable of detecting extracellular ADP. ADPrime serves a good first-generation sensor that may be improved upon for the creation of future generations of ADP sensors.

4.7 Methods

FP Library Cloning

The ParM gene was made as a G-block to include mutations previously shown to increase ADP affinity over ATP[58,59]. The library of mTFP1-mVenus constructs (Pertz kit) was purchased from AddGene[112]. Cloning for the first library we done using a double restriction enzyme digest using NotI and BspEI to insert ParM between the pair of FPs (mTFP on ParM's N-terminal end and mVenus on the C-terminal end). The restriction sites were present in the Pertz kit DNA and were added to ParM via PCR[112]. The library was grown in a deep-well, 96-well plate with a blank, pUC, and ATeam control. The library was expressed in DH5a cells in LB media for 14-18 hours at 37^{o}C then 2 days at room temperature.

KCN Assay

Bacterial cultures were diluted in M9 media (50mM Na_2HPO_4, 20mM KH_2PO_4, 20mM NH_4Cl, 9mM NaCl, 2mM $MgSO_4$, 0.1mM $CaCl_2$, pH 7.5) to and OD600 of 0.2. Fluorescent emission spectra were then measured, excitation wavelength 450/9nm, emission wavelengths 470-600/9nm. KCN was then added to a final concentration of 10mM, the cultures were incubated with the cyanide for 10 minutes before a second set of emission spectra were measured.

Constructs that contained peaks for both fluorescent proteins and significant ratiometric changes were selected for the second library.

Linker Library Cloning

A library was designed to shorten the linker length between the FPs and the termini of ParM to seven, five, or three amino acids. This library was screened with the same assay as described above.

Poly-proline Library

Primers were designed to insert poly proline linkers of 0-7 repeats of the amino acid proline in between ParM and both the mTFP1 and mVenus (a total of 16 primers and a library size of 64). This library was expressed the same way as before but after expression the culture was lysed using a lysozyme-freeze thaw method. In short, cells were resuspended in lysis buffer (MOPS buffer,

100mM MOPS, 50mM KCl, 5mM NaCl, 0.5mM $MgCl_2$, pH 7.3 + 1mg/mL lysozyme, 0.1% Triton-X, 1mM PMSF, 1mM DTT), incubated at 37°C for 30 minutes then cycled between freezing (-80°C) and thawing (37°C) three times. Lysate was pelleted at 2,500xg for 15 minutes. Lysate was then transferred to a HC 96-well plate (Sigma S5563) and incubated at room temp. for at least 4 hours then at 4°C for at least 12 hours. Remaining lysate was then aspirated and the plate was rinsed 3x with TBS-Tween (TRIS buffered saline 0.05M Tris, 0.138M NaCl, 0.0027M KCl, 0.05% Tween-20, pH 8), then rinsed 3x with MOPs buffer (100mM MOPS, 50mM KCl, 5mM NaCl, 0.5mM $MgCl_2$, pH 7.3). Protein was eluted with MOPS buffer + 20mM Imidazole and 0.1% BSA on a shaker for 1-2 hrs. Eluate was then added to a pre-treated (incubated with elution buffer during purification) low-binding 96-well plate. ADP was then added incrementally with an emission spectrum taken at each step (0µM, 0.05µM, 0.25µM, 1µM, and 5µM ADP)

Protein Expression

The three hits from the second round of screens were expressed at a larger scale (250mL) and purified using nickel affinity chromatography on an AKTA instrument.

Dose Response Assays

All dose response assays were performed at a protein concentration of 0.125µM in buffer previously used for purinergic dose response assays (50mM MOPS-KOH, 50mM KCl, 0.5mM $MgCl_2$, 0.05% Triton-X, pH 7.3)[24,49]. ADP was complexed with Mg^{2+}

Competition Assays

Competition assays were run as ADP dose response assays in increasing amounts of the purine of interest. ATP was complexed with Mg^{2+} .

pH Assay

To test for pH sensitivity the FRET ratio was measured with and without saturating ADP in buffers of varying pH (0.5 pH unit increments)

Transfection/Membrane Expression

Membrane targeting was achieved by cloning our ADP sensor construct into a plasmid that contained the Igκ signal sequence and the PDGFR membrane tag. The plasmid was transfected into HEK-293a cells via a calcium phosphate transfection (20K cells/cm^2, 3.6ug/well in 6well plate).

Microscopy

Cells were imaged in an imaging solution (120mM NaCl, 15mM HEPES, 10mM Glucose, 3mM KCl, 3mM $NaHCO_3$, 2mM $CaCl_2$, 1.25mM NaH_2PO_4, 1mM $MgCl_2$, pH 7.3) on a 3.8mm nitric acid treated glass cover slip in a Warner perfusion chamber. Cells were perfused with imaging solution (~2mL/min) for at least 15 minutes prior to imaging. Live cell imaged were taken using an Olympus IX83 Microscope in 10 second intervals taking a CFP (x438,m470), CYFRET (x438,m540), and YFP (x510,m540) image each interval for the entirety of the experiment. During imaging solutions (imaging solution, osmotic shock solution, ADP calibration solution, ATP calibration solution) were perfused at approximately 2mL/minute for the entire experiment.

Image Analysis

Analysis of Imaging data was carried out using ImageJ. Five ROIs were drawn to obtain an average background for each experiment. The background was manually subtracted, and a mask was made using a minimum threshold of the mean background plus three times the standard deviation. Cellular membrane ROIs were selected by hand, the mean gray value was measured for each channel. A ratio image of the CFP/CYFRET images was made to measure the overall FRET change. The mean grey value was collected from each image and the ratio data was normalized to remove the baseline drift.

CHAPTER 5. IMAGING CELLULAR REDOX DYNAMICS

Reproduced with permission from ACS Sens.2017,21,11 721-1729
Publication Date: October 26, 2017

5.1 Intro

Reduction-oxidation (redox) reactions must be kept in a careful balance in order to maintain healthy cell growth and function[60–62]. Loss of redox balance can lead to both reductive and oxidative stresses associated with aging, cancer, cardiovascular disease, and Parkinson's disease[63–66]. For example, reactive oxygen species (ROS), such as hydrogen peroxide (H_2O_2) and superoxide anion ($O_2^{\bullet -}$), can oxidize protein-bound cysteines and other molecular species during normal metabolism and signaling[67]. However, excess ROS can cause oxidative stress and damage that leads to loss of function or cell death. To prevent such pathologies, redox enzymes and cellular redox buffers such as glutathione (GSH) are critical for maintaining proper redox balance. Together, both enzymatic and non-enzymatic components make up a "redox network"[60] that contributes to homeostasis in the face of changing intracellular and environmental conditions faced by prokaryotes and eukaryotes.

Like metabolic and signaling networks, the redox network is spatially organized within a cell, and compartments such as the cytosol and mitochondria contain distinct sources of ROS as well as distinct antioxidant mechanisms involving redox enzymes and redox buffers[60]. As a result, compartment-specific redox and ROS dynamics exist with varying degrees of cross-compartment coupling[68–71]. Redox coupling across compartments is a critical aspect of network response. For example, the production of mitochondrially-derived cytosolic ROS plays an integral role in retrograde mitonuclear communication and stress response[72,73]. However, compartment-specific ROS dynamics and redox signaling between organelles has been poorly studied because of the lack of spectrally-compatible redox probes that are available to simultaneously quantify redox in multiple compartments within the same living cell.

Currently, the redox-sensitive green fluorescent protein (roGFP) sensors are widely used to study redox biology across model species, including yeast, plants, and animals[15,78,115–119]. The roGFP sensors were originally developed by engineering two solvent-facing cysteines on the β-barrel of GFP[15]. Upon oxidation, the cysteines form a disulfide bond, causing a structural change

that alters the protonation state of the internal chromophore. Redox state is reported as the ratio of the two peaks in the fluorescence excitation spectrum near 400 nm and 485 nm, in which oxidation causes an increase in the 400 nm peak and a decrease in the 485 nm peak. There are two versions of the sensor: the roGFP1 sensor is based on wildtype GFP in which the 400 nm peak is greater in absolute magnitude, and the roGFP2 sensor is based on GFP(S65T) in which the 485 nm peak is greater in absolute magnitude. The roGFP sensors are particularly useful because they can be genetically targeted to specific cell types and subcellular locations, including the cytosol and mitochondria. Furthermore, they provide ratiometric readouts that are independent of expression level and enable quantitative measurements that can be compared between independent experiments.

However, the roGFP-based sensors are solely green fluorescent, which makes accurate measurement of redox dynamics in multiple compartments within the same cell difficult or impossible. Recently, red fluorescent redox sensors, HyPerRed[75] and rxRFP[76], were engineered and can be used for dual-compartment, dual-color live-cell microscopye[76], but these sensors are not ratiometric, which can render quantitative analysis more challenging.

Therefore, in this work we describe the design, development, characterization, and validation of a first-generation family of roGFP-based sensors that exhibit long-wavelength emission via Förster-type resonance energy transfer (FRET) from a roGFP donor to a red fluorescent protein (RFP) acceptor. Importantly, we show that the redox properties of the parent roGFP donor are maintained when measuring the red emission of the roGFP-RFP sensors. We also report proof-of-principle studies that demonstrate that using multicolor imaging we can measure redox dynamics in the cytosol and mitochondria simultaneously within the same cell.

5.2 Design for Extending roGFP Emission

This sensor design employs a FRET “relay” strategy in which the roGFP serves as a redox-sensing donor that is fused to a RFP acceptor (Figure 28).[100,120–122] Excitation of the roGFP at any wavelength in its excitation spectrum will result in red fluorescence from the RFP while preserving both redox sensing properties and a ratiometric readout. In principle, the roGFP-RFP red emission will be spectrally distinct and enable dual color imaging by co-expressing both roGFP and roGFP-RFP in the same cell. This FRET relay strategy has been demonstrated with both CFP-YFP as well as GFP-RFP fusions engineered for high efficiency FRET, and this relay strategy has been used to

overcome autofluorescence in live-cell imaging.[100,120–122] It is important to note that FRET between the roGFP donor and RFP acceptor is designed to be constant in this strategy, and the ratiometric redox sensing originates solely from the change in the roGFP excitation spectrum. Thus, our design is fundamentally different from sensors that report redox changes by a change in FRET.[123,124]

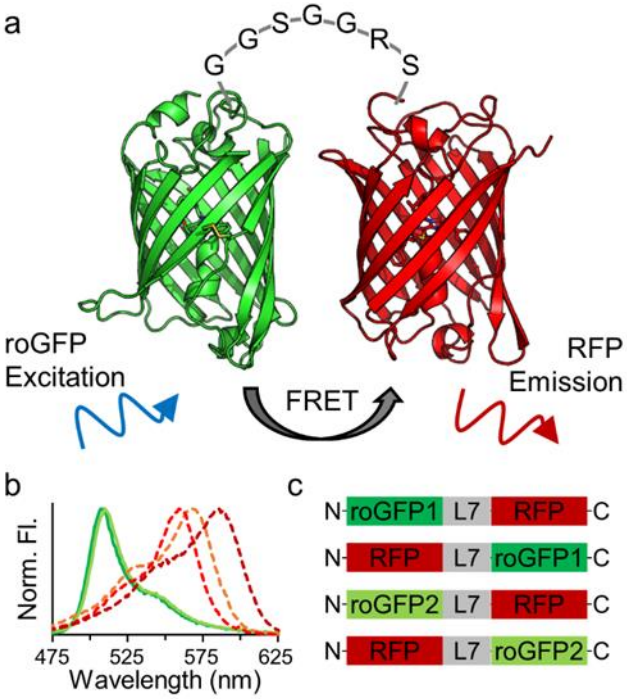

Figure 28 Design of the roGFP-RFP sensor library. (a) Diagram of the FRET relay from the roGFP donor to the RFP acceptor. (b) Fluorescence spectra showing roGFP (solid, green) emission and RFP excitation (dashed, left-to-right: mRuby2, mApple, mCherry). (c) Diagram of the N- versus C-terminal fusions tested in this work, in which L7 indicates the GGSGGRS linker.

To implement our design, we first generated a library of twelve roGFP-RFP fusions to identify constructs that provide red emission via our FRET relay strategy. FRET efficiency depends on the distance, orientation, and spectral overlap between the donor and acceptor fluorescent proteins.[125] Therefore, we considered four main variables in our library design: the roGFP choice, the fusion linker, the RFP choice, and the orientation of the fusion. We included both roGFP1 and roGFP2 as possible donors in our library because they have similar redox sensing capabilities and provide ratiometric readouts[15]. Although the roGFP2 sensor is more commonly used, the roGFP1 sensor can be beneficial for live-cell imaging because of its greater brightness

when excited at 400 nm. For the fusion linker, we used a short seven amino acid linker (GGSGGRS) that has previously been used for high efficiency FRET between fluorescent proteins.[126] For the acceptor, we included the RFPs mRuby2, mApple, and mCherry (Figure 28).[99,127,128] The mRuby2 acceptor provides the greatest spectral overlap between the roGFP green emission and its absorbance, and it has been used as a FRET acceptor for the GFP Clover.[127] The mCherry acceptor provides the greatest spectral separation between the green and red emission profiles, and it has been used in FRET pairs with GFPs both in vitro and in vivo.[129] We included mApple as an acceptor with intermediate spectral profile and high brightness.[128] Finally, we also included constructs in which the RFP acceptor was fused to either the N- or C-terminus of the roGFP donor (Figure 28).

5.3 Screening Sensor Candidates for FRET Efficiency

In order to select the best performing fusion constructs, we screened our library using steady-state and time-resolved fluorescence measurements. We first qualitatively screened our twelve constructs by measuring emission spectra and fluorescence anisotropy. We discovered that all twelve roGFP-RFP fusion constructs exhibit a clear red fluorescence FRET emission peak upon donor excitation (Figure 29, Figure 30). Although there is substantial residual donor green fluorescence, the red emission peak is distinct and well above background (Table 4). Furthermore, FRET is expected to cause depolarization of the red emission and thus a decrease in anisotropy. Indeed, all constructs also exhibit a large decrease in fluorescence anisotropy in the red emission channel upon donor excitation, despite the increase in overall protein size (Table 5). Thus, significant FRET occurs in all twelve constructs.

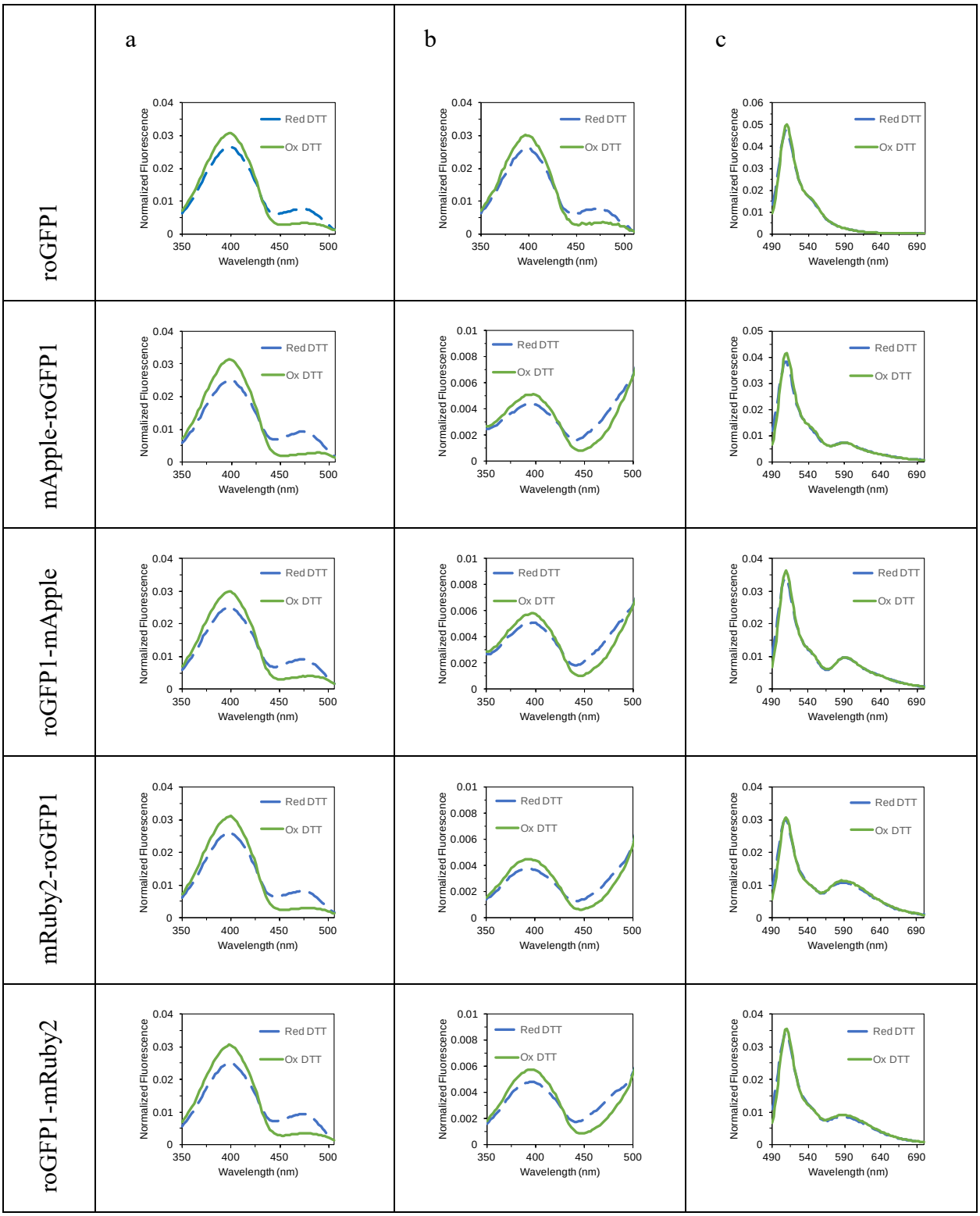

Figure 29 Fluorescence spectra of all roGFP1 sensor constructs. (a) excitation spectra collecting green donor emission, (b) excitation spectra collecting red acceptor emission and (c) emission spectra exciting at the isosbestic point.

Firgure 29 Continued

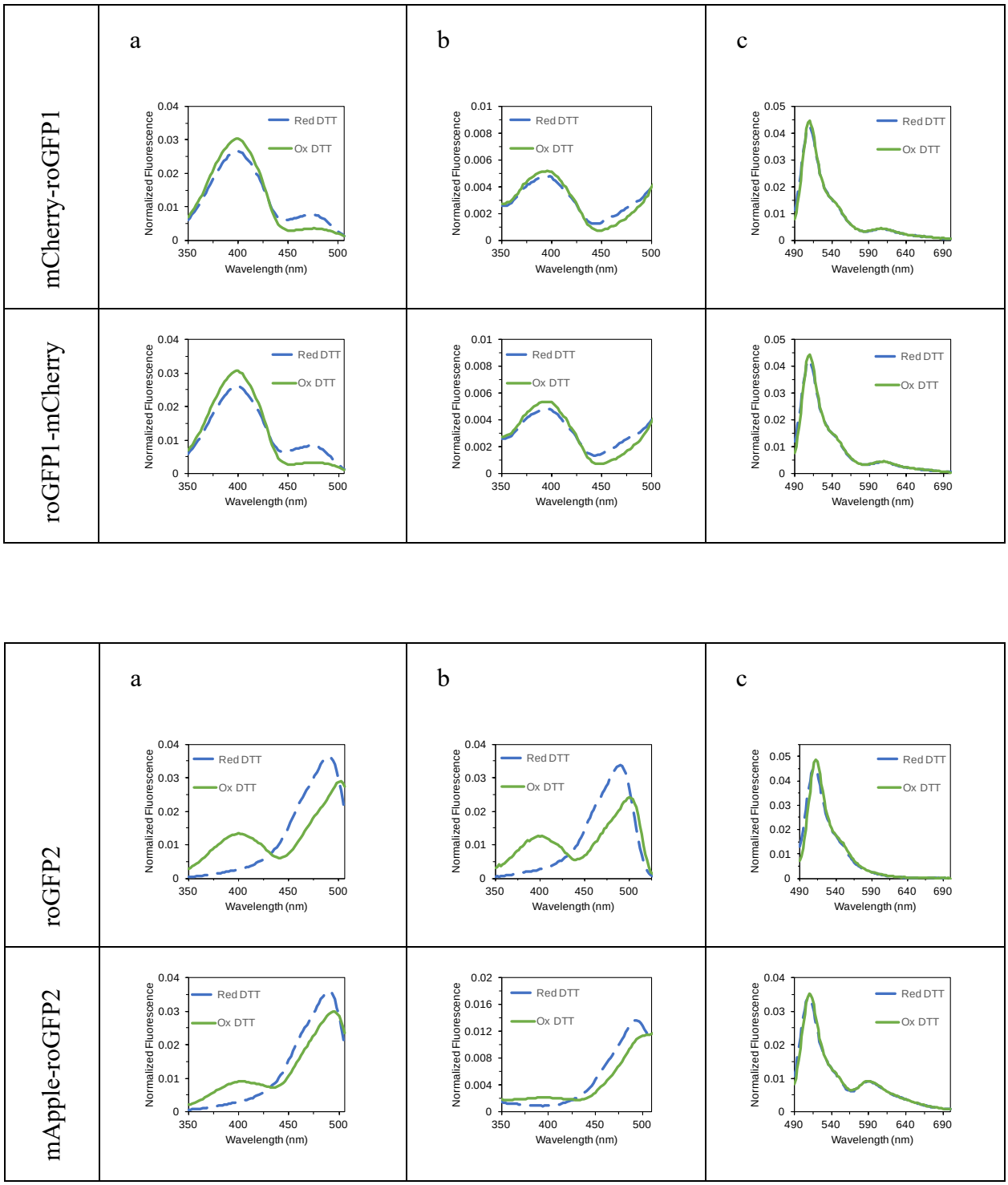

Figure 30 Fluorescence spectra of all roGFP2 sensor constructs. (a) excitation spectra collecting green donor emission, (b) excitation spectra collecting red acceptor emission and (c) emission spectra exciting at the isosbestic point.

Figure 30 Continued

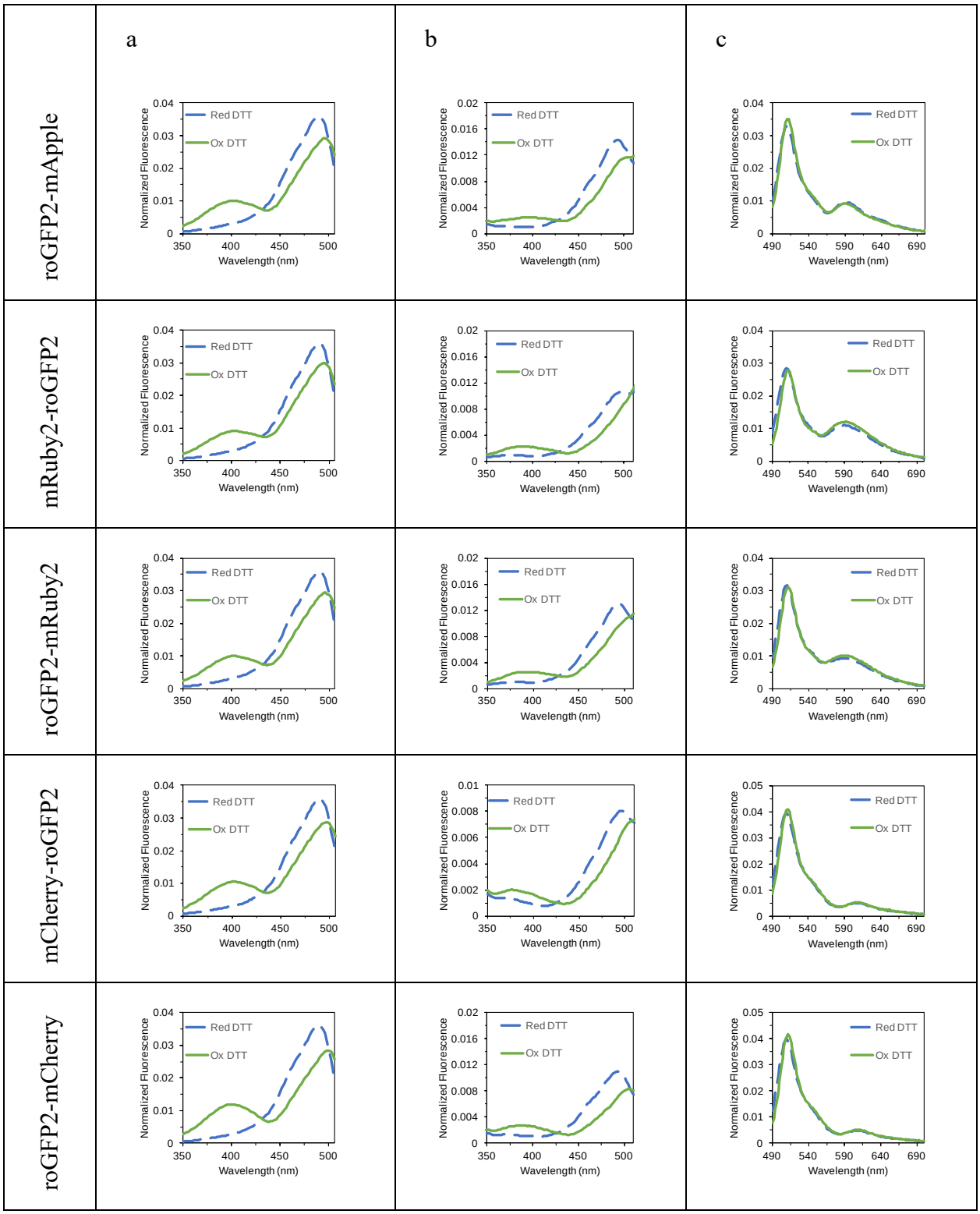

Table 4 Spectral bleed-through (mean ± stdev)

Construct	400 nm Bleed-Through (%)	480 nm Bleed-Through (%)
mApple-roGFP1, roGFP1-mApple	6.8 ± 0.1	14.3 ± 0.7
mRuby2-roGFP1, roGFP1-mRuby2	4.82 ± 0.07	10 ± 1
mCherry-roGFP1, roGFP1-mCherry	7.3 ± 0.9	7.3 ± 0.9
mApple-roGFP2, roGFP2-mApple	6.9 ± 0.1	13.1 ± 0.2
mRuby2-roGFP2, roGFP2-mRuby2	4.7 ± 0.2	9.3 ± 0.1
mCherry-roGFP2, roGFP2-mCherry	4.06 ± 0.09	6.65 ± 0.07

Table 5 Steady-state and time-resolved fluorescence characterization of roGFP-RFP library (n=3, mean ± stdev.) * Three highest FRET efficiency constructs chosen for in-depth characterization.

Construct	Anisotropy	$Ratio_{(ox)}$ / $Ratio_{(red)}$	Donor Lifetime (ps)	FRET Efficiency
roGFP1	0.270 ± 0.001	2.61 ± 0.02	3145 ± 2	N/A
mApple-L7-roGFP1	0.047 ± 0.002	1.62 ± 0.04	2370 ± 10	0.247 ± 0.006
roGFP1-L7-mApple	-0.028 ± 0.001	1.51 ± 0.02	2175 ± 5	0.308 ± 0.003 *
mRuby2-L7-roGFP1	0.107 ± 0.001	1.63 ± 0.01	2140 ± 30	0.32 ± 0.01 *
roGFP1-L7-mRuby2	0.0660 ± 0.003	1.75 ± 0.01	2360 ± 20	0.249 ± 0.007
mCherry-L7-roGFP1	0.04 ± 0.02	1.44 ± 0.03	2280 ± 1	0.275 ± 0.001
roGFP1-L7-mCherry	0.03 ± 0.02	1.63 ± 0.04	2290 ± 20	0.273 ± 0.008
roGFP2	0.270 ± 0.001	8.07 ± 0.01	2905 ± 5	N/A
mApple-L7-roGFP2	0.022 ± 0.002	3.22 ± 0.03	2085 ± 2	0.282 ± 0.002
roGFP2-L7-mApple	-0.0132 ± 0.0008	3.66 ± 0.07	2074 ± 5	0.286 ± 0.003
mRuby2-L7-roGFP2	0.126 ± 0.001	4.86 ± 0.04	2130 ± 30	0.27 ± 0.01
roGFP2-L7-mRuby2	0.0698 ± 0.007	4.15 ± 0.07	2180 ± 20	0.248 ± 0.008
mCherry-L7-roGFP2	0.053 ± 0.002	2.92 ± 0.03	1986 ± 4	0.316 ± 0.003 *
roGFP2-L7-mCherry	0.018 ± 0.002	4.456 ± 0.008	2062 ± 2	0.290 ± 0.002

We next assessed whether the constructs preserve redox sensing by measuring the steady-state fluorescence excitation spectra in the presence of excess reduced or oxidized dithiothreitol (10 mM DTT). All twelve constructs exhibit a redox-dependent ratiometric change in the excitation spectrum when collecting either direct donor roGFP green fluorescence emission or FRET acceptor red fluorescence emission (Figure 29, Figure 30). From the excitation spectra, we quantified the excitation ratios for the FRET acceptor red fluorescence emission channel (Ratio =

F400nm/F485nm) in the oxidized and reduced states, and we measured the dynamic range as the maximal fold change in ratio signal upon oxidation (Dynamic range = $Ratio_{oxidized}/Ratio_{reduced}$) (Table 5). Compared to the roGFP1 and roGFP2 parent sensors, the roGFP-RFP fusion constructs exhibit on average a 40% and 50% reduction in dynamic ranges. The attenuation in the dynamic ranges is primarily due to imperfect FRET efficiency, and it is not caused by spectral crosstalk between the donor and acceptor channels, which is minimal (Table 4). Despite the attenuation in dynamic range, all constructs exhibit clear preservation of redox sensing as well as a ratiometric response of the same magnitude as other sensors that have proven useful in live-cell imaging.[78,118,127]

In order to quantitatively compare FRET efficiencies of the twelve constructs, we measured donor fluorescence lifetimes, which decrease with increasing FRET efficiency. As expected, all roGFP-RFP constructs exhibit reduced donor fluorescence lifetimes relative to the roGFP1 and roGFP2 parent sensors, indicating FRET efficiencies from 25-32% (Table 5). We therefore selected three constructs with the highest FRET efficiencies, roGFP1-mApple, mRuby2-roGFP1, and mCherry-roGFP2, for further characterization of their redox sensing properties (Figure 31).

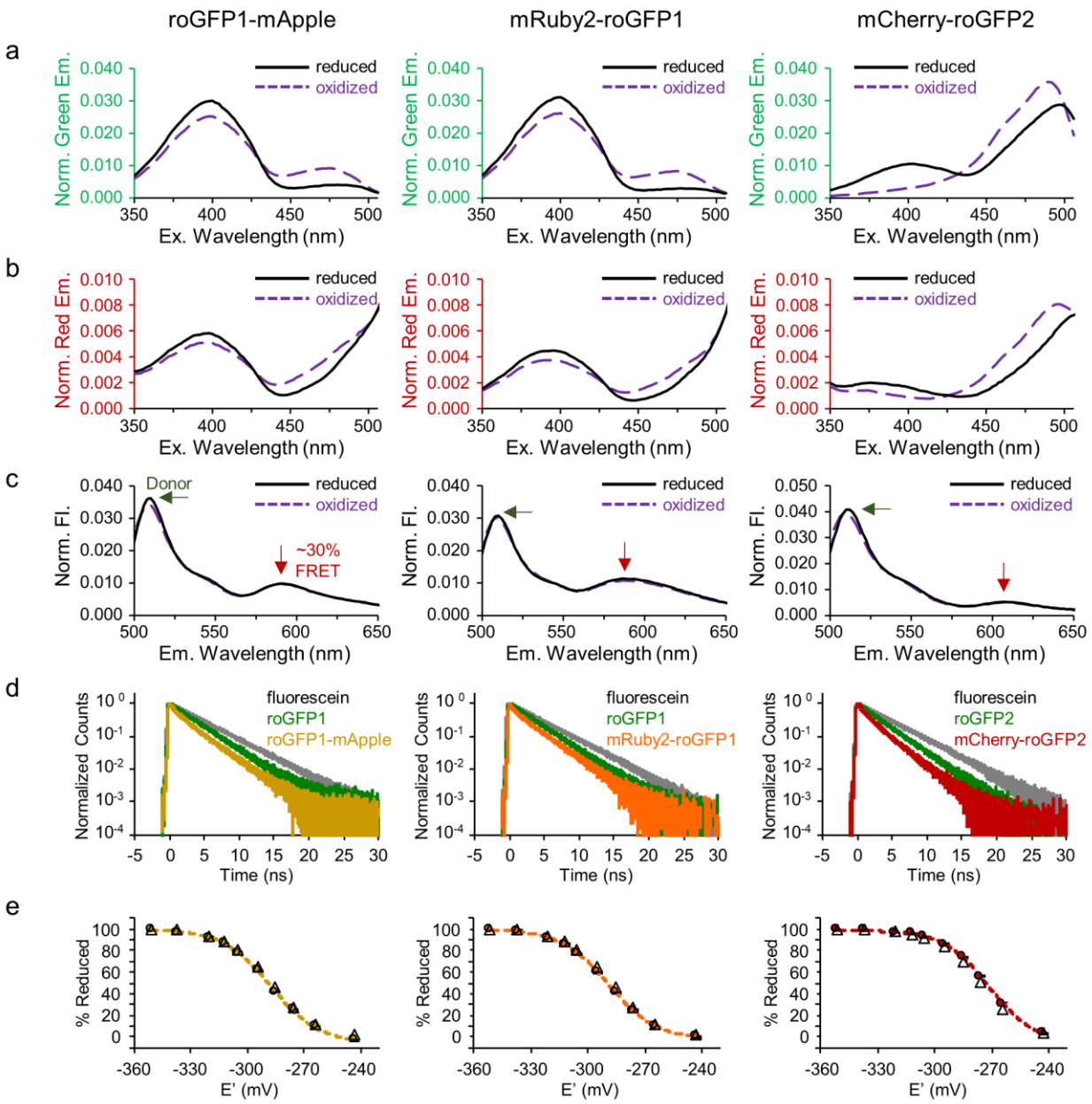

Figure 31 Characterization of steady-state and time-resolved fluorescence properties of the highest FRET efficiency roGFP-RFP constructs. (a-b) Redox-dependent ratiometric changes in the fluorescence excitation spectra when collecting (a) residual roGFP donor green emission and (b) RFP emission via FRET. (c) Fluorescence emission spectra show the residual roGFP donor (green arrow) and RFP FRET acceptor emission peaks (red arrow). (d) The roGFP-RFP constructs exhibit a decreased donor fluorescence lifetime, which is used to quantify FRET efficiency. (e) The roGFP-RFP constructs (circles, measured; dashed line, fitted) preserve redox sensing and exhibit similar DTT reduction potentials relative to the parent roGFP (triangles, measured).

5.4 *In Vitro* Characterization of Redox Potentials

To determine if the redox properties of the parent roGFP are preserved in these three selected fusion constructs, we carried out redox titrations against increasing ratios of oxidized-to-reduced DTT. We determined that the midpoint potentials of roGFP1-mApple (-287.1 ± 0.4 mV) and mRuby2-roGFP1 (-288.7 ± 0.8 mV), measured in both direct donor green fluorescence and FRET acceptor red fluorescence channels, are in agreement with the midpoint potential of the parent roGFP1 measured in this work (-287.4 ± 0.7 mV) and as originally reported by Hanson et al. using the same method (-288 mV).[15,115] Likewise, we also determined that the midpoint potential of mCherry-roGFP2 (-272 ± 1 mV) is in agreement with the midpoint potential of the parent roGFP2 measured in this work (-274.4 ± 0.5 mV) and as originally reported (-272 mV).[15,115] Thus, our results confirm that our FRET relay constructs preserve the original redox properties of the parent roGFP and provide an excitation ratiometric response when measuring the FRET acceptor red fluorescence emission. (n=3, mean ± stdev)

With ~30% FRET efficiency, the roGFP-RFP constructs generate significant red fluorescence signal, despite the residual green donor emission. By targeting these new sensors to subcellular locations, we hypothesized that the roGFP-RFP red fluorescence signal could be spectrally and spatially separated from roGFP green fluorescence signal targeted to a different compartment. Thus, in order to validate the function of the roGFP1-mApple, mRuby2-roGFP1, and mCherry-roGFP2 constructs for dual-color imaging, we next measured mitochondrial and cytosolic redox potentials simultaneously within the same cells.

5.5 Cytosolic and Mitochondrial Redox Potential

When Neuro2A mouse neuroblastoma cells were co-transfected pairwise with a mitochondrially-targeted roGFP-RFP fusion and its respective parent roGFP for cytosolic expression, we found that the red and green fluorescence signals were spectrally and spatially separated as hypothesized. The mito-roGFP-RFP fusions were targeted to the mitochondrial matrix by appending the signal sequence from cytochrome c oxidase subunit VIII (Cox8), which we and others have previously employed, and we observed excellent subcellular localization to mitochondria, as expected (Figure 32)[129].

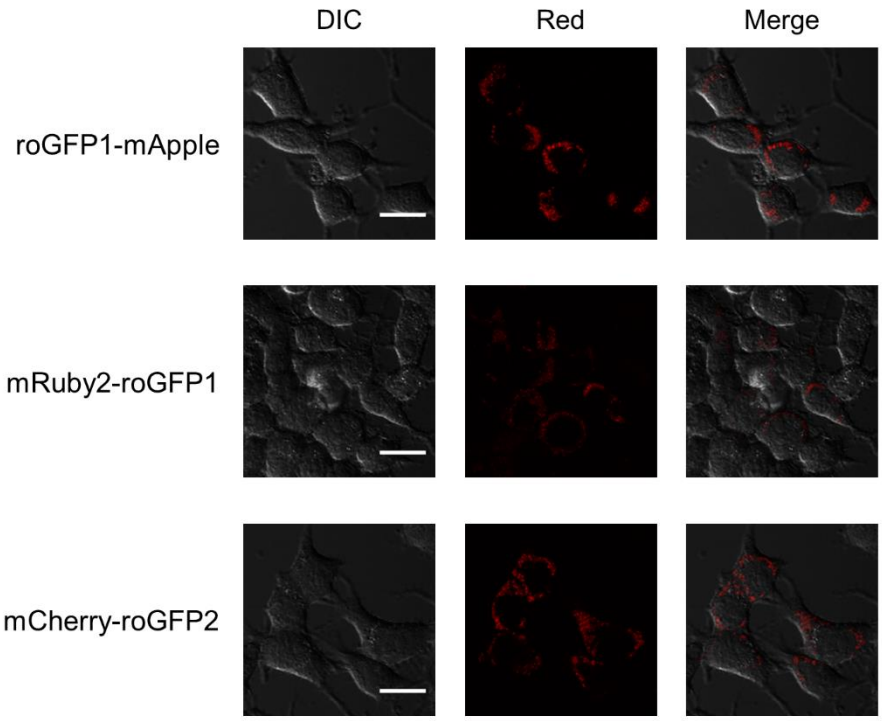

Figure 32 Confocal images show excellent subcellular localization for mito-roGFP-RFP constructs, targeted with the cox8 mitochondrial localization signal. Undifferentiated neuro2a cells exhibit large nuclei, causing the perinuclear appearance of the mitochondria, which are also rounded under high glucose conditions, as previously observed38

Ratiometric imaging was carried out with sequential collection of green and red emission, in which the red emission was localized to mitochondria (Figure 33). In order to measure redox potentials, we carried out baseline ratio measurements followed by a sensor calibration as previously described[15,78,115]. In the calibration, sensors were fully oxidized by the addition of 1 mM H_2O_2 to the imaging solution followed by full reduction with 10 mM DTT, and the calibration values were used to calculate the percent oxidation of the respective sensors (Figure 33)[15,78,115]. As expected from previous reports, the mitochondrially targeted sensors on average are more oxidized than the cytosolic sensors because of the alkaline pH of the mitochondrial matrix[15,78,115]. Taking compartment-specific pH into account (assuming cytosolic pH = 7.2 and mitochondrial pH = 8.0)[130,131], our average measurements of the cytosolic and mitochondrial redox potential, -298 ± 6 mV and -338 ± 5 mV (mean ± stdev) respectively, agree well with previously reported values (Figure 33)[15,78,115]. Importantly, our approach enables the direct comparison of the average mitochondrial and cytosolic redox potentials within the same cell. We discovered that

mitochondrial redox potential is set -40 mV relative to cytosolic redox potential, which was highly consistent across independent cells and sensor pairings (Figure 33). Thus, our roGFP-RFP FRET relay redox sensors enable steady-state differences in redox potential between subcellular compartments to be quantified. We next tested whether our new sensors could also quantify differences in subcellular redox dynamics.

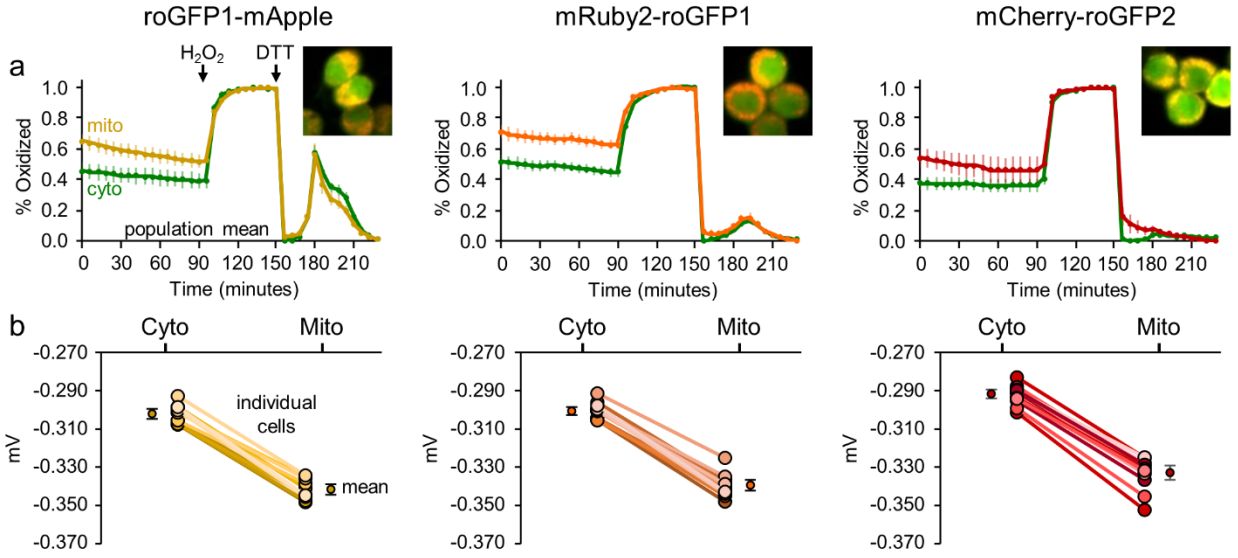

Figure 33 Simultaneous measurement of cytosolic and mitochondrial matrix redox potentials by the co-expression of cyto-roGFP and mito-roGFP-RFP in Neuro2A cells. (a) The mean response of the cell populations during the imaging time course (roGFP1-mApple, n=12 cells; mRuby2-roGFP1, n=14 cells; mCherry-roGFP2, n=15; errors are 95% confidence intervals). A baseline measurement period is followed by treatment with excess H_2O_2 and DTT (arrows) in order to calibrate the fully oxidized and fully reduced states of the sensor. The calibration is used to determine the sensor percent oxidation on a cell-by-cell basis for every experiment. (b) Single-cell analysis of compartment-specific redox potentials. Lines connect cytosolic and mitochondrial redox potentials for individual cells. Mean ± s.e.m. is shown for the population.

5.6 Heterogeneous Responses to Cytosolic Reductive Stress

We found that our dual-compartment imaging approach was able to reveal cell-to-cell population heterogeneity in compartment-specific responses to cytosolic reductive stress induced by exposure to excess N-acetylcysteine (NAC). In our initial redox studies (Figure 33), we observed that the Neuro2A cells exhibited an oxidative rebound following DTT addition during the final calibration phase, which indicates that Neuro2A cells respond to reductive stress. It has previously been observed that reductive stress causes a paradoxical oxidative response in HEK293,

H9c2, and other cell types[132–134]. NAC is a cell-permeant reductant that increases the levels of cytosolic reduced glutathione, but NAC is mitochondrially impermeant[132,134]. Interestingly, NAC-induced reductive stress causes an oxidative response in mitochondria but not the cytosol[132,134]. However, the compartment-specific difference in redox dynamics was determined by comparing population averages from cells separately transfected with cytosolic or mitochondrial roGFP-based probes, and therefore open questions remain regarding whether a difference in compartment-specific responses actually exists within a single cell and whether there is variability from cell-to-cell.

To answer this question, we used our dual-compartment imaging approach. After a baseline measurement period, Neuro2A cells expressing mitochondrial roGFP1-mApple and cytosolic roGFP1 were exposed to 6 mM NAC[132,134] followed by cell-by-cell sensor calibration with H2O2 and DTT after every experiment (Figure 34). At the level of the population average, we observed that both the cytosol and mitochondrial matrix experienced an initial reduction in redox potential upon addition of NAC; however, a small oxidative rebound was observed in the mitochondria after several minutes, which was absent in the cytosol (Figure 34). Our population measurement is in agreement with the previous population measurements, and the smaller magnitude of the oxidative rebound likely reflects cell-type differences[132,134]. Furthermore, our measurements also reveal a reductant-specific difference in the stress response because, while NAC-induced stress causes an oxidative rebound in mitochondria only, DTT-induced stress causes an oxidative rebound in both the cytosol and the mitochondria. Importantly, our dual-compartment imaging approach revealed heterogeneous responses at the single-cell level. That is, some cells showed no change, some cells showed a reduction, and some cells showed an oxidation of the mitochondria relative to the cytosol in response to NAC-induced stress (Figure 34). In order to quantify the cell-to-cell heterogeneity, we scored the difference in compartment-specific responses by measuring the ratio of the mito-roGFP1-mApple percent sensor oxidation to the cytosolic roGFP1 percent sensor oxidation, which reflects the change in mitochondrial redox relative to cytosolic redox upon NAC treatment (Figure 34). The heterogeneity reflects cell-to-cell differences in compartmentalized redox buffering capacity as well as cross-compartment redox coupling[68,132–134]. Thus, our roGFP-RFP FRET relay redox sensors enable differential compartment-specific dynamics to be quantified, showing that cytosolic stress can affect mitochondrial redox dynamics.

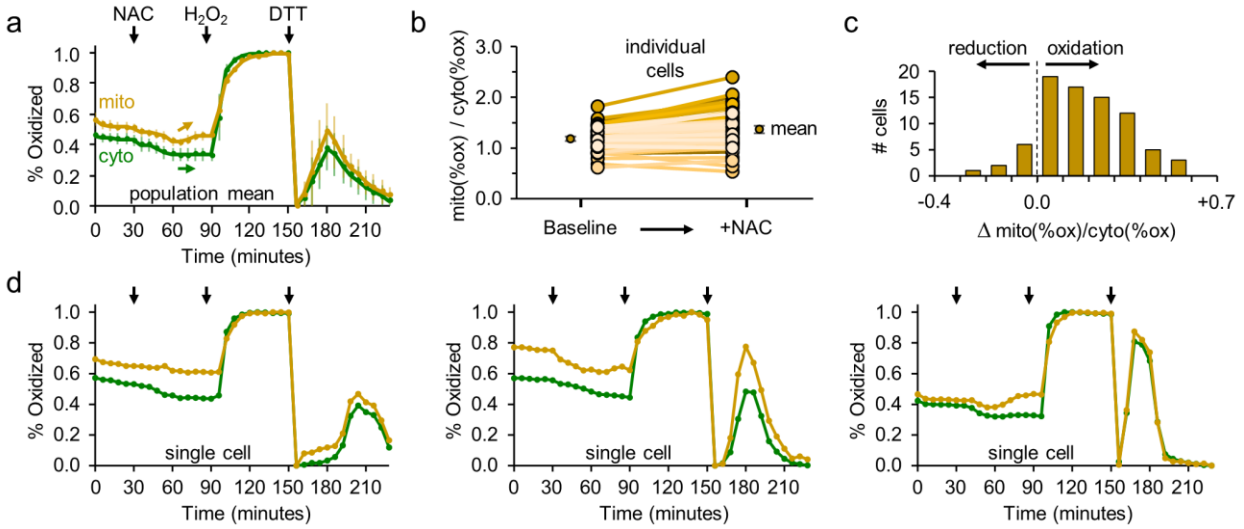

Figure 34 Single-cell heterogeneity in compartment-specific redox dynamics is observed in response to reductive stress when Neuro2A cells are treated with 6 mM N-acetylcysteine (NAC). (a) The mean compartment-specific time-course responses of the cell populations (n=80 cells, errors are 95% confidence intervals.). On average, Neuro2A cells co-expressing mito-roGFP1-mApple (yellow) and cyto-roGFP1 (green) exhibit an oxidative rebound in the mitochondria (yellow arrow) that is not observed in the cytosol (green arrow). (b-d) Single-cell analysis reveals population heterogeneity in the compartment-specific response to NAC. (b) The ratio of mitochondrial sensor oxidation to cytosolic sensor oxidation quantifies the variability in the mitochondrial redox change relative to the cytosol at the single-cell level. Lines show responses for individual cells, and the population mean ± s.e.m. is shown. (c) Cell count histogram shows the heterogeneity in the magnitude of the single-cell responses. (d) Examples of single-cell responses.

5.7 Heterogeneous Response to Mitochondrial Inhibition

Lastly, we tested whether our dual compartment imaging approach could reveal cell-to-cell population heterogeneity in compartment-specific responses to mitochondrial inhibition. The mitochondrial electron transport chain is a major source of both mitochondrial and cytosolic ROS. Inhibition of electron transport is expected to cause a decrease in ROS production, but low dose treatment with transport inhibitors or proton uncouplers can also cause an increase in ROS[132,135,136]. However, there remains an open question to what extent mitochondrial and cytosolic redox dynamics are coupled in the face of mitochondrial inhibition. To answer this question Neuroa2A cells expressing roGFP1-mApple in mitochondria and roGFP1 in the cytosol were grown in low glucose media in order to increase mitochondrial respiration prior to imaging[137,138]. During imaging, mitochondrial inhibition was induced with the complex I inhibitor rotenone and the

uncoupling protonophore carbonyl cyanide 4-(trifluoromethoxy)phenylhydrazone (FCCP) (Figure 35). At the level of the population average, we observed a trend suggesting that mitochondrial inhibition causes cytosolic reduction and mitochondrial oxidation (Figure 35). Importantly, our dual compartment imaging approached revealed cell-to-cell variation in the magnitude of mitochondrial oxidation relative to cytosolic reduction, and it also revealed that at the single-cell level complex compartment-specific dynamics can occur in response to mitochondrial inhibition (Figure 35). The heterogeneity may reflect cell-specific differences in respiratory efficiency as well as variability in redox buffer capacity in the face of metabolic inhibition. Overall, these results demonstrate that our roGFP-RFP FRET relay redox sensors can quantify how mitochondrial stress alters cytosolic redox dynamics at the single-cell level.

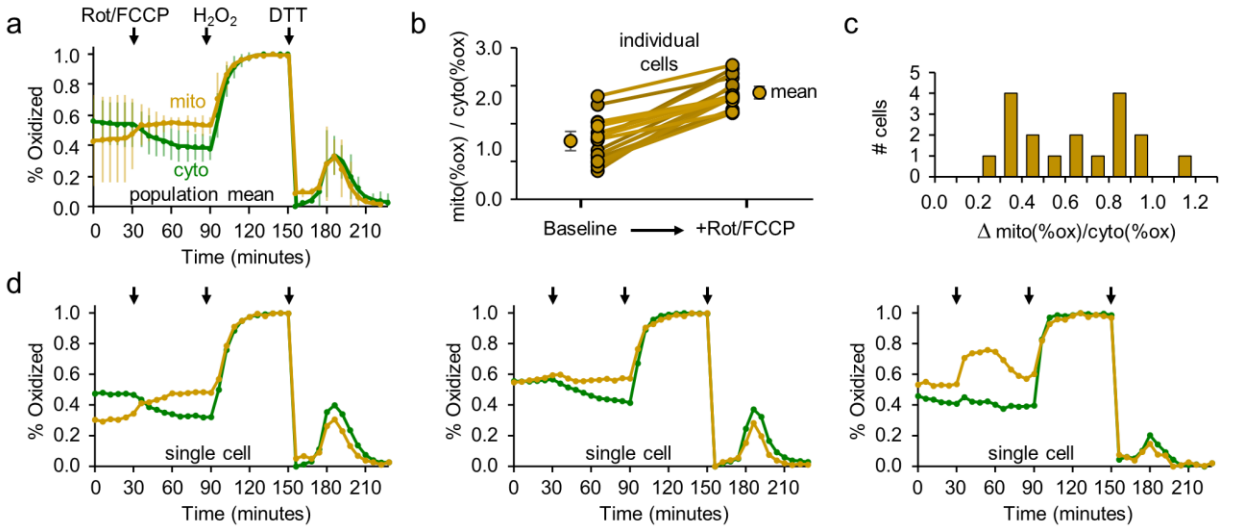

Figure 35 Single-cell heterogeneity in compartment-specific redox dynamics observed in response to metabolic stress when Neuro2A cells are treated with mitochondrial inhibitors (rot/FCCP: 2 µM rotenone and 2 µM FCCP) under low glucose conditions. (a) The mean compartment-specific time-course responses of the cell populations (n=18 cells, errors are 95% confidence intervals). On average, Neuro2A cells co-expressing mito-roGFP1-mApple (yellow) and cyto-roGFP1 (green) exhibit mitochondrial oxidation and cytosolic reduction in response to mitochondrial inhibition. (b-d) Single-cell analysis reveals significant heterogeneity in the extent to which mitochondria oxidize relative to the cytosol in individual cells. (b) The ratio of mitochondrial sensor oxidation to cytosolic sensor oxidation quantifies the variability in the mitochondrial redox change relative to the cytosol at the single-cell level. Lines show responses for individual cells, and the population mean ± s.e.m. is shown. (c) Cell count histogram shows the heterogeneity in the magnitude of the single-cell responses. (d) Examples of single-cell responses.

5.8 Conclusions

In this work, we developed a first-generation family of genetically encoded redox sensors that exhibit an excitation-ratiometric red fluorescence readout, and we demonstrated their utility in dual color, dual compartment live-cell imaging. These roGFP-RFP sensors utilize a FRET relay strategy to extend the emission spectrum of the donor roGFP out to red fluorescence wavelengths, and they preserve the redox sensing properties of the donor roGFP sensors. However, these first-generation sensors exhibit modest FRET efficiencies of approximately 30%, and they suffer from residual donor green fluorescence. Future optimization of the linker length could improve the FRET efficiency, but currently the residual donor emission leads to a spectral mixing problem that precludes the use of the roGFP-RFP sensors with other green fluorescent sensors if they are expressed in the same compartment. To circumvent this problem, we targeted the roGFP-RFP sensors to the mitochondria and roGFP sensors to the cytosol, and spatial localization allowed is to measure cytosolic and mitochondrial redox potentials simultaneously within the same cell for the first time to our knowledge. Thus, these sensors are advantageous for quantifying subcellular redox potentials because they can be targeted to organelles, they exhibit an emission profile that is spectrally distinct from green fluorescent redox sensors, and they preserve the redox sensing properties of the roGFP sensors. Our results also demonstrate that our FRET relay strategy can in principle be used to extend the fluorescence emission of other green fluorescent sensors of redox or other analytes into red wavelengths for multiparameter imaging studies.

5.9 Methods

Molecular Biology and Protein Expression

Standard molecular biology, protein expression, and nickel affinity purification procedures were used. Poly-histidine-tagged proteins were expressed using the pRsetB bacterial expression vector. Protein lacking the poly-histidine tag was expressed in mammalian cells using the GW1 mammalian expression vector with four copies of the COX8 mitochondrial signal sequence for mitochondrial localization or without any signal sequence for cytosolic expression38. Plasmid constructs are distributed via Addgene.

Steady-State Fluorescence Spectroscopy

For all spectroscopy measurements protein was diluted to a final concentration of 1 μM in 75 mM HEPES, 125 mM KCl, 1 mM EDTA, pH 7.0 – 7.3. Solutions were degassed under vacuum and purged with argon gas, and protein solutions were equilibrated with 10 mM reduced DTT (1, 4-Dithiothreitol) or 10 mM oxidized DTT (trans-4,5-Dihydroxy-1,2-dithiane) for 1 hour before measurements. Fluorescence anisotropy was determined for samples oxidized with 10 mM ox DTT. Redox titrations carried out in solutions in which the total DTT concentration was held constant at 10 mM while the reduced DTT to oxidized DTT ratio was varied. Midpoint potentials were determined as previously described20 and by fitting titration data to a Boltzmann equation.

Time-Resolved Fluorescence Spectroscopy

Fluorescence lifetimes were measured on a custom-built microscope using a 447 nm pulsed diode laser with an instrument response function full width at half maximum of 150 ps. roGFP donor emission was collected using a combination of 500 longpass and 550 shorpass filters. Empirical lifetimes were measured from the photon decays, and FRET efficiency was calculated as $1 - \tau_{roGFP\text{-}RFP}/\tau_{roGFP}$.

Live-Cell Imaging

Neuro2A cells were cultured according to ATCC recommendations and transfected with Effectene reagent (Qiagen) according to the manufacturer's instructions. Cells were imaged in glass-bottom 12-well plates at 6-minute intervals at room temperature on an Olympus IX83 microscope. DIC images were taken before and after experiments to verify cell health. Percent sensor oxidation and pH-adjusted midpoint potentials were calculated assuming cytosolic pH = 7.2 and mitochondrial matric pH = 8.0 as previously described9.

Data Analysis

Images were analyzed with ImageJ as previously described38. Briefly, ratio signals were manually measured from ratio images obtained by dividing fluorescence images on a pixel-by-pixel basis. Fluorescence images were background subtracted and thresholded at three standard deviations above the mean background to reject background pixels.

REFERENCES

(1) Chalfie, M.; Tu, Y.; Euskirchen, G.; Ward, W. W.; Prasher, D. C. Green Fluorescent Protein as a Marker for Gene Expression. *Science* **1994**, *263* (5148), 802–805.

(2) Gao, H.; Liu, W.; Yang, S.; Zhang, W.; Li, X.; Qin, H.; Wang, W.; Zhao, C. Detection of Circulating Tumor Cells Using OHSV1-HTERT-GFP in Lung Cancer. *Thorac. Cancer* **2018**, *9* (1), 44–50. https://doi.org/10.1111/1759-7714.12526.

(3) Bouvet, M.; Hoffman, R. M. Tumor Imaging Technologies in Mouse Models. *Methods Mol. Biol. Clifton NJ* **2015**, *1267*, 321–348. https://doi.org/10.1007/978-1-4939-2297-0_16.

(4) Cui, Y.; Gao, C.; Zhao, Q.; Jiang, L. Using Fluorescent Protein Fusions to Study Protein Subcellular Localization and Dynamics in Plant Cells. *Methods Mol. Biol. Clifton NJ* **2016**, *1474*, 113–123. https://doi.org/10.1007/978-1-4939-6352-2_7.

(5) Shibata, A.; Machida, J.; Yamaguchi, S.; Kimura, M.; Tatematsu, T.; Miyachi, H.; Nakayama, A.; Shimozato, K.; Tokita, Y. Identification of Nuclear Localization Signals in the Human Homeoprotein MSX1. *Biochem. Cell Biol. Biochim. Biol. Cell.* **2018**, *96* (4), 483–489. https://doi.org/10.1139/bcb-2017-0263.

(6) Kaddoum, L.; Magdeleine, E.; Waldo, G. S.; Joly, E.; Cabantous, S. One-Step Split GFP Staining for Sensitive Protein Detection and Localization in Mammalian Cells. *BioTechniques* **2010**, *49* (4), 727–728, 730, 732 passim. https://doi.org/10.2144/000113512.

(7) Belardinelli, J. M.; Jackson, M. Green Fluorescent Protein as a Protein Localization and Topological Reporter in Mycobacteria. *Tuberc. Edinb. Scotl.* **2017**, *105*, 13–17. https://doi.org/10.1016/j.tube.2017.04.001.

(8) Matz, M. V.; Fradkov, A. F.; Labas, Y. A.; Savitsky, A. P.; Zaraisky, A. G.; Markelov, M. L.; Lukyanov, S. A. Fluorescent Proteins from Nonbioluminescent Anthozoa Species. *Nat. Biotechnol.* **1999**, *17* (10), 969. https://doi.org/10.1038/13657.

(9) Mishin, A. S.; Subach, F. V.; Yampolsky, I. V.; King, W.; Lukyanov, K. A.; Verkhusha, V. V. The First Mutant of the Aequorea Victoria Green Fluorescent Protein That Forms a Red Chromophore. *Biochemistry* **2008**, *47* (16), 4666–4673. https://doi.org/10.1021/bi702130s.

(10) Ai, H.-W. Fluorescent-Protein-Based Probes: General Principles and Practices. *Anal. Bioanal. Chem.* **2015**, *407* (1), 9–15. https://doi.org/10.1007/s00216-014-8236-3.

(11) Miesenböck, G.; De Angelis, D. A.; Rothman, J. E. Visualizing Secretion and Synaptic Transmission with PH-Sensitive Green Fluorescent Proteins. *Nature* **1998**, *394* (6689), 192–195. https://doi.org/10.1038/28190.

(12) Tantama, M.; Hung, Y. P.; Yellen, G. Imaging Intracellular PH in Live Cells with a Genetically Encoded Red Fluorescent Protein Sensor. *J. Am. Chem. Soc.* **2011**, *133* (26), 10034–10037. https://doi.org/10.1021/ja202902d.

(13) Rajendran, M.; Claywell, B.; Haynes, E. P.; Scales, U.; Henning, C. K.; Tantama, M. Imaging PH Dynamics Simultaneously in Two Cellular Compartments Using a Ratiometric PH-Sensitive Mutant of MCherry. *ACS Omega* **2018**, *3* (8), 9476–9486. https://doi.org/10.1021/acsomega.8b00655.

(14) Dooley, C. T.; Dore, T. M.; Hanson, G. T.; Jackson, W. C.; Remington, S. J.; Tsien, R. Y. Imaging Dynamic Redox Changes in Mammalian Cells with Green Fluorescent Protein Indicators. *J. Biol. Chem.* **2004**, *279* (21), 22284–22293. https://doi.org/10.1074/jbc.M312847200.

(15) Hanson, G. T.; Aggeler, R.; Oglesbee, D.; Cannon, M.; Capaldi, R. A.; Tsien, R. Y.; Remington, S. J. Investigating Mitochondrial Redox Potential with Redox-Sensitive Green Fluorescent Protein Indicators. *J. Biol. Chem.* **2004**, *279* (13), 13044–13053. https://doi.org/10.1074/jbc.M312846200.

(16) Jing, M.; Zhang, P.; Wang, G.; Feng, J.; Mesik, L.; Zeng, J.; Jiang, H.; Wang, S.; Looby, J. C.; Guagliardo, N. A.; et al. A Genetically Encoded Fluorescent Acetylcholine Indicator for *in Vitro* and *in Vivo* Studies. *Nat. Biotechnol.* **2018**, *36* (8), 726–737. https://doi.org/10.1038/nbt.4184.

(17) Arai, S.; Kriszt, R.; Harada, K.; Looi, L.-S.; Matsuda, S.; Wongso, D.; Suo, S.; Ishiura, S.; Tseng, Y.-H.; Raghunath, M.; et al. RGB-Color Intensiometric Indicators to Visualize Spatiotemporal Dynamics of ATP in Single Cells. *Angew. Chem. Int. Ed Engl.* **2018**, *57* (34), 10873–10878. https://doi.org/10.1002/anie.201804304.

(18) Nakai, J.; Ohkura, M.; Imoto, K. A High Signal-to-Noise Ca(2+) Probe Composed of a Single Green Fluorescent Protein. *Nat. Biotechnol.* **2001**, *19* (2), 137–141. https://doi.org/10.1038/84397.

(19) Jin, L.; Han, Z.; Platisa, J.; Wooltorton, J. R. A.; Cohen, L. B.; Pieribone, V. A. Single Action Potentials and Subthreshold Electrical Events Imaged in Neurons with a Fluorescent Protein Voltage Probe. *Neuron* **2012**, *75* (5), 779–785. https://doi.org/10.1016/j.neuron.2012.06.040.

(20) Berg, J.; Hung, Y. P.; Yellen, G. A Genetically Encoded Fluorescent Reporter of ATP/ADP Ratio. *Nat. Methods* **2009**, *6* (2), 161–166. https://doi.org/10.1038/nmeth.1288.

(21) Yaginuma, H.; Kawai, S.; Tabata, K. V.; Tomiyama, K.; Kakizuka, A.; Komatsuzaki, T.; Noji, H.; Imamura, H. Diversity in ATP Concentrations in a Single Bacterial Cell Population Revealed by Quantitative Single-Cell Imaging. *Sci. Rep.* **2014**, *4*. https://doi.org/10.1038/srep06522.

(22) Schnitzler, H.; V Kalko, E. K.; Saillant, P. A.; Simmons, J. A.; Bouffard, F. H.; Lee, D. N.; scripts, M.; Jensen, F.; Canfield, D.; Surlykke, A.; et al. An Expanded Palette of Genetically Encoded Ca2+ Indicators. *21 J P Revel J Cell Biol* **2001**, *51*, 6094. https://doi.org/10.1126/science.1207309.

(23) Wu, J.; Abdelfattah, A. S.; Miraucourt, L. S.; Kutsarova, E.; Ruangkittisakul, A.; Zhou, H.; Ballanyi, K.; Wicks, G.; Drobizhev, M.; Rebane, A.; et al. A Long Stokes Shift Red Fluorescent Ca2+ Indicator Protein for Two-Photon and Ratiometric Imaging. *Nat. Commun.* **2014**, *5* (1), 5262. https://doi.org/10.1038/ncomms6262.

(24) Imamura, H.; Huynh Nhat, K. P.; Togawa, H.; Saito, K.; Iino, R.; Kato-Yamada, Y.; Nagai, T.; Noji, H. Visualization of ATP Levels inside Single Living Cells with Fluorescence Resonance Energy Transfer-Based Genetically Encoded Indicators. *Proc. Natl. Acad. Sci. U. S. A.* **2009**, *106* (37), 15651–15656. https://doi.org/10.1073/pnas.0904764106.

(25) Thestrup, T.; Litzlbauer, J.; Bartholomäus, I.; Mues, M.; Russo, L.; Dana, H.; Kovalchuk, Y.; Liang, Y.; Kalamakis, G.; Laukat, Y.; et al. Optimized Ratiometric Calcium Sensors for Functional *in Vivo* Imaging of Neurons and T Lymphocytes. *Nat. Methods* **2014**, *11* (2), 175–182. https://doi.org/10.1038/nmeth.2773.

(26) Chen, Y.; Saulnier, J. L.; Yellen, G.; Sabatini, B. L. A PKA Activity Sensor for Quantitative Analysis of Endogenous GPCR Signaling via 2-Photon FRET-FLIM Imaging. *Front. Pharmacol.* **2014**, *5*, 56. https://doi.org/10.3389/fphar.2014.00056.

(27) Gritton, H. J.; Howe, W. M.; Mallory, C. S.; Hetrick, V. L.; Berke, J. D.; Sarter, M. Cortical Cholinergic Signaling Controls the Detection of Cues. *Proc. Natl. Acad. Sci. U. S. A.* **2016**, *113* (8), E1089-1097. https://doi.org/10.1073/pnas.1516134113.

(28) Zaborszky, L. The Modular Organization of Brain Systems. Basal Forebrain: The Last Frontier. *Prog. Brain Res.* **2002**, *136*, 359–372.

(29) Parikh, V.; St Peters, M.; Blakely, R. D.; Sarter, M. The Presynaptic Choline Transporter Imposes Limits on Sustained Cortical Acetylcholine Release and Attention. *J. Neurosci. Off. J. Soc. Neurosci.* **2013**, *33* (6), 2326–2337. https://doi.org/10.1523/JNEUROSCI.4993-12.2013.

(30) Bohnen, N. I.; Frey, K. A.; Studenski, S.; Kotagal, V.; Koeppe, R. A.; Scott, P. J. H.; Albin, R. L.; Müller, M. L. T. M. Gait Speed in Parkinson Disease Correlates with Cholinergic Degeneration. *Neurology* **2013**, *81* (18), 1611–1616. https://doi.org/10.1212/WNL.0b013e3182a9f558.

(31) Perez-Lloret, S.; Barrantes, F. J. Deficits in Cholinergic Neurotransmission and Their Clinical Correlates in Parkinson's Disease. *NPJ Park. Dis.* **2016**, *2*, 16001. https://doi.org/10.1038/npjparkd.2016.1.

(32) Narayanan, N. S.; Rodnitzky, R. L.; Uc, E. Y. Prefrontal Dopamine Signaling and Cognitive Symptoms of Parkinson's Disease. *Rev. Neurosci.* **2013**, *24* (3), 267–278. https://doi.org/10.1515/revneuro-2013-0004.

(33) Wang, L.; Almeida, L. E. F.; Spornick, N. A.; Kenyon, N.; Kamimura, S.; Khaibullina, A.; Nouraie, M.; Quezado, Z. M. N. Modulation of Social Deficits and Repetitive Behaviors in a Mouse Model of Autism: The Role of the Nicotinic Cholinergic System. *Psychopharmacology (Berl.)* **2015**, *232* (23), 4303–4316. https://doi.org/10.1007/s00213-015-4058-z.

(34) Luchicchi, A.; Bloem, B.; Viaña, J. N. M.; Mansvelder, H. D.; Role, L. W. Illuminating the Role of Cholinergic Signaling in Circuits of Attention and Emotionally Salient Behaviors. *Front. Synaptic Neurosci.* **2014**, *6*, 24. https://doi.org/10.3389/fnsyn.2014.00024.

(35) Lockman, P. R.; Allen, D. D. The Transport of Choline. *Drug Dev. Ind. Pharm.* **2002**, *28* (7), 749–771. https://doi.org/10.1081/DDC-120005622.

(36) Sarter, M.; Parikh, V. Choline Transporters, Cholinergic Transmission and Cognition. *Nat. Rev. Neurosci.* **2005**, *6* (1), 48–56. https://doi.org/10.1038/nrn1588.

(37) Parikh, V.; Sarter, M. Cortical Choline Transporter Function Measured in Vivo Using Choline-Sensitive Microelectrodes: Clearance of Endogenous and Exogenous Choline and Effects of Removal of Cholinergic Terminals. *J. Neurochem.* **2006**, *97* (2), 488–503. https://doi.org/10.1111/j.1471-4159.2006.03766.x.

(38) Bruno, J. P.; Gash, C.; Martin, B.; Zmarowski, A.; Pomerleau, F.; Burmeister, J.; Huettl, P.; Gerhardt, G. A. Second-by-Second Measurement of Acetylcholine Release in Prefrontal Cortex. *Eur. J. Neurosci.* **2006**, *24* (10), 2749–2757. https://doi.org/10.1111/j.1460-9568.2006.05176.x.

(39) Parikh, V.; Kozak, R.; Martinez, V.; Sarter, M. Prefrontal Acetylcholine Release Controls Cue Detection on Multiple Timescales. *Neuron* **2007**, *56* (1), 141–154. https://doi.org/10.1016/j.neuron.2007.08.025.

(40) Song, P.; Hershey, N. D.; Mabrouk, O. S.; Slaney, T. R.; Kennedy, R. T. Mass Spectrometry "Sensor" for in Vivo Acetylcholine Monitoring. *Anal. Chem.* **2012**, *84* (11), 4659–4664. https://doi.org/10.1021/ac301203m.

(41) Bales, K. R.; Tzavara, E. T.; Wu, S.; Wade, M. R.; Bymaster, F. P.; Paul, S. M.; Nomikos, G. G. Cholinergic Dysfunction in a Mouse Model of Alzheimer Disease Is Reversed by an Anti-A Beta Antibody. *J. Clin. Invest.* **2006**, *116* (3), 825–832. https://doi.org/10.1172/JCI27120.

(42) Sarter, M.; Parikh, V.; Howe, W. M. Phasic Acetylcholine Release and the Volume Transmission Hypothesis: Time to Move On. *Nat. Rev. Neurosci.* **2009**, *10* (5), 383–390. https://doi.org/10.1038/nm2635.

(43) Newman, R. H.; Fosbrink, M. D.; Zhang, J. Genetically Encodable Fluorescent Biosensors for Tracking Signaling Dynamics in Living Cells. *Chem. Rev.* **2011**, *111* (5), 3614–3666. https://doi.org/10.1021/cr100002u.

(44) Tantama, M.; Hung, Y. P.; Yellen, G. Optogenetic Reporters: Fluorescent Protein-Based Genetically Encoded Indicators of Signaling and Metabolism in the Brain. *Prog. Brain Res.* **2012**, *196*, 235–263. https://doi.org/10.1016/B978-0-444-59426-6.00012-4.

(45) Nguyen, Q.-T.; Schroeder, L. F.; Mank, M.; Muller, A.; Taylor, P.; Griesbeck, O.; Kleinfeld, D. An in Vivo Biosensor for Neurotransmitter Release and in Situ Receptor Activity. *Nat. Neurosci.* **2010**, *13* (1), 127–132. https://doi.org/10.1038/nn.2469.

(46) Rodriguez-Diaz, R.; Dando, R.; Huang, Y. A.; Berggren, P.-O.; Roper, S. D.; Caicedo, A. Real-Time Detection of Acetylcholine Release from the Human Endocrine Pancreas. *Nat. Protoc.* **2012**, *7* (6), 1015–1023. https://doi.org/10.1038/nprot.2012.040.

(47) Lacin, E.; Muller, A.; Fernando, M.; Kleinfeld, D.; Slesinger, P. A. Construction of Cell-Based Neurotransmitter Fluorescent Engineered Reporters (CNiFERs) for Optical Detection of Neurotransmitters In Vivo. *J. Vis. Exp. JoVE* **2016**, No. 111. https://doi.org/10.3791/53290.

(48) Tantama, M.; Martínez-François, J. R.; Mongeon, R.; Yellen, G. Imaging Energy Status in Live Cells with a Fluorescent Biosensor of the Intracellular ATP-to-ADP Ratio. *Nat. Commun.* **2013**, *4*, 2550. https://doi.org/10.1038/ncomms3550.

(49) Conley, J. M.; Radhakrishnan, S.; Valentino, S. A.; Tantama, M. Imaging Extracellular ATP with a Genetically-Encoded, Ratiometric Fluorescent Sensor. *PLOS ONE* **2017**, *12* (11), e0187481. https://doi.org/10.1371/journal.pone.0187481.

(50) Saito, K.; Chang, Y.-F.; Horikawa, K.; Hatsugai, N.; Higuchi, Y.; Hashida, M.; Yoshida, Y.; Matsuda, T.; Arai, Y.; Nagai, T. Luminescent Proteins for High-Speed Single-Cell and Whole-Body Imaging. *Nat. Commun.* **2012**, *3*, 1262. https://doi.org/10.1038/ncomms2248.

(51) Yoshida, T.; Kakizuka, A.; Imamura, H. BTeam, a Novel BRET-Based Biosensor for the Accurate Quantification of ATP Concentration within Living Cells. *Sci. Rep.* **2016**, *6*, 39618. https://doi.org/10.1038/srep39618.

(52) Burnstock, G. Purinergic Mechanisms and Pain. *Adv. Pharmacol. San Diego Calif* **2016**, *75*, 91–137. https://doi.org/10.1016/bs.apha.2015.09.001.

(53) Inoue, K. Purinergic Signaling in Microglia in the Pathogenesis of Neuropathic Pain. *Proc. Jpn. Acad. Ser. B Phys. Biol. Sci.* **2017**, *93* (4), 174–182. https://doi.org/10.2183/pjab.93.011.

(54) Magni, G.; Riccio, D.; Ceruti, S. Tackling Chronic Pain and Inflammation through the Purinergic System. *Curr. Med. Chem.* **2018**, *25* (32), 3830–3865. https://doi.org/10.2174/0929867324666170710110630.

(55) Ferrari, D.; McNamee, E. N.; Idzko, M.; Gambari, R.; Eltzschig, H. K. Purinergic Signaling During Immune Cell Trafficking. *Trends Immunol.* **2016**, *37* (6), 399–411. https://doi.org/10.1016/j.it.2016.04.004.

(56) Ledderose, C.; Bao, Y.; Kondo, Y.; Fakhari, M.; Slubowski, C.; Zhang, J.; Junger, W. G. Purinergic Signaling and the Immune Response in Sepsis: A Review. *Clin. Ther.* **2016**, *38* (5), 1054–1065. https://doi.org/10.1016/j.clinthera.2016.04.002.

(57) Zhang, X.; Qin, J.; Zou, J.; Lv, Z.; Tan, B.; Shi, J.; Zhao, Y.; Ren, H.; Liu, M.; Qian, M.; et al. Extracellular ADP Facilitates Monocyte Recruitment in Bacterial Infection via ERK Signaling. *Cell. Mol. Immunol.* **2018**, *15* (1), 58–73. https://doi.org/10.1038/cmi.2016.56.

(58) Kunzelmann, S.; Webb, M. R. A Biosensor for Fluorescent Determination of ADP with High Time Resolution. *J. Biol. Chem.* **2009**, *284* (48), 33130–33138. https://doi.org/10.1074/jbc.M109.047118.

(59) Kunzelmann, S.; Webb, M. R. A Fluorescent, Reagentless Biosensor for ADP Based on Tetramethylrhodamine-Labeled ParM. *ACS Chem. Biol.* **2010**, *5* (4), 415–425. https://doi.org/10.1021/cb9003173.

(60) Sies, H.; Berndt, C.; Jones, D. P. Oxidative Stress. *Annu. Rev. Biochem.* **2017**, *86* (1), 715–748. https://doi.org/10.1146/annurev-biochem-061516-045037.

(61) Dickinson, B. C.; Chang, C. J. Chemistry and Biology of Reactive Oxygen Species in Signaling or Stress Responses. *Nat. Chem. Biol.* **2011**, *7* (8), 504–511. https://doi.org/10.1038/nchembio.607.

(62) Schieber, M.; Chandel, N. S. ROS Function in Redox Signaling and Oxidative Stress. *Curr. Biol.* **2014**, *24* (10), R453–R462. https://doi.org/10.1016/j.cub.2014.03.034.

(63) Surmeier, D. J.; Guzman, J. N.; Sanchez, J.; Schumacker, P. T. Physiological Phenotype and Vulnerability in Parkinson's Disease. *Cold Spring Harb. Perspect. Med.* **2012**, *2* (7), a009290–a009290. https://doi.org/10.1101/cshperspect.a009290.

(64) Gorrini, C.; Harris, I. S.; Mak, T. W. Modulation of Oxidative Stress as an Anticancer Strategy. *Nat. Rev. Drug Discov.* **2013**, *12* (12), 931–947. https://doi.org/10.1038/nrd4002.

(65) Brewer, A. C.; Mustafi, S. B.; Murray, T. V. A.; Rajasekaran, N. S.; Benjamin, I. J. Reductive Stress Linked to Small HSPs, G6PD, and Nrf2 Pathways in Heart Disease. *Antioxid. Redox Signal.* **2013**, *18* (9), 1114–27. https://doi.org/10.1089/ars.2012.4914.

(66) Griendling, K. K.; Touyz, R. M.; Zweier, J. L.; Dikalov, S.; Chilian, W.; Chen, Y.-R.; Harrison, D. G.; Bhatnagar, A.; American Heart Association Council on Basic Cardiovascular Sciences. Measurement of Reactive Oxygen Species, Reactive Nitrogen Species, and Redox-Dependent Signaling in the Cardiovascular System. *Circ. Res.* **2016**, *119* (5), e39–e75. https://doi.org/10.1161/RES.0000000000000110.

(67) Paulsen, C. E.; Carroll, K. S. Cysteine-Mediated Redox Signaling: Chemistry, Biology, and Tools for Discovery. *Chem. Rev.* **2013**, *113* (7), 4633–4679. https://doi.org/10.1021/cr300163e.

(68) Dey, S.; Sidor, A.; O'Rourke, B. Compartment-Specific Control of Reactive Oxygen Species Scavenging by Antioxidant Pathway Enzymes. *J. Biol. Chem.* **2016**, *291* (21), 11185–11197. https://doi.org/10.1074/jbc.M116.726968.

(69) Al-Mehdi, A.-B.; Pastukh, V. M.; Swiger, B. M.; Reed, D. J.; Patel, M. R.; Bardwell, G. C.; Pastukh, V. V.; Alexeyev, M. F.; Gillespie, M. N. Perinuclear Mitochondrial Clustering Creates an Oxidant-Rich Nuclear Domain Required for Hypoxia-Induced Transcription. *Sci. Signal.* **2012**, *5* (231), ra47. https://doi.org/10.1126/scisignal.2002712.

(70) Booth, D. M.; Enyedi, B.; Geiszt, M.; Várnai, P.; Hajnóczky, G. Redox Nanodomains Are Induced by and Control Calcium Signaling at the ER-Mitochondrial Interface. *Mol. Cell* **2016**, *63* (2), 240–8. https://doi.org/10.1016/j.molcel.2016.05.040.

(71) Exposito-Rodriguez, M.; Laissue, P. P.; Yvon-Durocher, G.; Smirnoff, N.; Mullineaux, P. M. Photosynthesis-Dependent H2O2 Transfer from Chloroplasts to Nuclei Provides a High-Light Signalling Mechanism. *Nat. Commun.* **2017**, *8* (1), 49. https://doi.org/10.1038/s41467-017-00074-w.

(72) Quir?s, P. M.; Mottis, A.; Auwerx, J. Mitonuclear Communication in Homeostasis and Stress. *Nat. Rev. Mol. Cell Biol.* **2016**, *17* (4), 213–226. https://doi.org/10.1038/nrm.2016.23.

(73) Shadel, G. S.; Horvath, T. L. Mitochondrial ROS Signaling in Organismal Homeostasis. *Cell* **2015**, *163* (3), 560–569. https://doi.org/10.1016/j.cell.2015.10.001.

(74) Morgan, B.; Sobotta, M. C.; Dick, T. P. Measuring E GSH and H 2O 2 with RoGFP2-Based Redox Probes. *Free Radic. Biol. Med.* **2011**, *51* (11), 1943–1951. https://doi.org/10.1016/j.freeradbiomed.2011.08.035.

(75) Schwarzländer, M.; Fricker, M. D.; Sweetlove, L. J. Monitoring the in Vivo Redox State of Plant Mitochondria: Effect of Respiratory Inhibitors, Abiotic Stress and Assessment of Recovery from Oxidative Challenge. *Biochim. Biophys. Acta - Bioenerg.* **2009**, *1787* (5), 468–475. https://doi.org/10.1016/j.bbabio.2009.01.020.

(76) Ermakova, Y. G.; Bilan, D. S.; Matlashov, M. E.; Mishina, N. M.; Markvicheva, K. N.; Subach, O. M.; Subach, F. V.; Bogeski, I.; Hoth, M.; Enikolopov, G.; et al. Red Fluorescent Genetically Encoded Indicator for Intracellular Hydrogen Peroxide. *Nat. Commun.* **2014**, *5*, 5222. https://doi.org/10.1038/ncomms6222.

(77) Lukyanov, K. A.; Belousov, V. V. Genetically Encoded Fluorescent Redox Sensors. *Biochim. Biophys. Acta* **2014**, *1840* (2), 745–756. https://doi.org/10.1016/j.bbagen.2013.05.030.

(78) Meyer, A. J.; Dick, T. P. Fluorescent Protein-Based Redox Probes. *Antioxid. Redox Signal.* **2010**, *13* (5), 621–650. https://doi.org/10.1089/ars.2009.2948.

(79) Fan, Y.; Chen, Z.; Ai, H. Monitoring Redox Dynamics in Living Cells with a Redox-Sensitive Red Fluorescent Protein. *Anal. Chem.* **2015**, *87* (5), 2802–2810. https://doi.org/10.1021/ac5041988.

(80) Lawrence, J. J. Cholinergic Control of GABA Release: Emerging Parallels between Neocortex and Hippocampus. *Trends Neurosci.* **2008**, *31* (7), 317–327. https://doi.org/10.1016/j.tins.2008.03.008.

(81) Picciotto, M. R.; Higley, M. J.; Mineur, Y. S. Acetylcholine as a Neuromodulator: Cholinergic Signaling Shapes Nervous System Function and Behavior. *Neuron* **2012**, *76* (1), 116–129. https://doi.org/10.1016/j.neuron.2012.08.036.

(82) Drenan, R. M.; Grady, S. R.; Whiteaker, P.; McClure-Begley, T.; McKinney, S.; Miwa, J. M.; Bupp, S.; Heintz, N.; McIntosh, J. M.; Bencherif, M.; et al. In Vivo Activation of Midbrain Dopamine Neurons via Sensitized, High-Affinity Alpha 6 Nicotinic Acetylcholine Receptors. *Neuron* **2008**, *60* (1), 123–136. https://doi.org/10.1016/j.neuron.2008.09.009.

(83) Drenan, R. M.; Grady, S. R.; Steele, A. D.; McKinney, S.; Patzlaff, N. E.; McIntosh, J. M.; Marks, M. J.; Miwa, J. M.; Lester, H. A. Cholinergic Modulation of Locomotion and Striatal Dopamine Release Is Mediated by Alpha6alpha4* Nicotinic Acetylcholine Receptors. *J. Neurosci. Off. J. Soc. Neurosci.* **2010**, *30* (29), 9877–9889. https://doi.org/10.1523/JNEUROSCI.2056-10.2010.

(84) Eggermann, E.; Kremer, Y.; Crochet, S.; Petersen, C. C. H. Cholinergic Signals in Mouse Barrel Cortex during Active Whisker Sensing. *Cell Rep.* **2014**, *9* (5), 1654–1660. https://doi.org/10.1016/j.celrep.2014.11.005.

(85) Bargmann, C. I.; Marder, E. From the Connectome to Brain Function. *Nat. Methods* **2013**, *10* (6), 483–490.
(86) Threlfell, S.; Lalic, T.; Platt, N. J.; Jennings, K. A.; Deisseroth, K.; Cragg, S. J. Striatal Dopamine Release Is Triggered by Synchronized Activity in Cholinergic Interneurons. *Neuron* **2012**, *75* (1), 58–64. https://doi.org/10.1016/j.neuron.2012.04.038.
(87) Cachope, R.; Mateo, Y.; Mathur, B. N.; Irving, J.; Wang, H.-L.; Morales, M.; Lovinger, D. M.; Cheer, J. F. Selective Activation of Cholinergic Interneurons Enhances Accumbal Phasic Dopamine Release: Setting the Tone for Reward Processing. *Cell Rep.* **2012**, *2* (1), 33–41. https://doi.org/10.1016/j.celrep.2012.05.011.
(88) Nelson, A. B.; Hammack, N.; Yang, C. F.; Shah, N. M.; Seal, R. P.; Kreitzer, A. C. Striatal Cholinergic Interneurons Drive GABA Release from Dopamine Terminals. *Neuron* **2014**, *82* (1), 63–70. https://doi.org/10.1016/j.neuron.2014.01.023.
(89) Chuhma, N.; Mingote, S.; Moore, H.; Rayport, S. Dopamine Neurons Control Striatal Cholinergic Neurons via Regionally Heterogeneous Dopamine and Glutamate Signaling. *Neuron* **2014**, *81* (4), 901–912. https://doi.org/10.1016/j.neuron.2013.12.027.
(90) Straub, C.; Tritsch, N. X.; Hagan, N. A.; Gu, C.; Sabatini, B. L. Multiphasic Modulation of Cholinergic Interneurons by Nigrostriatal Afferents. *J. Neurosci. Off. J. Soc. Neurosci.* **2014**, *34* (25), 8557–8569. https://doi.org/10.1523/JNEUROSCI.0589-14.2014.
(91) Dupont, L.; Garcia, I.; Poggi, M.-C.; Alloing, G.; Mandon, K.; Le Rudulier, D. The Sinorhizobium Meliloti ABC Transporter Cho Is Highly Specific for Choline and Expressed in Bacteroids from Medicago Sativa Nodules. *J. Bacteriol.* **2004**, *186* (18), 5988–5996. https://doi.org/10.1128/JB.186.18.5988-5996.2004.
(92) Oswald, C.; Smits, S. H. J.; Höing, M.; Sohn-Bösser, L.; Dupont, L.; Le Rudulier, D.; Schmitt, L.; Bremer, E. Crystal Structures of the Choline/Acetylcholine Substrate-Binding Protein ChoX from Sinorhizobium Meliloti in the Liganded and Unliganded-Closed States. *J. Biol. Chem.* **2008**, *283* (47), 32848–32859. https://doi.org/10.1074/jbc.M806021200.
(93) Oswald, C.; Smits, S. H. J.; Höing, M.; Bremer, E.; Schmitt, L. Structural Analysis of the Choline-Binding Protein ChoX in a Semi-Closed and Ligand-Free Conformation. *Biol. Chem.* **2009**, *390* (11), 1163–1170. https://doi.org/10.1515/BC.2009.113.
(94) Marvin, J. S.; Schreiter, E. R.; Echevarría, I. M.; Looger, L. L. A Genetically Encoded, High-Signal-to-Noise Maltose Sensor. *Proteins* **2011**, *79* (11), 3025–3036. https://doi.org/10.1002/prot.23118.
(95) Marvin, J. S.; Borghuis, B. G.; Tian, L.; Cichon, J.; Harnett, M. T.; Akerboom, J.; Gordus, A.; Renninger, S. L.; Chen, T.-W.; Bargmann, C. I.; et al. An Optimized Fluorescent Probe for Visualizing Glutamate Neurotransmission. *Nat. Methods* **2013**, *10* (2), 162–170. https://doi.org/10.1038/nmeth.2333.
(96) Akerboom, J.; Carreras Calderón, N.; Tian, L.; Wabnig, S.; Prigge, M.; Tolö, J.; Gordus, A.; Orger, M. B.; Severi, K. E.; Macklin, J. J.; et al. Genetically Encoded Calcium Indicators for Multi-Color Neural Activity Imaging and Combination with Optogenetics. *Front. Mol. Neurosci.* **2013**, *6*. https://doi.org/10.3389/fnmol.2013.00002.
(97) Suzuki, K.; Kimura, T.; Shinoda, H.; Bai, G.; Daniels, M. J.; Arai, Y.; Nakano, M.; Nagai, T. Five Colour Variants of Bright Luminescent Protein for Real-Time Multicolour Bioimaging. *Nat. Commun.* **2016**, *7*, 1–10. https://doi.org/10.1038/ncomms13718.
(98) England, C. G.; Ehlerding, E. B.; Cai, W. NanoLuc: A Small Luciferase Is Brightening up the Field of Bioluminescence. *Bioconjug. Chem.* **2016**, *27* (5), 1175–1187. https://doi.org/10.1021/acs.bioconjchem.6b00112.

(99) Shaner, N. C.; Campbell, R. E.; Steinbach, P. A.; Giepmans, B. N. G.; Palmer, A. E.; Tsien, R. Y. Improved Monomeric Red, Orange and Yellow Fluorescent Proteins Derived from Discosoma Sp. Red Fluorescent Protein. *Nat. Biotechnol.* **2004**, *22* (12), 1567–1572. https://doi.org/10.1038/nbt1037.

(100) Wiens, M.; Shen, Y.; Li, X.; Salem, M.; Smisdom, N.; Zhang, W.; Brown, A.; Campbell, R. E. A Tandem Green-Red Heterodimeric Fluorescent Protein with High FRET Efficiency. *ChemBioChem* **2016**, *118* (7), 2858–2871. https://doi.org/10.1002/cbic.201600492.

(101) Bindels, D. S.; Haarbosch, L.; van Weeren, L.; Postma, M.; Wiese, K. E.; Mastop, M.; Aumonier, S.; Gotthard, G.; Royant, A.; Hink, M. A.; et al. MScarlet: A Bright Monomeric Red Fluorescent Protein for Cellular Imaging. *Nat. Methods* **2017**, *14* (1), 53–56. https://doi.org/10.1038/nmeth.4074.

(102) Calovi, S.; Mut-Arbona, P.; Sperlágh, B. Microglia and the Purinergic Signaling System. *Neuroscience* **2019**, *405*, 137–147. https://doi.org/10.1016/j.neuroscience.2018.12.021.

(103) Oliveira-Giacomelli, Á.; Naaldijk, Y.; Sardá-Arroyo, L.; Gonçalves, M. C. B.; Corrêa-Velloso, J.; Pillat, M. M.; de Souza, H. D. N.; Ulrich, H. Purinergic Receptors in Neurological Diseases With Motor Symptoms: Targets for Therapy. *Front. Pharmacol.* **2018**, *9*, 325. https://doi.org/10.3389/fphar.2018.00325.

(104) Liu, J.-Q.; Chu, S.-F.; Zhou, X.; Zhang, D.-Y.; Chen, N.-H. Role of Chemokines in Parkinson's Disease. *Brain Res. Bull.* **2019**. https://doi.org/10.1016/j.brainresbull.2019.05.020.

(105) Tsukimoto, M. Purinergic Signaling Is a Novel Mechanism of the Cellular Response to Ionizing Radiation. *Biol. Pharm. Bull.* **2015**, *38* (7), 951–959. https://doi.org/10.1248/bpb.b15-00062.

(106) Gao, Z.-G.; Jacobson, K. A. Distinct Signaling Patterns of Allosteric Antagonism at the P2Y1 Receptor. *Mol. Pharmacol.* **2017**, *92* (5), 613–626. https://doi.org/10.1124/mol.117.109660.

(107) Rajendran, M.; Dane, E.; Conley, J.; Tantama, M. Imaging Adenosine Triphosphate (ATP). *Biol. Bull.* **2016**, *231* (1), 73–84. https://doi.org/10.1086/689592.

(108) Garner, E. C. Dynamic Instability in a DNA-Segregating Prokaryotic Actin Homolog. *Science* **2004**, *306* (5698), 1021–1025. https://doi.org/10.1126/science.1101313.

(109) Espelt, M. V.; de Tezanos Pinto, F.; Alvarez, C. L.; Alberti, G. S.; Incicco, J.; Denis, M. F. L.; Davio, C.; Schwarzbaum, P. J. On the Role of ATP Release, EctoATPase Activity, and Extracellular ADP in the Regulatory Volume Decrease of Huh-7 Human Hepatoma Cells. *Am. J. Physiol.-Cell Physiol.* **2013**, *304* (10), C1013–C1026. https://doi.org/10.1152/ajpcell.00254.2012.

(110) Tan, L.; Zhao, B.; Ge, F.-T.; Sun, D.-H.; Yu, T. Shockwaves Inhibit Chondrogenic Differentiation of Human Mesenchymal Stem Cells in Association with Adenosine and A2B Receptors. *Sci. Rep.* **2017**, *7*. https://doi.org/10.1038/s41598-017-14875-y.

(111) Van den Ent, F.; Møller-Jensen, J.; Amos, L. A.; Gerdes, K.; Löwe, J. F-Actin-like Filaments Formed by Plasmid Segregation Protein ParM. *EMBO J.* **2002**, *21* (24), 6935–6943. https://doi.org/10.1093/emboj/cdf672.

(112) Fritz, R. D.; Letzelter, M.; Reimann, A.; Martin, K.; Fusco, L.; Ritsma, L.; Ponsioen, B.; Fluri, E.; Schulte-Merker, S.; van Rheenen, J.; et al. A Versatile Toolkit to Produce Sensitive FRET Biosensors to Visualize Signaling in Time and Space. *Sci. Signal.* **2013**, *6* (285), rs12. https://doi.org/10.1126/scisignal.2004135.

(113) Nagai, T.; Ibata, K.; Park, E. S.; Kubota, M.; Mikoshiba, K.; Miyawaki, A. A Variant of Yellow Fluorescent Protein with Fast and Efficient Maturation for Cell-Biological Applications. *Nat. Biotechnol.* **2002**, *20* (1), 87–90. https://doi.org/10.1038/nbt0102-87.

(114) Ai, H.; Henderson, J. N.; Remington, S. J.; Campbell, R. E. Directed Evolution of a Monomeric, Bright and Photostable Version of Clavularia Cyan Fluorescent Protein: Structural Characterization and Applications in Fluorescence Imaging. *Biochem. J.* **2006**, *400* (3), 531–540. https://doi.org/10.1042/BJ20060874.

(115) Dooley, C. T.; Dore, T. M.; Hanson, G. T.; Jackson, W. C.; Remington, S. J.; Tsien, R. Y. Imaging Dynamic Redox Changes in Mammalian Cells with Green Fluorescent Protein Indicators. *J. Biol. Chem.* **2004**, *279* (21), 22284–22293. https://doi.org/10.1074/jbc.M312847200.

(116) Gutscher, M.; Pauleau, A.-L.; Marty, L.; Brach, T.; Wabnitz, G. H.; Samstag, Y.; Meyer, A. J.; Dick, T. P. Real-Time Imaging of the Intracellular Glutathione Redox Potential. *Nat. Methods* **2008**, *5* (6), 553–559. https://doi.org/10.1038/nmeth.1212.

(117) Gutscher, M.; Sobotta, M. C.; Wabnitz, G. H.; Ballikaya, S.; Meyer, A. J.; Samstag, Y.; Dick, T. P. Proximity-Based Protein Thiol Oxidation by H \textlesssub\textgreater2\textless/Sub\textgreater O \textlesssub\textgreater2\textless/Sub\textgreater -Scavenging Peroxidases. *J. Biol. Chem.* **2009**, *284* (46), 31532–31540. https://doi.org/10.1074/jbc.M109.059246.

(118) Lohman, J. R.; Remington, S. J. Development of a Family of Redox-Sensitive Green Fluorescent Protein Indicators for Use in Relatively Oxidizing Subcellular Environments † ‡. *Biochemistry* **2008**, *47* (33), 8678–8688. https://doi.org/10.1021/bi800498g.

(119) Wagener, K. C.; Kolbrink, B.; Dietrich, K.; Kizina, K. M.; Terwitte, L. S.; Kempkes, B.; Bao, G.; Müller, M. Redox Indicator Mice Stably Expressing Genetically Encoded Neuronal RoGFP: Versatile Tools to Decipher Subcellular Redox Dynamics in Neuropathophysiology. *Antioxid. Redox Signal.* **2016**, *25* (1), 41–58. https://doi.org/10.1089/ars.2015.6587.

(120) Allen, M. D.; Zhang, J. A Tunable FRET Circuit for Engineering Fluorescent Biosensors. *Angew. Chem. Int. Ed.* **2008**, *47* (3), 500–502. https://doi.org/10.1002/anie.200703493.

(121) Shimozono, S.; Hosoi, H.; Mizuno, H.; Fukano, T.; Tahara, T.; Miyawaki, A. Concatenation of Cyan and Yellow Fluorescent Proteins for Efficient Resonance Energy Transfer. *Biochemistry* **2006**, *45* (20), 6267–6271. https://doi.org/10.1021/bi060093i.

(122) Evers, T. H.; van Dongen, E. M. W. M.; Faesen, A. C.; Meijer, E. W.; Merkx, M. Quantitative Understanding of the Energy Transfer between Fluorescent Proteins Connected via Flexible Peptide Linkers. *Biochemistry* **2006**, *45* (44), 13183–13192. https://doi.org/10.1021/bi061288t.

(123) Yano, T.; Oku, M.; Akeyama, N.; Itoyama, A.; Yurimoto, H.; Kuge, S.; Fujiki, Y.; Sakai, Y. A Novel Fluorescent Sensor Protein for Visualization of Redox States in the Cytoplasm and in Peroxisomes. *Mol. Cell. Biol.* **2010**, *30* (15), 3758–3766. https://doi.org/10.1128/MCB.00121-10.

(124) Abraham, B. G.; Santala, V.; Tkachenko, N. V.; Karp, M. Fluorescent Protein-Based FRET Sensor for Intracellular Monitoring of Redox Status in Bacteria at Single Cell Level. *Anal. Bioanal. Chem.* **2014**, *406* (28), 7195–7204. https://doi.org/10.1007/s00216-014-8165-1.

(125) Iqbal, A.; Arslan, S.; Okumus, B.; Wilson, T. J.; Giraud, G.; Norman, D. G.; Ha, T.; Lilley, D. M. J. Orientation Dependence in Fluorescent Energy Transfer between Cy3 and Cy5 Terminally Attached to Double-Stranded Nucleic Acids. *Proc. Natl. Acad. Sci. U. S. A.* **2008**, *105* (32), 11176–11181. https://doi.org/10.1073/pnas.0801707105.

(126) Subach, O. M.; Entenberg, D.; Condeelis, J. S.; Verkhusha, V. V. A FRET-Facilitated Photoswitching Using an Orange Fluorescent Protein with the Fast Photoconversion Kinetics. *J. Am. Chem. Soc.* **2012**, *134* (36), 14789–14799. https://doi.org/10.1021/ja3034137.

(127) Lam, A. J.; St-Pierre, F.; Gong, Y.; Marshall, J. D.; Cranfill, P. J.; Baird, M. a.; McKeown, M. R.; Wiedenmann, J.; Davidson, M. W.; Schnitzer, M. J.; et al. Improving FRET Dynamic Range with Bright Green and Red Fluorescent Proteins. *Nat. Methods* **2012**, *9* (10), 1005–1012. https://doi.org/10.1038/nmeth.2171.

(128) Shaner, N. C.; Lin, M. Z.; McKeown, M. R.; Steinbach, P. a; Hazelwood, K. L.; Davidson, M. W.; Tsien, R. Y. Improving the Photostability of Bright Monomeric Orange and Red Fluorescent Proteins. *Nat. Methods* **2008**, *5* (6), 545–551. https://doi.org/10.1038/nmeth.1209.

(129) Bajar, B.; Wang, E.; Zhang, S.; Lin, M.; Chu, J. A Guide to Fluorescent Protein FRET Pairs. *Sensors* **2016**, *16* (9), 1488. https://doi.org/10.3390/s16091488.

(130) Deutsch, C.; Erecińska, M.; Werrlein, R.; Silver, I. A. Cellular Energy Metabolism, Trans-Plasma and Trans-Mitochondrial Membrane Potentials, and PH Gradients in Mouse Neuroblastoma. *Proc. Natl. Acad. Sci. U. S. A.* **1979**, *76* (5), 2175–9.

(131) Dickens, C. J.; Gillespie, J. I.; Greenwell, J. R. Interactions between Intracellular PH and Calcium in Single Mouse Neuroblastoma (N2A) and Rat Pheochromocytoma Cells (PC12). *Q. J. Exp. Physiol. Camb. Engl.* **1989**, *74* (5), 671–9.

(132) Kolossov, V. L.; Beaudoin, J. N.; Prabhu Ponnuraj, N.; DiLiberto, S. J.; Hanafin, W. P.; Kenis, P. J. a.; Gaskins, H. R. Thiol-Based Antioxidants Elicit Mitochondrial Oxidation via Respiratory Complex III. *Am. J. Physiol. - Cell Physiol.* **2015**, ajpcell.00006.2015. https://doi.org/10.1152/ajpcell.00006.2015.

(133) Korge, P.; Calmettes, G.; Weiss, J. N. Increased Reactive Oxygen Species Production during Reductive Stress: The Roles of Mitochondrial Glutathione and Thioredoxin Reductases. *Biochim. Biophys. Acta* **2015**, *1847* (6–7), 514–25. https://doi.org/10.1016/j.bbabio.2015.02.012.

(134) Zhang, H.; Limphong, P.; Pieper, J.; Liu, Q.; Rodesch, C. K.; Christians, E.; Benjamin, I. J. Glutathione-Dependent Reductive Stress Triggers Mitochondrial Oxidation and Cytotoxicity. *Faseb J* **2012**, *26* (4), 1442–1451. https://doi.org/10.1096/fj.11-199869.

(135) Li, N.; Ragheb, K.; Lawler, G.; Sturgis, J.; Rajwa, B.; Melendez, J. A.; Robinson, J. P. Mitochondrial Complex I Inhibitor Rotenone Induces Apoptosis through Enhancing Mitochondrial Reactive Oxygen Species Production. *J. Biol. Chem.* **2003**, *278* (10), 8516–8525. https://doi.org/10.1074/jbc.M210432200.

(136) Zhou, Q.; Liu, C.; Liu, W.; Zhang, H.; Zhang, R.; Liu, J.; Zhang, J.; Xu, C.; Liu, L.; Huang, S.; et al. Rotenone Induction of Hydrogen Peroxide Inhibits MTOR-Mediated S6K1 and 4E-BP1/EIF4E Pathways, Leading to Neuronal Apoptosis. *Toxicol. Sci. Off. J. Soc. Toxicol.* **2015**, *143* (1), 81–96. https://doi.org/10.1093/toxsci/kfu211.

(137) Gohil, V. M.; Sheth, S. A.; Nilsson, R.; Wojtovich, A. P.; Lee, J. H.; Perocchi, F.; Chen, W.; Clish, C. B.; Ayata, C.; Brookes, P. S.; et al. Nutrient-Sensitized Screening for Drugs That Shift Energy Metabolism from Mitochondrial Respiration to Glycolysis. *Nat. Biotechnol.* **2010**, *28* (3), 249–55. https://doi.org/10.1038/nbt.1606.

(138) Szajewski, R. P.; Whitesides, G. M. Rate Constants and Equilibrium Constants for Thiol-Disulfide Interchange Reactions Involving Oxidized Glutathione. *J. Am. Chem. Soc.* **1980**, *102* (6), 2011–2026. https://doi.org/10.1021/ja00526a042.